A Deep *Chandra* ACIS Survey of M83[1]

Knox S. Long[2], Kip D. Kuntz[3], William P. Blair[3], Leith Godfrey[4,5], Paul P. Plucinsky[6], Roberto Soria[4], Christopher Stockdale[7], and P. Frank Winkler[8]

ABSTRACT

We have obtained a series of deep X-ray images of the nearby galaxy M83 using *Chandra*, with a total exposure of 729 ks. Combining the new data with earlier archival observations totaling 61 ks, we find 378 point sources within the D_{25} contour of the galaxy. We find 80 more sources, mostly background AGN, outside of the D_{25} contour. Of the X-ray sources, 47 have been detected in a new radio survey of M83 obtained using the Australia Telescope Compact Array. Of the X-ray sources, at least 87 seem likely to be supernova remnants (SNRs), based on a combination of their properties in X-rays and at other wavelengths. We attempt to classify the point source population of M83 through a combination of spectral and temporal analysis. As part of this effort, we carry out an initial spectral analysis of the 29 brightest X-ray sources. The soft X-ray sources in the disk, many of which are SNRs, are associated with the spiral arms, while the harder X-ray sources, mostly X-ray binaries (XRBs), do not appear to be. After eliminating AGN, foreground stars and identified SNRs from the sample, we construct the cumulative luminosity function (CLF) of XRBs brighter than 8×10^{35} ergs s^{-1}. Despite M83's relatively high star formation rate, the CLF indicates that most of the XRBs in the disk are low mass XRBs.

[2]Space Telescope Science Institute, 3700 San Martin Drive, Baltimore, MD, 21218; long@stsci.edu

[3]The Henry A. Rowland Department of Physics and Astronomy, Johns Hopkins University, 3400 N. Charles Street, Baltimore, MD, 21218; kuntz@pha.jhu.edu, wpb@pha.jhu.edu

[4]Curtin Institute of Radio Astronomy, Curtin University, 1 Turner Avenue, Bentley WA6102, Australia; leith.godfrey@icrar.org, roberto.soria@icrar.org

[5]Netherlands Institute for Radio Astronomy (ASTRON), Postbus 2, 7990 AA Dwingeloo, the Netherlands'; godfrey@astron.nl

[6]Harvard-Smithsonian Center for Astrophysics, 60 Garden Street, Cambridge, MA 02138; plucinsky@cfa.harvard.edu

[7]Department of Physics, Marquette University, PO Box 1881, Milwaukee, WI 53201-1881, USA; christopher.stockdale@marquette.edu

[8]Department of Physics, Middlebury College, Middlebury, VT, 05753; winkler@middlebury.edu

Subject Headings: galaxies: individual (M83) – galaxies: ISM – supernova remnants – X-rays: general – X-rays: binaries – X-rays: individual (M83) – SN: individual (SN1923A)

1. Introduction

M83 (NGC 5236) is a large, grand-design spiral galaxy at a distance of 4.61 Mpc (Saha et al. 2006) that has been the site of six historical supernovae (SNe; see Stockdale et al. (2006) and references therein). It has very active star formation, estimated by Boissier et al. (2005) at between 3 and 4 $M_\odot \, \mathrm{yr}^{-1}$. Due to its nearly face-on inclination (i=24°, Talbot et al. 1979), very well defined spiral arms, and location along a line of sight with low Galactic absorption (N_H=4 × 10^{20} cm^{-2}; Kalberla et al. 2005), M83 provides an outstanding laboratory for understanding X-ray source populations in star-forming galaxies.

Given the nature of M83, it is not surprising that it has been observed many times at X-ray wavelengths. Trinchieri et al. (1985) were the first to obtain spatially resolved images of M83 using the *Einstein Observatory* and to discuss its X-ray properties. Immler et al. (1999) used the improved sensitivity of the ROSAT HRI to resolve about half of the total luminosity of the galaxy (1.1×10^{40} ergs s^{-1}, corrected to our assumed distance of 4.61 Mpc) into 21 X-ray point sources, and to show that some of the diffuse emission was associated with the spiral arms of M83. However, detailed study of the galaxy has become possible only with the increased sensitivity of *Chandra* (and *XMM/Newton*). Soria & Wu (2002, 2003) analyzed a 51 Ks observation of M83 with *Chandra*'s ACIS-S instrument, identifying 127 sources to a limiting sensitivity of $\sim 4.6 \times 10^{36}$ ergs s^{-1} (also adjusted to a distance of 4.61 Mpc), and showed that many of the discrete sources as well as much of the emission from hot gas and unresolved sources is associated with the spiral arms. Most of the sources have been tentatively identified as X-ray binaries (XRBs), based on their spectral characteristics, but a number of supernova remnants (SNRs) and possible supersoft sources (SSS) have been identified as well.

Here we provide an overview of a very deep set of *Chandra* observations of M83 and an analysis of the X-ray point source populations. We also describe new radio observations of M83 made with the Australia Telescope Compact Array (ATCA), which were obtained to support the *Chandra* observations. We have previously used these data to report the

---

[1]Based on observations made with NASA's *Chandra* X-ray Observatory. NASA's *Chandra* Observatory is operated by Smithsonian Astrophysical Observatory under contract # NAS83060 and the data were obtained through program GO1-12115.

discovery of a new ultra-luminous X-ray source (ULX) in M83 (Soria et al. 2012), to report the recovery of the remnant of the historical SN1957D in X-rays in M83 (Long et al. 2012) and more recently to describe the properties of a new micro-quasar in M83 (Soria et al. 2014).

2. Observations

2.1. X-ray Observations

The X-ray observations of M83 in our survey were all carried out with ACIS-S in order to maximize the sensitivity to soft X-ray sources, such as SNRs, and to diffuse emission. The nucleus of M83 was centered in the field of the back-illuminated S3 chip to provide reasonably uniform coverage of M83. In addition to the S3 chip, data were also obtained from chips S1, S2, S4, I2 and I3. All of the observations were made in the "very faint" mode to optimize background subtraction. Observations were spaced over a period of one year from 2010 December to 2011 December, as indicated in Table 1. The only difference among observations was the roll orientation of the spacecraft and the differing exposure times. All of the observations were nominal, and yielded a total of 729 ks of useful data. In order to maximize our sensitivity and more importantly to improve our ability to identify time variable sources, we included in our analysis earlier *Chandra* observations of M83 in 2000 and 2001 totaling 61 ks obtained by G. Rieke (Prop ID. 1600489) and by A. Prestwich (Prop ID. 267005758). These data were obtained in a very similar manner to that of our survey, and increased the total exposure to 790 ks. As indicated in Figure 1, which shows the summed exposure time map superposed on an optical image of the galaxy, most of the optically bright inner disk of the galaxy was included in the observations.

For the data analysis which follows, we reprocessed the data using tools available in CIAO Version 4.4 (Fruscione et al. 2006). We used CalDB version 4.5.3 for the analysis, which includes a revised model for the buildup of contamination on the optical blocking filter of ACIS. After reprocessing the data, we aligned all the images to one another using the positions of sources identified with the source finding routine *wavdetect* and the script *reproject_aspect*, which matches the offsets, scale and rotation of each image to a reference image–in our case ObsID 12994, the observation with the longest exposure time. To reduce the error in this alignment we used a subset of the sources identified with *wavdetect*, specifically 49 sources with more than 300 broadband counts in the summed exposures, and located between 1 and 6 kpc from the galactic center, to avoid the confused nuclear region of the galaxy. The *reproject_aspect* procedure reduced the alignment errors between ObsID 12994 and the other images from $0.5 - 1$ pixels to just $0.1 - 0.2$ pixels, or $0\farcs05 - 0\farcs1$.

This procedure assured that the X-ray images were coaligned, but does not establish absolute astrometry for the X-ray source catalog. Typically, the absolute astrometry of *Chandra* images is accurate to $0\rlap.{''}6$.[2] An initial comparison of X-ray source positions in the *Chandra* catalog to those in our ATCA survey indicated an average offset of $0\rlap.{''}4$ between the two, mostly in right ascension. A similar offset was seen in comparisons between SNR candidates identified in our Magellan images (Blair et al. 2012), which are discussed in more detail in Section 5.3. Sources in the Magellan data and the ATCA data are well aligned with one another. The astrometry of the ATCA data is tied to the ICRF2 quasar catalog (Ma et al. 2009), which is accurate to $0\rlap.{''}1$, while the Magellan astrometry is tied to high-precision stars from the UCAC3 and USNO-B1.0 catalogs, which produced rms errors < 80 mas. As discussed in Section 2.2 below, there are a number of sources that appear both in our X-ray source catalog and in the ATCA data. Comparison of the object positions in the two catalogs indicated a small but systematic offset between the two catalogs. Therefore, in the catalog produced below (Table 3), we have shifted the X-ray positions by ΔR.A. = -$0\rlap.{''}35$ and ΔDecl. = $0\rlap.{''}08$ to compensate for this systematic error and produce the best absolute positions.

A slightly-smoothed three-color image of the combined X-ray data is shown in Figure 2. In addition to a large number of point sources, the image contains soft diffuse X-ray emission that traces the spiral arms of the galaxy. There is a patch of extended emission with a hard X-ray spectrum near R.A. 13:37:08, Declination -29:53:40 visible to the SE of the nucleus. We have not noticed similar features in the X-ray images of other nearby galaxies that we have studied. We suspect that it is a background cluster of galaxies whose X-ray emission is visible through the disk of M83. There is no obvious optical cluster at this location, but this would could well be due to obscuration as a dust lane runs through this region. Finally, the nuclear region comprises both diffuse emission and about 40 bright point sources.

2.2. Radio Observations

To support and extend our X-ray study of M83, we have been carrying out a number of other studies of M83, including optical broad- and narrow-band imaging with the IMACS camera on Magellan (Blair et al. 2012), optical imaging with the Wide Field Camera 3 (WFC3) on the *Hubble Space Telescope* (*HST*; W. P. Blair PI, Prop. ID. 12513, Blair et al. (2013)), and radio imaging with the Jansky Very Large Array (JVLA, C. Stockdale PI, Prog.

---

[2] 90% of ACIS-S test sources within $3'$ of on-axis have positions accurate to within $0\rlap.{''}6$; see http://cxc.harvard.edu/cal/ASPECT/celmon/

ID. 12A-335). The *HST* and the JVLA results will be described elsewhere. Here we describe new 6 and 3 cm radio imaging we have obtained from ATCA.

M83 was observed with the ATCA in the 6A configuration for 12 hours on each of 2011 April 28, 29 and 30, for a total observing time of 36 hours, simultaneously recording 2 GHz bandwidths centered on 5.5 GHz and 9 GHz in all four polarization products. Regular scans on the nearby phase calibrator PKS 1313–333 were scheduled throughout the observations, as well as scans on the ATCA primary flux calibrator PKS 1934–638. Standard calibration and editing procedures were carried out using the MIRIAD data analysis package (Sault et al. 1995). Following calibration, the data were exported for imaging and self-calibration using the Common Astronomy Software Applications (CASA) package (McMullin et al. 2007). Due to the large size of M83 ($\sim 12'$) relative to the ATCA primary beam width ($8.'5$ and $5.'2$ at 5.5 and 9 GHz respectively), primary beam correction was required to account for the radial dependence of gain in the image.

The primary beam correction results in position-dependent noise, with the rms noise increasing with distance from the pointing center. This renders most source-finding algorithms unsuitable. We therefore applied the following procedure to produce the source catalog. First, we identified candidate sources by running the MIRIAD image-finding algorithm *imsad*, prior to primary beam correction. The resulting source list was edited based on visual inspection of the candidate sources. After applying the primary beam correction to each image, flux densities were obtained from the CASA task *imstat* using an elliptical aperture centered on each candidate source, with the aperture major and minor axes equal to twice the restoring beam FWHM and rotated to the same position angle. For each candidate source, the uncertainty in flux density was calculated using the nearest source-free region of the radio map. In cases where the fit converged, coordinates were obtained by fitting an elliptical Gaussian to the pixels with values greater than half the peak—using the CASA task *imfit*; otherwise, the centroid was determined and used.

The results are shown in Table 2 and in Figure 3. We find a total of 109 radio sources, mostly associated with the spiral arms of the galaxy. Of these, 49 of the ATCA sources lie within $2''$ of sources in the earlier VLA study of M83 conducted by Maddox et al. (2006).[3] Only 8 of the 55 VLA sources have no counterparts in our ATCA survey. Two ATCA sources, A063 and A064, are associated with M06-34; two, A077 and A079, are associated with M06-40. A063 is closer ($0.''5$) to M06-34 than is A064 ($1.''5$) and is most likely the correct association. On the other hand, the A71 and A79 are about the same distance ($1.''7$ and $1.''9$)

---

[3]There is a clear offset in the positions in the two surveys of about $0.''6$, which we corrected before associating sources with one another.

from M06-40.

Two historical SNe, SN1957D and SN1950B, were clearly detected, and both had been previously identified by Maddox et al. (2006, see also references therein). The situation with SN1923A is more problematic, however, because the position of the optical SN was not well determined. Pennington et al. (1982) went to considerable effort to measure the position on original plate material from 1923, but the SN image itself creates an extended patch of emission and the centroid may be affected by other local emissions near the site. Precessing their position to J2000, the Pennington et al. (1982) position is $4\rlap{.}''2$ away ($3\rlap{.}''8$ south in declination) from the closest ATCA, A096, which seems too far to be a real association, if the errors on the position given by Pennington et al. (1982) can be believed. However, we note that the position determined by Pennington et al. (1982) for SN1957D is $2\rlap{.}''4$ south from what is now the well-known position of SN1957D (ATCA and *HST*), in the same direction as the discrepancy for SN1923A. This is also outside the stated errors in Pennington et al. (1982), and so we suspect the error budget they estimated was too low.

We have independently used the figure based on the original plate showing SN1923A, provided in Pennington et al. (1982, their Figure 1b) to reconstruct the SN position on our Magellan images. Again with the uncertainty that other sources may have been blended with the SN on the original plate, we determine a reconstructed J2000 position of R.A.=13:37:09.19, Dec=$-$29:51:01.39, which is $3\rlap{.}''2$ almost due north of the Pennington position, and just over $2''$ from A096 (differing primarily in R.A.). If we consider the difference between the Pennington position and our reconstruction to be more indicative of the real uncertainties, then an identification with A096 is consistent.

Eck et al. (1998) have also claimed a radio source near the optical position of SN1923A, although their radio source position had an uncertainty of $5''$. Given that the ATCA radio sources in this region are unconfused, the source reported by Eck et al. (1998) is likely to be the same source as A096. If true, then the changes in flux of this source with time are also consistent with it being due to the young remnant of the SN. If continued monitoring of A096 confirms the decay in flux with time, this would be a smoking gun for the ID, and the ATCA radio position would provide the best positional information for SN1923A going forward.

Comments and suggested identifications for many additional sources in the ATCA images are provided in Table 2, but we defer discussion of these until Section 5.

3. The X-ray Point Source Catalog

As indicated in Section 2.1, the X-ray emission from M83 is complex. Not only are there contributions from point sources and extended emission, but the density of point sources varies greatly. Furthermore, the *Chandra* point spread function (PSF) also varies with position away from the field center. As a result, the generation of a point source catalog is not trivial. We have used a combination of CIAO tools and the package *ACIS Extract* (*AE*, Broos et al. 2010) to carry out this task. The procedure we used, in brief, was to use *wavdetect* to create source lists from each of the individual observations as well as from the combined X-ray images. We created source lists for a variety of energy bands and combined all of these, eliminating duplicate sources, to yield a total of 847 candidate sources. We pared this list down to 458 "good" sources using various statistical tests and comparisons among the data subsets. Finally, we visually inspected the resulting "good" source list on the *Chandra* images as a sanity check that our list of candidate sources was not missing any obvious sources. The following paragraphs provide the details of this procedure.

3.1. Preliminary source list and positions

We used the CIAO task *wavdetect* to generate initial source lists. In running *wavdetect*, we set the *sigthresh* parameter to 10^{-6}, which is expected to produce about one false detection per chip. Because the *Chandra* PSF degrades as one moves off-axis, we set the *scales* parameter to all the powers of two up to 32 pixels. We used five overlapping energy bands, 0.35-1.0 keV, 0.35-8.0 keV, 0.5-2.0 keV, 1.0-2.0 keV, and 2.0-8.0 keV, which produced 180 individual source lists, one for each energy band for each ObsID. Although we ran *wavdetect* individually on the S1, S2, S3, and S4 chips, we first merged all of the lists for different chips of each ObsID/energy combination, after checking for duplicate sources near the chip gap. In merging the source lists, we used the local PSF size to determine whether nearby sources detected in different lists were indeed the same source; if the centers of a source in one list fell within the 85% encircled energy ellipse of a source in another list, we assumed it to be the same source. We then merged the lists for the same ObsID but different energies, to create a list of unique sources for each ObsID. Finally, we merged the lists from all of the ObsIDs, again using the PSF size criterion for matching sources.

In parallel, we ran *wavdetect* on the combined data set, using the same parameters and energy bands as for the individual observations. As before, we merged the lists produced in the different energy bands, using the above criterion for duplicate sources. Finally, we combined the lists from the combined and individual observations. By running the source detection on both the total data set and the individual observations, we managed to produce

the deepest possible catalog while not missing transients that might fall below the significance threshold in the total data set.

A visual check of the source positions projected onto a display of the actual data was used as a sanity check. The only area where we made modifications to the list produced through the *wavdetect* process described above was in the nuclear region, where diffuse emission is quite prominent. In this complicated region it appeared that some of the identified sources were not well centered on visible X-ray peaks, and in a few cases, there were multiple *wavdetect* positions identified with a single peak in the X-ray image. We manually removed duplicate targets and adjusted positions for a handful of sources to produce the final catalog.

3.2. Final Source List and Count Rates

With the positions established, we then used *AE* to derive net count rates from the sources in various energy bands: 0.35-8 keV (total or T), 0.35-1.1 keV (soft or S), 1.1-2.6 keV (medium or M), 2.6-8 keV (hard or H), 0.5-2 keV ($\mathcal{S}$), and 2-8 keV ($\mathcal{H}$). Our choice of these bands was based on a variety of overlapping goals. The broad 0.35-8 keV samples the full energy range accessible to *Chandra* observations. The three bands, 0.35-1.1 keV, 1.1-2.6 keV and 2.6-8 keV provide bands intended to classify sources on the basis of their hardness ratios. The boundary at 1.1 keV, in particular, is just above the region containing strong features due to Ne and Fe seen in the spectra of most SNRs. The 0.5-2 keV and 2-8 keV bands are needed because number counts of AGN and of X-ray binary populations are normally carried out in these bands, and because the 0.5-2.0 keV band, encompassing the peak of the response curve, provides better statistics for some purposes than S+M.

The *AE* count rates were used to establish which of the sources in the candidate list were statistically valid. We retained any source that had a probability-of-no-source $< 5 \times 10^{-6}$ in any one of these bands in the total data set. For our final run of *AE*, our list of source candidates had 847 potential sources. Of those, we find a total of 458 valid point sources, whose properties are listed in Table 3. Most of these (409) were detected as sources in the 0.35-8 keV energy band. Totals of 315, 305, and 179 were detected as sources in the soft, medium and hard bands, respectively. There were 383 sources detected in the 0.5-2 keV band and 210 sources in the 2-8 keV band. Without the 0.5-2 keV and 2-8 keV sources there would have been 443 sources; adding these two bands resulted in 15 more sources. Of the 458 point sources, 378 are located within the area defined by the D_{25} ellipse of the galaxy (which we take to have a major axis diameter of 12.9 arcmin), and the remaining 80 are outside this region. There were 43 sources in the nuclear region (defined to be any source within a projected radius of 0.5 kpc from the optical nucleus).

Over the course of analyzing these data, we repeated the process of identifying source candidates and processing them through *AE* multiple times, with differing versions of CIAO and the other tools that make up *AE*. While the vast majority of sources appear in all of the lists we have developed, it is clear that the faintest 5-10% of the sources we detect by this procedure vary somewhat. This is not surprising given the combination of diffuse emission and field crowding that exists in places. Once again, a visual check was used to inspect the "good" sources from *AE*. Most of the sources are readily apparent in the raw images or in a smoothed version of them, but a small number of the fainter objects, mostly located in regions with bright diffuse emission, are hard to pick out in these images. The user is cautioned to be wary of the faintest sources, but we have not eliminated these objects from the catalog since they passed the statistical test we applied.

The complete source list in right ascension order is presented in Table 3. For ease of reference we have labeled the sources X001 through X458. Along with this name (col. 1), the Table provides for each source the position (col. 3 and 4), the position error as determined by AE (col. 5), the total exposure time (col. 6), the count rate in the 0.35-8 keV band (col. 7), and two hardness ratios (col. 8 and 9), which are described in the next section. Count rates for detected sources range over almost four orders of magnitude, from 2×10^{-5} to 0.11 counts s^{-1}.

4. Derived Source Characteristics

4.1. Source Fluxes, Luminosities, and Hardness Ratios

The conversion of source counts to flux of an X-ray source depends on the assumed X-ray spectrum and, for soft sources, the absorbing column. Although *AE* provides several estimates of the fluxes of the sources it reports, it does not permit one to specify the shape of the spectrum. *AE* does, however, produce nominal X-ray spectra of all of the sources if requested. We have used these spectra in conjunction with the task *xspec* to estimate band-limited fluxes, assuming a power-law source with a photon index of -1.9 and foreground absorption of 4×10^{20} cm^{-2}. This choice of spectrum is appropriate for compact binaries and background AGN, and is typical of that chosen for other studies of the X-ray properties of normal galaxies (see, e. g. Tüllmann et al. 2011). Fluxes in units of photons cm^{-2} s^{-1} for the various bands, T, S, M, H, $\mathcal{S}$ and $\mathcal{H}$, are presented in Table 4. In addition, the average 0.35-8 keV X-ray luminosities of the sources, calculated from the energy flux in the 0.35-8 keV band, and assuming that all sources are located at the distance of M83, are shown in Table 4. The luminosities, calculated in this simple way, range from 5×10^{35} ergs s^{-1} to 2.2×10^{39} ergs s^{-1}. The total luminosity of all the point sources is 1.2×10^{40} ergs s^{-1}, so the

brightest source, which is the ULX we described in Soria et al. (2012), contributes 18% of the total point source luminosity of the galaxy. Broad band (0.35-8 keV) luminosities estimated using flux conversions based on our fiducial power law are fairly insensitive to differences in line of sight absorption less than $1 \times 10^{22}\,\mathrm{cm}^{-2}$ for hard sources like compact binaries. However, our simple calculation overestimates luminosities for soft, relatively unabsorbed sources, such as many SNRs (by about a factor of 2 for a source with a characteristic plasma temperature of 0.6 keV and low absorption).

Hardness ratio plots, based on the photon fluxes of the sources, are shown in Figure 5, with different panels of the plot showing different subsets of the sample. Of the 458 sources in the sample, 57% have (M–S)/T ratios greater than -0.5, and 27% have (H–M)/T ratios greater than 0. Many of the sources form a central clump in the region with (M–S)/T ratio near -0.1 and (H–M)/T ratio near $+0.2$, and extending toward the S=0 line. This is the region of the diagram where compact binaries and AGN are both expected. The upper right panel shows sources located outside the D_{25} radius (green symbols), which indeed are systematically harder and thus consistent with a population dominated by AGN and other background sources. The panel at upper left shows sources within the D_{25} contour, which no doubt includes a combination of background AGN and sources intrinsic to M83. There is a also group of softer X-ray sources, as shown by the red symbols in the lower left panel, along the line with very little emission in the H band. Many of these sources, as will be discussed in Section 5.3, are coincident with optical emission nebulae with line ratios that suggest they are SNRs. A number of the additional objects in this region be SNRs as well. Some of the softest sources, those with very few counts in the M or H band, may be super-soft sources (SSSs – see below). The sources in the nuclear region (shown in black, lower right panel) have a wide variety of spectral shapes, consistent with a mixture of XRBs, SNRs, and other thermal emission within the starburst nucleus. More detailed discussions of specific source identifications are provided in Section 5.

4.2.   Variable and Transient Sources

Variability is an important clue to the nature of the X-ray sources in any X-ray sample, but various authors assess variability is different ways. Rather than attempt a full analysis of variability in this overview paper, we produce a preliminary assessment of the number of sources that were variable using a single, simple approach; we compare the time averaged fluxes of each of the sources in our source catalog in each of the separate observations listed in Table 1. We have not carried out a systematic assessment of whether sources vary within a single observation, although we have identified a few example objects for which this is true

(see Appendix A).

For our assessment, we have used a standard measure of variability

$$R_{ij} \equiv \frac{F_i - F_j}{\sqrt{\sigma_{F_i}^2 + \sigma_{F_j}^2}}, \tag{1}$$

where F is the measured photon flux in an observation, and σ_F is its Poisson-based uncertainty (see, e.g. Primini et al. 1993; Fridriksson et al. 2008). Typically, sources are considered to be variable if R_{ij} is greater than some threshold value R_0. To assess whether a source was variable in our set of observations, we first calculated the maximum observed value of R, hereafter R_{max}, from the multiple observations using equation 1. To estimate the value of R_{max} expected for a non-variable source, we created 10^6 simulations of each observation of the source, allowing for Poisson statistics, variations in the effective area of *Chandra* with time, and the regions used by AE to generate the background. We calculated R_{max} for each of these simulations, and used this to calculate for a constant source the probability $P(R_{max} > R_0)$ that R_{max} would be greater than R_0. Not surprisingly, these distribution functions resemble the cumulative distribution function and have no sharp features. There is no obvious threshold value of R_0 in the cumulative distribution function $P(R_{max} > R_0)$ that isolates constant sources from variable sources upon visually inspecting plots of the fluxes in the various observations of individual objects. Thus we have somewhat arbitrarily labeled as variable those sources for which $P(R_{max} > R_0) < 0.0027$, roughly the 3σ level.

We searched for variability in all of the bands. The sources that have been determined to be variable have been marked in Table 3. Of the 458 sources in our catalog, 96 were found to be variable in one or more bands, and of these, 83 were found in 0.35-8 keV (T) band. This is not surprising since the broad band contains all of the counts. There were 47, 52, 29, 68 and 38 detected in the S, M, H, $\mathcal{S}$, and $\mathcal{H}$ bands, respectively. Of the 13 sources not detected as variable in the 0.38-8 keV band, 8 were found to be variable in the 0.3-1.1 keV (S) band; there were no "new" variables detected in the 1.1-2.6 keV (M) band and small numbers in each of the other bands.[4] Our sensitivity to variation is clearly a function of the source brightness. We can detect variations comparable to the mean photon flux for sources brighter than $\sim 10^{-6}$ phot cm^{-2} s^{-1}, and variations of one third the mean flux for sources with photon fluxes $\sim 1.5 \times 10^{-5}$ phot cm^{-2} s^{-1}.

For sources with 0.35-8.0 keV band fluxes $> 10^{-15}$ ergs cm^{-2} s^{-1} within the D25 contour, the variable sources have average hardness ratios of (M–S)/T = -0.313±0.009 and (H–M)/T

---

[4]The 13 sources that were not detected as variable in the 0.35-8 keV (T) band, but were detected as variable in one of the other variables are indicated "V*" in column 6 of Table 3.

= -0.0419±0.0040. This compares to ratios of (M–S)/T = of -0.539±0.012 and (H–M)/T = -0.0358±0.0059 for the non-variable sources. One would expect the variable sources to be dominated by XRBs and AGN, both of which typically have hard X-ray spectra, while SNRs, which have softer spectra, are non-variable. For the (M–S)/T ratio, the variable sources are are harder on average, while for the (H–M)/T ratio, the two sources populations are indistinguishable. An inspection of Table 3 shows that many of variable sources are identified with binaries or AGN based on other considerations.

Some of the sources in our catalog are transients. The definition of a transient source varies between authors and has been shaped by the depth and cadence of the relevant data as well as details about the types of sources being sought. The criterion common to all definitions of transients is that the range between the maximum and minimum luminosities be "large," where large ranges from factors of 5 to 10. Some authors set the problematic criterion that the source be undetectable at its faintest, which can in principle select different types of objects depending on the sensitivity of the data set being considered. Temporal criteria are often applied to distinguish between transients and other types of strongly variable sources, usually to select sources with very short duty cycles.

We have set two criteria to identify transient objects. We first require that $R_{max} > 4$ and $P(R) < 0.0027$, which is effectively a statement that transients must have a large difference between the maximum and minimum fluxes. We then insist that transients be objects for which the bulk of the measurements have fluxes less than one quarter of the maximum flux, which constrains the duty cycle of the bright phase, eliminating objects that are variable on roughly month time-scales (i.e. the approximate cadence of our observations). However, these criteria still allow a wide variety of light-curve behaviors. To better characterize the behaviors, we have flagged our transient candidates with further descriptors as follows: "C" or "classical" transient sources have a single high point and a quiescent level consistent with zero (three sources); "B" sources have more than one high point (five sources); and "N" vary by a large amount, but never completely disappear (eight sources). The latter might be seen as classical transients given a less sensitive detection limit.

Also, since all but two of the observations were made over the course of about one year, and the remaining two(ObsIDs 793 and/or 2064) were taken almost a decade earlier, we must consider how this may have affected the variability assessments. We flagged with "A" those sources that were on (or off) in the archival data, and off (or on) in the current data. Five sources were very significantly detected in the archival data but consistent with zero in the current data, while six sources (including the ULX discussed by Soria et al. (2012)) would have been detected in the archival data at levels seen in the new observations. If we exclude the archival data, 21 sources are no longer considered variable. Interestingly, two

non-variable sources (based on the entire data set), X030 and X255, were found to be variable when the archival data were excluded, though their variability was just barely significant. Of the sources found to be variable only with the addition of the archival data, half show clear "events" in the archival data, meaning that the increase of baseline allowed detection of more transients. The other half do not show noticeable transient behavior, suggesting that the detection of their variability with the addition of the archival data may be due primarily to the increased count rate statistics.

5. Source Identifications in the M83 Catalog

The sources in our new M83 X-ray point source catalog no doubt arise from a variety of types of objects, including XRBs and SNRs, as well as objects not associated with M83, foreground stars and background AGN. We can, of course, follow two paths toward identifying sources: a) compare to previously cataloged objects of various kinds, and b) use the observed multiwavelength characteristics of the X-ray sources to make our best determination directly. In Table 5, we summarize the results of the more extended discussion below by showing our identifications and cross references as appropriate. Specifically, column 1 of this Table lists the X-ray source number while columns 2, 3 and 4 show positional coincidences with sources cataloged in recent X-ray, radio, and optical SNR studies, respectively, Columns 5 and 6 provide information about the variability and spectral properties of the sources, which as discussed in Sections 4.2 and 6 respectively, are useful for determining the nature of the sources. Finally, columns 7 and 8 provide our classification of the various source types along with notes that support or qualify the source classifications. The rationale for the various identifications and classifications is discussed below.

5.1. Sources from earlier Chandra and XMM studies of M83

The most detailed analysis of the archival *Chandra* observations of M83 was carried out by Soria & Wu (2003) who identified 127 sources in data obtained with the S3 chip in the 51 ks exposure obtained in 2000. Of these, 124 are located near (within 2″) of sources identified in our new deeper survey. This is hardly surprising, since we have included the archival data in our catalog as well. Since Soria & Wu (2003) analyzed only the S3 data, there are number of sources that we detect in the 2000 observations that they did not report.

There are three sources from Soria & Wu (2003) missing from our catalog. One of these, the soft source SW03-098, would have been included in our catalog had we chosen to report

any source detected in any of the various observations instead of only sources detected in the combined data set. Located in a spiral arm, this soft, and possibly variable, source fell below our detection limit in the combined data, but was seen in our analysis of Obs. ID 793, the observation discussed by Soria & Wu (2003). The source SW03-004 is located $2\rlap{.}''2$ from a source X026 in our catalog, and it is likely that this is in fact the same source as X026 despite being outside the limit of $2\rlap{.}''0$ we set in calculating spatial coincidences. The third source missing from our catalog, SW03-114, was among the faintest sources reported by Soria & Wu (2003), and appears to be spurious, at least by our detection criteria.

Recently, Ducci et al. (2013) have reported the results of a study of M83 from *XMM-Newton*.[5] Of the 189 *XMM* sources identified by Ducci et al. (2013), 46 are within the D_{25} contours of the galaxy, and 40 of these are aligned (within $3''$) with sources in our *Chandra* catalog. An additional 37 *XMM* sources outside the D_{25} contours are also found in our *Chandra* catalog. The smaller fraction of sources found outside the D_{25} contours in our catalog is simply due to the fact the many of the *XMM* sources are not in the FOV of our *Chandra* images. Due to the lower spatial resolution of *XMM*, several of the *XMM* sources, D13-090, D13-093, and D13-130, align with more than one *Chandra* source; we list only the closest association in Table 5.

5.2. Historical Supernovae

M83 has been the site of six historical SNe, two of which coincide in position with X-ray sources in our survey. The first of these is X279 = SN1957D, which was discussed in detail by Long et al. (2012), for which we conclude an active pulsar is most likely powering the relatively hard emission observed.

The second is SN1968L, which is spatially coincident with a bright X-ray source (X216) in the nuclear region of the galaxy. SN1968L was a poorly observed SN, thought to be of Type II (Wood & Andrews 1974), which Dopita et al. (2010) may have recovered as a faint [O III]-dominated emission nebula with *HST*. If SN1968L is the source associated with X216, it would be one of the more luminous young SNRs known, with L_X of about 7×10^{37} ergs s^{-1}. It is not detected as a radio source, which is not surprising due to the bright diffuse emission from the nuclear region. It does have an X-ray spectrum dominated by a thermal plasma. However, as discussed in more detail in Section 7, it is quite possible, perhaps likely, that

---

[5]Based on a comparison of the source positions in the two catalogs, there is a small offset of about $1\rlap{.}''0$ between the two catalogs. We had to shift the *XMM* positions by $+0\rlap{.}''94$ in right ascension and $-0\rlap{.}''45$ in declination to align the two catalogs.

X216 is simply a peak in the hot thermal gas permeating the nuclear region. As a result, more study will be required to establish whether X216 is really the X-ray counterpart to SN1968L.

We do not detect X-rays from any of the other historical SNe in M83, including SN1950B, which we do detect with ATCA (A024) and which had previously been detected at radio wavelengths by Maddox et al. (2006), or SN1923A, whose identification with the ATCA source A096 is discussed in Section 2.2.

5.3. Supernova Remnants

5.3.1. Optical Supernova Remnants

Optical SNRs in nearby galaxies are usually identified on the basis of high [S II]:Hα ratios compared to H II regions in interference filter imagery. The most recent study of M83 was carried out by Blair et al. (2012), who identified 225 SNR candidates in M83 based on this technique. (This paper specifically excluded the nuclear region, which had previously been covered by Dopita et al. (2010) using *HST* data.) Of these 225 objects, 67 (73) lie within $1''$ ($2''$) of sources in our new *Chandra* catalog. Almost all of these are soft X-ray sources, based on their hardness ratios. Their identification as X-ray sources provides strong support that these objects are indeed SNRs.

A small number of the positional coincidences might be by chance. To estimate the number of chance coincidences, we have adopted the following simple Monte Carlo procedure, which accounts for the fact that sources are spread in a non-uniform manner across M83. After having calculated the number of coincidences at the positions in two lists, we shift the positions of one of the lists in a random direction by $3 \times$ the positional offset that we allow, and recalculate the number of coincidences. For the SNR catalog described above we find on average 2.1 (8.5) coincidences for a position mismatch of $1''$ ($2''$). Indeed, other source characteristics indicate that a handful of the X-ray sources that coincide in position with optical SNRs are not true associations. For example, the very bright X-ray source X321, which is spatially coincident with B12-179, has a hard featureless spectrum and is most likely a black-hole binary observed in the high/soft state, as is discussed in Appendix A.

The optical SNRs identified from their [S II]:Hα line ratios are usually dominated by radiative shocks in the ISM. Very young SNRs, such as Cas A and E0102–72, which are still dominated by shocks within the ejecta, show strong [O III] emission instead. Blair et al. (2012) identified 46 emission nebulae that are possibly of this type, but only 6 (8) of those sources lie within $1''$ ($2''$) of an X-ray source. Of these sources, one is SN1957D (X279), and

therefore does not represent a new SNR identification. Several others, X044, X054, X135, have hard X-ray spectra, which makes a SNR identification less likely. An optical spectrum we recently obtained of B12-307, which is coincident with X044, indicates the X-ray source is *not* a SNR but a background AGN instead. None except SN1957D was detected as a radio source. However, several other oxygen-dominated emission nebulae are likely SNRs. The source X243, in the nuclear region of the galaxy, is spatially coincident with B12-321, which Dopita et al. (2010) reported as the first good candidate for a Cas A-like SNR in M83. Three other sources, X110, X341, and X360, also have soft X-ray spectra which support an identification as a SNR (even though a supersoft source designation cannot completely be ruled out).

Dopita et al. (2010), in an optical search for SNRs using *HST*/WFC3 interference filter images of the nuclear and inner eastern spiral arm regions of M83, identified 60 emission nebulae as likely SNRs, including the Cas A-like object coincident with X243, mentioned above. Of the 60 emission nebulae, 20 are located within the bright nuclear starburst region (within 200 pc of the nucleus), where the determination of [S II]:Hα ratios was especially difficult.[6] Of the 60 nebulae, 29 lie within $1''$ of sources in our *Chandra* survey. Of these, 14 are duplicates of sources we have already identified as SNRs based on the list compiled by Blair et al. (2012), and 15 have not been considered here previously. There are 5.3 chance associations expected in this crowded region of M83. Even given the small maximal position offset we have adopted ($1''$), two sources, D10-N08 and D10-N10, are associated with one X-ray source, X223. Most of the new identifications (12 of 15) are in the nuclear region. Because of the crowding near the nucleus, even as viewed with *HST*, and the difficulty of measuring [S II]:Hα ratios in these confused regions with bright backgrounds, we have chosen to limit the objects we identify as SNRs based on the *HST* imagery to those we feel on other grounds are most likely SNRs.

5.3.2. *Radio Supernova Remnants*

Of the 109 sources detected with ATCA, 36 (47) are coincident with X-ray sources within $1''$ ($2''$). By the criterion outlined above, we would expect 1.7 (4.9) of these coincidences to occur by chance. There is one X-ray source, X116 that could be associated with two radio sources, A031 and A032, but A032 is most likely the correct association given a position error

---

[6]The number 20 includes the Cas A-like source S03-70 which is not contained in the tables in Dopita et al. (2010), but discussed separately. We ignore the five additional objects with strong [O III] emission discussed by Dopita et al. as these are likely W-R nebulae instead of SNR candidates.

of only $0\rlap.''3$ compared to $1\rlap.''8$ for A031. Thus there are 46 X-ray sources that have ATCA counterparts. Of these X-ray sources, 21 are also in the list of sources already identified as SNRs from a comparison to the optical data. Their detection as radio sources solidifies their identification as SNRs.

All but one of the ATCA sources coincident with [S II] bright emission nebulae in Blair et al. (2012) are also detected as X-ray sources. This suggests, as do the total number of sources in the two surveys, that the X-ray observations have an overall sensitivity advantage over ATCA for detecting SNRs. The exception is A004 which lies within $2''$ of the [S II] dominated optical emission nebula, B12-004, but does not have an X-ray counterpart. This identification is recorded in Table 2; there is no reason to believe that A004 is not a SNR but further analysis is required to determine whether the upper limit on the X-ray flux at that position is significantly lower than the observed X-ray luminosities of other ATCA SNRs.

This leaves 25 ATCA sources coincident with X-ray sources that are *not* identified with [S II] dominated optical SNRs. Some of these, such as A108 and A109, are AGN or background galaxies; one is SN1957D (Long et al. 2012); and one, as discussed briefly later, one, A062 (=X237), is a newly-identified micro-quasar (Soria et al. 2014). The hardness ratios of the X-ray sources identified with ATCA sources is shown in Figure 6. Most have soft X-ray spectra, including essentially all of the objects also identified with optical SNRs. The sources identified with AGN, the micro-quasar, and SN1957D are the outliers. This suggests that a number of the other sources identified with radio sources are also likely to be SNRs. We have included seven of these sources in our list of candidate SNRs in M83, based on detection in the ATCA sample, their soft X-ray spectra and no indication from other data that they are not SNRs. These sources are X067, X078, X095, X097, X104, X169, and X275.

5.3.3.   Summary of SNR Identifications

Thus of the 378 X-ray sources within the D_{25} contours of M83, we identify a total of 87 as likely SNRs, based on the characteristics of their X-ray spectrum, an association with either an optical emission nebulae with the characteristics of a SNR and/or an association with a radio source in our ATCA data, and no strong contra-indications such as obvious X-ray variability. With the possible exception of M33, where Tüllmann et al. (2011) identified 45 SNRs using similar techniques to those employed here and where Long et al. (2010) identified 88 based on a targeted search for SNRs, this is the largest sample of X-ray SNRs in any external galaxy. A full discussion of the properties of these SNRs will be presented elsewhere.

5.4. Foreground and Background sources

Our deep X-ray images also show a number of X-ray sources that are background AGN and foreground stars. Here we discuss the identification of specific sources that can be recognized based on their appearance in other wavelength bands. The identification of AGN, the biggest source of contamination, is discussed in a statistical sense in Section 9.

Foreground stars are generally associated with soft X-ray sources and are visible as point sources in optical images. The numbers of such objects are expected to be relatively small given that M83 is approximately 31° from the Galactic plane. Background AGN generally have hard X-ray spectra similar to many XRBs and are often visible in optical images as long as a region is not confused by other emission.

In some cases, we were able to identify objects based on existing catalogs. For example, there are eight X-ray objects that are coincident with bright 2MASS sources well away from the optically bright portions of the galaxy; seven of these sources are clearly stars in our Magellan images. The other one is a background galaxy/AGN, listed in the Hyperleda catalog (Paturel et al. 2003) and the 6dF Galaxy Survey (Jones et al. 2009). A few other sources are also previously known AGN or background galaxies in these catalogs. In addition, as mentioned earlier, as part of an on-going study of the spectra of SNR candidates, we obtained a Gemini GMOS spectra of X044 and found it to be an AGN.

To obtain a more complete census of such objects, we have inspected the positions of the sources in the multiband Magellan images of M83, and made tentative identifications of a group of other objects. When we found an optical counterpart within the error circle of an X-ray source, we identified it as a likely AGN if the X-ray-to-optical flux ratio is between ~ 0.1 and ~ 10, and if the optical counterpart is an isolated blue object (under the assumption that isolated OB stars or young star clusters are not likely to be found far away from star-forming regions). In a few other cases, we found objects that appear extended in the Magellan images, and are thus consistent with a background galaxy, even though they appeared to be uncatalogued. Conversely if the isolated object appeared to be a star, and the X-ray to optical luminosity ratio was appropriate, we suggest a foreground star identification for the object. When the optical counterpart has unequivocal evidence of proper motion, for example in the USNO-B1.0 Catalog (Monet et al. 2003), or the NOMAD Catalog (Zacharias et al. 2004), or the PPMXL Catalog (Roeser et al. 2010), we identified it as a foreground star. In several cases, we also relied on the "probability of identification" (star, galaxy, quasar) listed in the Atlas of Radio/X-ray associations (Flesch 2010).

Not surprisingly the majority of the objects we classified in this fashion are objects outside the main body of M83. In the end, we found evidence that six of the X-ray sources

in the survey are stars, and that 56 are AGN/active galaxies. Many other objects are unidentified because they have no obvious optical counterparts.

In Table 6, we provide a census of the various source identifications in M83. Most of the objects identified within the D25 contour of M83 are SNRs, while most of those outside are identified with AGN/gaalxies.

6. Characteristics of the Bright Sources

Most of the 458 sources in the X-ray catalog are faint, and therefore for most of the sources, spectral analysis yields only a little more information than can be obtained from hardness ratios. However, 29 of the sources have more than 2000 counts, enough that detailed spectral fitting can be carried out. An additional 50 sources have between 500 and 2000 counts, not enough for really detailed fitting, but enough that one can learn more by fitting the spectrum than can be determined from simple hardness ratios. Hereafter, we will refer to the sources with >2000 counts as "bright" sources and those with between 500-2000 counts as "intermediate brightness" sources.

The spatial distribution of the bright and intermediate sources is interesting. Nine of the 29 bright sources and 13 of the 50 intermediate brightness sources are in the crowded starburst nuclear region, which we define as the region inside 0.4 kpc ($0farcm3$) from the center of M83. The remainder are distributed throughout the disk. Except for the concentration of objects in the nuclear region, the disk sources are distributed fairly uniformly across the disk of the galaxy, and are not particularly concentrated along the spiral arms or regions of most active star formation. Interestingly, one of the bright and 9 of the intermediate brightness sources are located outside of the D25 contours; some of these are background sources. However, because of the very extended outer disk structure seen in H I and by GALEX, these outer sources cannot automatically be disqualified from belonging to M83. As part of the source identification process discussed above, we have used the Magellan imaging data to search for optical counterparts, and indeed some AGN/background galaxies have been identified. However, the X-ray spectral analysis described below and the absence of an obvious optical AGN/galaxy identification allows us to identify a number of these outer sources as likely belonging to M83.

A thorough spectral analysis of the intermediate brightness and bright sources is beyond the scope of this overview report. However, we have carried out a preliminary analysis of the time-averaged spectra, as created by AE, which is intended as a guide for more detailed analysis to follow by ourselves or others.

For the 29 bright sources, we followed the following procedure. By inspection, we first determined whether the spectra showed evidence of lines or were relatively smooth. We then fit the spectra using XSPEC V12.8 (Arnaud 1996). In all cases, we fixed Galactic absorption N_H at 4.0×10^{20} cm^{-2} and included a second absorption component internal to M83 that was allowed to vary. We used the absorption model `tbabs` and `tbvarabs` for the Galactic and M83 absorption, respectively, and adopted the abundances of Wilms et al. (2000). A summary of the fit results for each source is given in the Appendix A; here we focus on the general motivation and physical interpretation of such analysis.

For the group of sources with spectra containing emission lines, with have fit the spectra with an optically-thin thermal-plasma model (`APEC`), in order to get a sense of the dominant temperature (usually in the range ~ 0.3–0.7 keV). In some cases, a single-temperature model was clearly inadequate and we had to add additional components: either a second thermal component or a power law. The physical interpretation of this class of models is either a young SNR (especially if relatively isolated) or a bright, compact starforming knot (especially in the nuclear region) which may include a number of unresolved SNRs and high-mass X-ray binaries.

A second group of bright sources (in particular, X237, X248, X284 and X286) showed featureless but strongly curved spectra that were well fit with an absorbed disk-blackbody model, with characteristic luminosity $\sim 10^{38}$ erg s^{-1}, peak color temperature $T_{\rm in} \lesssim 1$ keV and characteristic "apparent" inner-disk radius $r_{\rm in} (\cos\theta)^{0.5} \gtrsim 30$ km (where θ is the viewing angle to the disk plane, and the "true" inner-disk radius $R_{\rm in} \approx 1.2 r_{\rm in}$ Kubota et al. 1998). The physical interpretation of these sources is that they are stellar-mass BHs in the canonical high/soft state.

A third group of bright sources shows no evidence of lines and negligible broad-band curvature. They are well, or at least adequately, fit with an absorbed power-law model with characteristic photon index $\Gamma \sim 1.5$–1.7. A handful of those may be background AGN (*e.g.*, X038 and X138); the rest are probably XRBs. At first sight, the simplest physical interpretation for their spectral shapes would be that they are either NSs or BHs in the canonical low/hard state, defined by a power-law with similar photon index. However, this interpretation is almost certainly wrong for the most of sources in this sample, because they have X-ray luminosities of ≈ 1–2×10^{38} erg s^{-1}. This is too luminous for systems in the low/hard state, which is generally associated with luminosities $\lesssim$ a few 10^{37} erg s^{-1} in stellar-mass systems (unless some of them are intermediate-mass BHs, which we deem highly unlikely). Therefore, we suspect that the simple phenomenological power-law fit mimics a more complex physical model. In particular, based on our experience of XRB modeling, we investigated the possibility that the majority of the sources in this class are NS XRBs in a

high state, close to their Eddington limit. Unlike BHs, NSs have a hard surface; therefore, their spectra tend to contain two optically-thick thermal components (possibly modified by Comptonization): one from the inner disk and one from the boundary layer between disk and surface, or from the surface itself.

A simple way to model the spectra of this third group of sources is is to use a disk-blackbody plus a simple blackbody, or their Comptonized versions (*e.g.*, `diskir` and `comptt` in XSPEC). (See, for example, Lin et al. 2007; Barret 2001; Mitsuda et al. 1989; White et al. 1988, for detailed discussions on NS XRB spectral models.). The other characteristic feature of a NS XRB in the high state is that its inner-disk temperature is higher than that for a BH XRB. Compact objects of smaller mass have higher disk temperatures: at a fixed Eddington ratio (for example at $L \approx L_{\rm Edd}$), $T_{\rm in} \propto M^{-1/4}$, while at a fixed luminosity, $T_{\rm in} \propto M^{-1/2}$. When we tried fitting the same sample of sources with absorbed optically-thick thermal components (*e.g.*, disk-blackbody plus a simple blackbody), we obtained equally good fits as with an absorbed, hard power-law. Crucially, the characteristic temperatures of the best-fitting disk-blackbody components are $T_{\rm in} \sim 1.5$–2 keV and the characteristic sizes are $r_{\rm in} (\cos \theta)^{0.5} \sim 10$ km. Both values are consistent with the expected parameters of NS XRBs in their high state. It is intuitive to see why a hot disk-blackbody component may be mistaken for a hard power-law at low or moderate signal-to-noise. The peak of the disk-blackbody emission occurs at $E \sim 5$–6 keV; the continuum below the peak energy can be approximated with an absorbed, hard power-law, while the Wien curve above the disk-blackbody peak occurs in an energy range where *Chandra*'s sensitivity is very low, and does not constrain the model significantly. To quantify this hypothesis, we used the `fakeit` task in XSPEC to simulate the spectrum of a source with disk-blackbody parameters $T_{\rm in} = 1.8$ keV, $r_{\rm in} (\cos \theta)^{0.5} = 10$ km, total $N_{\rm H} = 8 \times 10^{20}$ cm^{-2}, 0.35–8 keV unabsorbed luminosity $\approx 2 \times 10^{38}$ erg s^{-1} (Eddington luminosity of a NS XRB) and simulated exposure time chosen to produce 2300 counts. We then re-fitted the spectrum with the original model and with an absorbed power-law model, and found that both models produce statistically acceptable fits; for the best-fit power-law model, the photon index was $\Gamma = 1.61 \pm 0.11$ and the inferred luminosity $\approx 3 \times 10^{38}$ erg s^{-1}. We conclude that apparent "hard-power-law" sources are indeed consistent with being NS XRBs in the high state. In some cases, though, the interpretation remains ambiguous (Appendix A).

For the intermediate brightness sources, our approach has been more abbreviated. We performed automated spectral fits in `XSPEC` with a non-thermal model (`powerlaw`), an optically-thin thermal-plasma model (`APEC`), and an accretion disk model (`diskbb`). As for the brightest sources, each model included an absorption component for the Galaxy fixed at $N_{\rm H}$ of 4.0×10^{20} cm^{-2}, another absorption component internal to M83 that was allowed to vary. We used the absorption model `tbabs` and `tbvarabs` for the Galactic and M83

absorption, respectively, and adopted the abundances of Wilms et al. (2000).

We examined the fit results and classified the spectra by which model resulted in the best fit and physically reasonable parameters. For example, we selected the thermal-plasma model for fits that resulted in power-law indices $\Gamma > 3.0$ and fitted temperatures for the thermal-plasma model $kT < 2.5$ keV, even if the fit statistic for the power-law model might have been slightly lower. Conversely, we selected the power-law model for fits that resulted in photon indices < 3.0 and fitted plasma temperatures > 2.5 keV. For some spectra with a distinctly curved continuum, the disk-blackbody model resulted in a significantly better fit than either the power-law or thermal-plasma model. This typically occurred for spectra with a large number of counts such that a deviation from a pure power-law could be detected.

As for the brightest sources, the intermediate-luminosity sources that are best fitted by a pure thermal-plasma model are probably either individual SNRs or compact knots of hot gas in dense star-forming regions. The sources for which the disk-blackbody model provides the dominant component are most likely XRBs in a high state. The sources that are best fitted by a pure power-law (typically, with photon index ~ 1.5) are a mixed bag and we cannot give a general physical interpretation based on X-ray modeling alone: some of them may be NS XRBs with optically-thick thermal emission at $T \gtrsim 1.5$ keV as discussed earlier; others (especially sources with only ~ 500 counts) may be BH XRBs in the low/hard state, at $L \sim$ a few 10^{37} erg s^{-1}; a few others might be high-energy pulsars and pulsar-wind nebulae (Crab-like sources), which have a synchrotron power-law X-ray spectrum and can also reach X-ray luminosities $\sim$ a few 10^{37} erg s^{-1}; and finally, some of the power-law sources are background AGN.

In conclusion, we summarize our results by classifying the sources into six spectral categories depending on their best-fit model: "P" non-thermal (power-law); "T" optically-thin thermal-plasma; "D" disk-blackbody; "P/D" either power-law or disk-blackbody with similar statistical likelihood; "P/T" either power-law or (hot) thermal-plasma; "P+D" power-law plus disk-blackbody. These classifications are listed in Table 5. Of the 79 sources fitted, 38 were best fit by a power-law model (P), 18 by a thermal-plasma model (T), and 11 by a disk-blackbody model (D). Six were inconclusive between a power-law and disk blackbody (P/D), two were inconclusive between a power-law and a thermal-plasma model (P/T), and four were best fitted by a combination of power-law and disk-blackbody models (P+D). This type of spectra classification is crude, because (as explained earlier) the power-law model is often degenerate with disk-blackbody or Comptonization models, and thus completely different classes of physical sources can end up in the same group. Nonetheless, it provides a simple spectral classification that can be used for monitoring luminosity and spectral changes in future observations of M83, and to in some cases for comparisons between X-ray source

populations in different galaxies For reference and to show the diagnostic power of the fits, Figure 8 shows examples of the model fits for two bright and two intermediate brightness sources.

7.   Nuclear Region

The bright nuclear region of M83 is a complex and dynamic environment (Harris et al. 2001; Dottori et al. 2008; Knapen et al. 2010; Wofford et al. 2011), and exhibits a complex X-ray and optical morphology involving point sources of various types as well as diffuse emission in both bands (Soria & Wu 2003; Houghton & Thatte 2008). Many massive, young star clusters imply an age gradient and a distributed burst of star formation, much of which is hidden from direct view by dust, especially to the north. Dopita et al. (2010) have identified some 20 SNRs in the nuclear region using HST/WFC3 imagery, as well as tentatively identifying the optical counterpart of SN1968L, as mentioned earlier. For our purposes, we choose the nuclear region to be represented by the inner 0.4 kpc ($\sim$0.′3) of the galaxy, which includes the entire bright starburst region, as well as a population of older stars that comprise most of the bulge the of the galaxy (e.g. Figure of Knapen et al. 2010).[7] This region is shown in Figure 7, where three-color versions of the Magellan broadband and $Chandra$ data (unsmoothed and smoothed) are provided, with scaling to show the brightest emissions that are mostly saturated in the wider field images provided earlier.

A reddish optical cluster and X-ray source X233 are coincident with the optical nucleus (ON), which is identified by the red circles in Figure 7. An optical SNR (Table 3 #15 from Dopita et al. 2010) also nearly aligns with the ON. The kinematic center (KC) of the nuclear region lies some 3.″7 to the WSW (see, e.g. Thatte et al. 2000; Knapen et al. 2010; Piqueras López et al. 2012, and references therein). Furthermore, a second mass concentration, dubbed the "hidden nucleus" or HN by Dottori et al. (2008), was identified by Mast et al. (2006) some 3.″9 west of the ON. The relative positions of the KC and HN, reconstructed from the original references, are shown by the blue circles in the left panels of Figure 7.[8] Neither of these two positions has a specific X-ray counterpart, although both are within the bright, clumpy soft X-ray emission in the nuclear region energized by both

---

[7]We discuss the cumulative luminosity function of sources in the nuclear region, and the rest of the bulge in Section 9.3.2.

[8]Note that the relative positions of the ON, KC, and HN as shown in Figure 2 of Dottori et al. (2008) do not agree with the positions shown in Thatte et al. (2000) and Mast et al. (2006). We have carefully reconstructed the relative positions by referring back to the original figures in these references.

the SNR population and the strong stellar winds from all of the young massive stars.

We have identified a large number of X-ray point sources within the nuclear region. However, given both the complexity and the appearance of the region, not all of these may be physically distinct individual objects and we also may be missing sources that would be detected if they were more isolated. iAs indicated in Figure 7, there is very strong diffuse emission in the nuclear region; some of these sources (those whose spectra show strong emission lines) may simply be peaks in the bright diffuse thermal emission the permeates the nuclear region. Nine of the sources in the nuclear region are in our bright (2000 counts) group, and 13 are in the intermediate group discussed above, and are clearly detected above the bright diffuse X-ray background in the region. Significant dust lanes are also evident in the Magellan data, and these are no doubt also responsible for shaping the character of the X-ray emission. Since we don't know where each X-ray source is along the line of sight, some sources may appear harder in X-rays than they really are, depending on the foreground absorption. However, large regions are nearly free of overlying dust, and so some sources, especially on the near side of the nucleus, may not have excessive column densities.

Figure 7 shows an overlay of X-ray source regions, and the potential for confusion of identification of individual objects is obvious. Despite the source crowding even at *Chandra* resolution, we have inspected the positions of all of the nuclear sources against the optical (Magellan) broadband data, as well as the Dopita et al. (2010) SNR list to provide context for the possible identifications. For the bright sources, brief descriptions are provided as part of the notes in Appendix A. Even for these bright sources, we describe how alignments with optical SNRs or other structures may be chance coincidences, given the fits to the X-ray spectra. (For instance, see sections on objects such as X216, X233, and others.) The spatial alignments for nuclear sources are annotated in Table 5.

In Figure 7 (right panels) we show green and magenta regions that correspond to the *Chandra* nuclear sources. Green circles are identified with regions of star formation, including a few that align with actual clusters. Magenta circles indicate those sources that align with SNRs. (Note: some sources align with both star formation and SNRs.) Sources X186, X207, X212 and X250 all align with Dopita et al. (2010) SNRs and are relatively soft sources on the fringes of the nuclear region. These are probably fairly solid IDs with SNRs. X243=S03-70 is a special case identified by D10: a compact oxygen-enhanced emission nebula that is a likely cousin to Cas A in our Galaxy. X237, the magenta circle to the upper left of the field center, corresponds to a relatively hard X-ray source (turquoise in the figure). It aligns with an optical source that had been identified as a SNR by Dopita et al. (2010); however, our multiwavelength assessment (including radio, *Chandra*, and *HST* data) now points to its being a newly-identified microquasar MQ1 (Soria et al. 2014). The apparently hard

spectrum is primarily due to the fact that the source lies behind considerable absorption. Its intrinsic spectrum can be modeled in terms of disk-blackbody models with kT of about 0.7 keV. Several green circles align with bright white (medium-hard) X-ray sources and are likely XRBs, but without specific optical counterparts, they have been labeled as star-formation regions. Finally, we highlight two hard (blue) X-ray sources, X242 on the SE fringe of the nucleus and X225 in the north, both of which are projected onto dark dust lanes. At least part of the spectral hardness of these sources may be due to absorption, assuming these sources are behind the dust.

Because of the overall complexity of the nuclear region of M83, a future dedicated study using all available multi-wavelength data is warranted.

8. Other Soft and Very Soft Sources in the Disk

As discussed in Section 5.3, we have classified 87 objects as likely SNRs, based on existing catalogs of SNRs in M83 and absence of evidence that would suggest an object is not a SNR. Of these, 79 SNRs lie within the D_{25} contours of the galaxy but outside the nuclear region, and of these, 72 have (M–S)/T hardness ratios of -0.5 or less.[9] There are a total of 154 sources in the catalog that have (M–S)/T hardness ratios of -0.5 or less and that lie within the D_{25} contours of the galaxy but outside the nuclear region. Here we discuss the nature of the 82 soft sources in the disk, which are not classified as SNRs. Soft sources in the vicinity of the nucleus have been discussed in Section 7.

What are the remaining soft sources likely to be? There are at least three possibilities: (a) currently unidentified SNRs, (b) true supersoft sources, that is binary X-ray sources with very soft spectra, or (c) peaks in the diffuse gas emission, possibly due to specific star formation regions that have been characterized as point-like. We note in passing that some of these same questions have been asked previously by Di Stefano & Kong (2004) who analyzed the archival data for M83 and a number of other galaxies in a search for supersoft X-ray binaries. Using hardness ratio based criteria, they identified 53 very soft sources (VSSs) in M101, 23 VSSs in M51, 19 VSSs in the elliptical galaxy NGC4697, and (using the archival data) 54 VSSs in M83.[10]

---

[9]There are seven SNRs, including X279, identified with SN1957D, that have higher values of (M–S)/T. There are eight SNRs within the nuclear region.

[10]The energy bands that Di Stefano & Kong (2004) used were S = 0.1-1.1 keV, M=1.1-2.2 keV, H=2-7 keV. They required a VSS to have (M-S)/(M+S)<0.8 and (H-S)<0.8. Although our bands are slightly different, we follow Di Stefano & Kong (2004) and denote sources that have (M-S)/(M+S) ratios < −0.88

Soria & Wu (2003) identified two sources, S03-068=X240 and S03-096=X312 as super-soft sources, based on all their counts occurring at energies below 1 keV. Both have (M–S)/T hardness ratios of −1 in the full dataset, consistent with this identification. Interestingly, both appear to be variable, with more flux in the archival data than in the more recent observations. This suggests that these two sources, at least, are true supersoft sources. A total of 17 of the 82 soft sources in the disk not identified with SNRs show time variability, as compared to only seven apparently variable sources among the 87 objects that we have suggested are SNRs. X365 appears to be a "classical transient"; S03-38=X162 and S03-124=X393 were detected in the early observations with *Chandra*, but not the more recent observations, while X273 was seen in the new observations but not the archival data. Variability suggests that at least 20% of the soft sources in the disk are binaries. The median value of the (M–S)/T hardness ratio of the 17 variable sources is -0.99, consistent with many of them being supersoft sources.

Both the SNRs and the other soft sources show marked concentrations in the spiral arms. Of the objects with (M–S)/T≤ -0.5, those that are not identified with SNRs tend to have lower hardness ratios than those that are identified with SNRs. The median hardness ratio for the soft sources (M–S/T≤ -0.5) which are not identified with SNRs is -0.88 while the median for SNRs is -0.83 (or -0.85 if the SNRs with (M–S)/T> -0.5 are excluded). The SNRs are somewhat harder on average than the other sources. Of the 87 SNRs, there are 49 with hardness ratios > -0.88 and 28 with values less than this. However, a two-sided Kolgoramov-Smirnov test comparing the hardness ratios of SNRs with (M–S)/T≤ -0.5 to other sources with M–S/T≤ -0.5, yields a probability (p-value) of 11%, implying we cannot distinguish the underlying source populations on the basis of hardness ratios, and providing some support for the hypothesis that many of the other soft sources are unidentified SNRs.

We have created composite, or more specifically summed, spectra for the objects identified with SNRs and those which are not, dividing each of these groups into those that are soft $-0.5 > (M–S)/T > -0.88$ and those that are very soft $-0.88 > (M–S)/T$. The four spectra are shown in Figure 9. It is quite clear that the composite spectrum of the soft sources (with (M–S)/T between -0.88 and -0.5) not identified with SNRs ("Soft, not SNRs") is very similar to spectra from those identified with SNRs ("Soft SNRs"), suggesting that many of the "Soft, not SNRs" sources are actually SNRs whose optical and radio emission is too faint to have been detected. The shape of spectrum of the very soft sources not identified with SNRs ("Very Soft, Not SNRs") differs from the very soft sources identified with SNRs ("Very Soft SNRs"), particularly near 0.5 keV. Although there could be a substantial con-

---

in our bands as very soft sources, to distinguish them from true supersoft sources.

tribution from unidentified SNRs to the "Very Soft, Not SNRs" spectrum, there must also be a large contribution from some class of sources whose spectrum is similar to a blackbody. A crude blackbody fit to the "Very Soft, Not SNRs" spectrum, fixing foreground absorption at $4 \times 10^{20} \, \text{cm}^{-2}$, yields kT of about 0.1 keV.

In the absence of a much more detailed multi-wavelength analysis, we cannot rule out the possibility that some of the unidentified soft and very soft sources are simply peaks in the diffuse emission, which arises from hot gas, and is also concentrated in the spiral arms. By definition, we do not have ancillary information on these objects to show they are SNRs. A preliminary extraction of the spectrum of the diffuse emission, with the point sources removed, yields a (M–S)/T hardness ratio of -0.93, similar to many of the softest point sources, and which might be associated with the feature near 0.5 keV in the "Very Soft, Not SNRs" spectrum. However, the diffuse emission spectrum shows features due to the lines of O VII and O VIII at 0.56 and 0.65 keV, as well as a feature at 0.82 keV, which is likely due to Fe XVII, but these are not not seen in the "Very Soft, Not SNRs" spectrum. In the absence of more evidence, our belief is that this group of sources is dominated by a mixture of SNRs and supersoft sources, with the possibility that a few of the softest sources are peaks in the diffuse emission.

9. Luminosity Function

The cumulative luminosity function (CLF) of the sources in M83 reflects the evolution history of the types of objects that produce X-ray sources, which, with the exception of the stars that produce SNRs, are almost entirely binaries (see, e.g., Fabbiano 2006, for a recent review of normal galaxy X-ray populations). There are currently several approaches to such analyses. One approach involves modeling the star formation history itself, (e.g. Tzanavaris et al. 2013) which is beyond the scope of the present effort. Here, we consider two simpler techniques, more appropriate for a first look at the CLF of M83.

The first, developed by Grimm et al. (2002, 2003) and by Gilfanov (2004), utilizes differences in "canonical" luminosity functions of low-mass X-ray binaries (LMXB) and high-mass X-ray binaries (HMXB) to estimate the fraction of each of these source types in different galaxies. The CLF of HMXB is described by a power law $N(> L) \propto L^{-\alpha}$, with an index $\alpha = 0.64 \pm 0.15$ and no obvious cutoff at high luminosity. The CLF for LMXB has a flatter slope $\alpha = 0.26 \pm 0.08$ and a distinct cutoff at about $10^{37.5}$ ergs s^{-1} (Grimm et al. 2002). These canonical luminosity functions have been applied to strongly star-forming galaxies, thought to be dominated by HMXB (Grimm et al. 2003) and older stellar systems, thought to be dominated by LMXB (Gilfanov 2004). Mixed systems should be characterized by

luminosity functions that are a combination of these.

The second focuses simply on changes in the index of a power law fit to the CLF. For example, Kilgard et al. (2002, 2005), using a small sample of spiral galaxies, found that the CLFs of starburst galaxies, such as M82 and the Antennae, have an index of ~ 0.5, while "star-forming" galaxies, a group comprising M51, M83, and M94, have indices of ~ 0.6, similar to that of the canonical HMXB CLF determined by Grimm et al. (2002). Spiral galaxies with lower star-formation rates have higher indices, typically ~ 1.2. Since many luminosity functions do not extend below 10^{37} ergs s^{-1}, evidence for the 'break' in the power law due to LMXBs can be confused by completeness issues. In these cases, the index may then reflect the joint contribution from the index characteristic of HMXB and higher index characteristic of LMXB above the break.

The CLF of M83 above about 5×10^{36} ergs s^{-1} has been described by Soria & Wu (2003) and by Kilgard et al. (2005) using the early *Chandra* observations. Both concluded that the overall CLF is a broken power law. Soria & Wu (2003) find an index of ~ 0.6 below the break, and steeper index, 1.6, above the break[11]. Kilgard et al. (2002) found an index of 1.4 above the break and, ignoring the break, a mean slope of 0.6. Soria & Wu (2003) found that the CLF of the inner disk and nucleus (within 60″ of the nucleus) could be fit with a pure power law, with a slope of 0.7 and no break, which they suggested was due to the influence of a large population of HMXBs. They also suggested that the break in the CLF of the disk outside this region might be due to multiple epochs of star formation.

With our new *Chandra* observations, we can now extend the luminosity function to luminosities below 10^{36} ergs s^{-1}, can remove the contributions from foreground and background objects, and can explore the CLF as a function of position in more detail. For this analysis, we consider only the sources within the D$_{25}$ contours, beyond which, as shown in Figure 11, the surface density of sources becomes indistinguishable from that expected from the background. To permit effective comparisons with other studies, we have calculated luminosity functions in three bands, 0.35-8 keV, 0.5-2.0 keV, and 2-8.0 keV. Unless otherwise indicated, however, our comments refer to the 0.35-8 keV broad band.

We constructed CLFs from the mean fluxes listed in Table 4 for the combined *Chandra* data. We converted fluxes to luminosities using the power law spectrum described in Section 4.1. Due to telescope vignetting and the change of roll angles between observations, there is some variation in the sensitivity of our observations across the face of M83. To account

---

[11]Despite obtaining indices from fitting differential luminosity functions, we quote the indices for the cumulative luminosity function in order to be consistent with current literature, and to allow ready comparison with the plots.

for this variation, we calculated the point source detection limit as a function of position. Using this method, we calculated the fraction of the area over which a source of a given luminosity would have been detected, and used this assessment to correct the luminosity function for incompleteness. We have set our sensitivity limit to be the luminosity for which the area correction factor was less than 10%. This varies from region to region, ranging from 6.4×10^{35} ergs s^{-1} for the bulge region to 10^{36} ergs s^{-1} for the outer disk. (See Table 7).

The total CLF for the 0.35-8 keV band is shown in Figure 10. The luminosity scale for sources in M83 is shown on the upper axis. The total CLF includes not only sources within M83, but also a contribution from background AGN and foreground Galactic stars, which must be removed to determine the CLF of M83. The total CLF also includes SNRs, which are usually ignored in attempts to explain X-ray sources populations in normal galaxies. The SNRs also need to be removed in order to study the X-ray binary populations.

9.1. Removing Background Sources from the CLF

Although we have identified a number of AGN and background galaxies as point sources in our M83 sample, most of these are outside of the D25 ellipse. The hardness ratios of AGN are expected to be similar to those of the XRBs and we do not have enough ancillary information to identify most of the AGN that are expected within the D25 ellipse. Therefore AGN have to be removed statistically. The number of background AGN expected in our catalog depends upon the intrinsic flux distribution of the background AGN as well as the point source detection limit and galactic absorption as a function of position in the galaxy. For our estimate, we used the intrinsic flux function (log N-log S) obtained by Kim et al. (2007), since they provide number counts for our bands of interest. We estimated the absorption due to M83 from a map of total hydrogen column density obtained by Lundgren et al. (2004).

To establish the background point source limit at each position in M83, we approximated the process used by AE to create the source catalog. Specifically, at each $0\rlap{.}''492 \times 0\rlap{.}''492$ pixel in our image mosaic, we first determined the local background rate using the same method as AE. We then calculated the minimum number of counts that a source at that location would need in order to have a probability of no source $< 5 \times 10^{-6}$ in the sum of the individual observations. Finally, we converted counts into fluxes using the exposure maps of each chip for each observation, to produce point source detection limit maps for our three bands of interest. From this point source detection limit, we calculated the number of AGN at each flux in $\Delta \log F = 0.1$ bins, using the intrinsic flux functions in Kim et al. (2007) at each image pixel.

From this calculation, we estimate that 97 AGN are among the 378 sources detected with *Chandra* in the 0.35-8.0 keV band within the D_{25} region. The intrinsic broad band luminosity function of M83, with the contributions from AGN, known foreground stars, and known SNRs all subtracted, is shown as the dashed line in Figure 10. There is some cosmic variance in the normalization of the AGN function at different locations in the sky. To see if this is a problem in the direction of M83, we calculated the predicted number of sources outside the D_{25} region using the Kim et al. (2007) flux function to get 59, reasonably consistent with the 54 actually identified. In Figure 11, we show the radial profile of the observed sources in M83 along with the number of sources predicted from the flux function. If anything, we seem to have overestimated the AGN contamination slightly.

9.2. Removing SNRs from the CLF

In most X-ray observations of galaxies, the numbers of SNRs detected are relatively small, and as a result the effect of SNRs on the CLF is usually ignored. However, SNRs constitute a significant fraction of the sources in M83, and must be removed from the CLF, if we want to examine the CLF of XRBs.

The left panel in Figure 10 shows the relative shapes of the CLFs for all the sources, for AGN alone, and for SNRs alone. The right hand panel shows the effects of removing the AGN and foreground stars from the CLF and of removing the SNRs in addition. The slope of the SNR-only CLF is very steep and does not significantly affect the broad band luminosity function above $10^{36.8}$ ergs s^{-1}, but it it flattens the CLF at lower luminosities. In the discussion of XRBs in M33 below, we have removed only the 87 sources we have specifically identified as SNRs. We will return to the effect of removing the "Soft, Not SNR" and "Very Soft, Not SNR" sources from the CLF for XRBs in Section 9.3.4, simply noting here that this would flatten the CLF even more.

9.3. The CLF of XRBs in M83

Having removed the AGN and (the majority of) SNRs, we now consider the CLF of the XRBs in M83. The corrected CLF (the green histogram in the right hand panel of Figure 10) resembles that of Soria & Wu (2003) and Kilgard et al. (2005) above 10^{37} ergs s^{-1}, as expected, even though Soria & Wu (2003) did not remove AGN and neither removed SNRs, both of which become important at luminosities below 10^{37} ergs s^{-1}. The shape of the CLF for all sources within the D_{25} radius can be roughly characterized as a power law below

$10^{37.5}$ ergs s^{-1} with progressively higher indices at higher luminosities.

To quantify our results, we have fit the differential luminosity function with a maximum likelihood method similar to that outlined in Kilgard et al. (2005).[12] Since the AGN must be removed statistically, and the maximum likelihood method requires integral sources (Crawford et al. 1970), each fit cited here is the result of 1000 trial fits, each of which is made to the data from which the AGN have been removed. We have used the distribution of the fits of individual trials to set the uncertainties.

The fit to the corrected CLF within D$_{25}$ yields an index of 0.41 ± 0.02. Restricting the fit to luminosities below $10^{37.5}$ ergs s^{-1} yields an index of 0.50 ± 0.02. This slope is intermediate between that expected for a pure HMXB population and a pure LMXB population, and the difference in slope reflects the break expected for LMXBs. Had we excluded all of the soft and very sources ("Soft, Not SNRs" and "Very Soft, Not SNRs") from the CLF, which would be the correct thing to do if most of these sources are unrecognized SNRs, then the slope for XRBs below $10^{37.5}$ ergs s^{-1} would have been shallower still, with an index of 0.15 ± 0.03. This would imply, within the context majority of canonical descriptions of X-ray CLFs, that the majority of XRBs in M83 are LMXBs, a point we discuss in more detail Section 9.3.4.

The mixture of high and low mass X-ray binaries typically varies as a function of position in galaxies, depending on the local star formation history. In particular, bulges and disks generally reveal different luminosity functions, e.g., M31 (Kong et al. 2003) or M81 (Tennant et al. 2001), with bulges more dominated by LMXBs, and star-forming disks more dominated by HMXBs. We have constructed CLFs of the XRBs for various regions of M83 to investigate this. The results are shown in the upper left, upper right, and lower left panels of Figure 12 for the 0.35-8 keV, 0.5-2 keV, and 2-8 keV bands, respectively. In constructing the various CLFs, we have only used sources that were detected with high confidence (probability-of-no-source $< 5 \times 10^{-6}$) in that energy band. Unless otherwise indicated, the following discussion refers to the 0.35-8 keV band.

9.3.1. Comparison of the CLFs in Different Energy Bands

As shown in Figure 12, the CLF derived from the 0.5-2 keV range is almost identical to that in the full spectral range, 0.35-8 keV. This is not surprising since Chandra is most

---

[12]We, as do many others, perform fits to the differential luminosity function rather than the CLF because the points in a cumulative luminosity function are not statistically independent of one another. We quote results in terms of the cumulative luminosity function since this is the historical practice.

sensitive in the range 0.5-2 keV, which is contained within the broader band. The CLF derived from the 2-8 keV band has less structure than the broad and 0.5-2 keV CLFs and follows a simple power law to nearly its highest luminosities. Similar behavior is observed in NGC300 (Binder et al. 2012). However, we do not find a difference in slope between the 0.35-8.0 and 2-8 keV band CLFs; for M83 both have indices of 0.61 ± 0.03. *Chandra* is less sensitive in the 2-8 keV range, and as a result, the CLF does not extend to as faint a limit in this band.

9.3.2. The CLF of the Bulge and Nucleus of M83

Although the nuclear starburst is expected to produce a significant number of young high-mass X-ray binaries, one expects a substantial number of low-mass binaries from the old stellar population forming the bulge. As in Section 7, we take the nuclear starburst to occupy the inner $0\rlap{.}''3$. In the optical, the surface brightness of the bulge has circular isophotes out to at least r=$0\rlap{.}''6$ and has a profile approximating that of an $r^{1/4}$ power law (Jensen et al. 1981). Since the bulge has a broader distribution than the nuclear starburst, one might expect the mixture of populations, and thus the CLFs to vary with radius. Given the strength of the starburst, one expects the young population to dominate at smaller radii.

As shown in Figure 12, the 0.35-8 keV CLF of the combined bulge and nuclear region is relatively flat with increasing indices above $10^{37.5}$ ergs s^{-1}. This CLF stands in apparent contrast with the simple power law found by Soria & Wu (2003) within $1\rlap{.}''0$, however, the break in our CLF is near the limiting luminosity of the Soria & Wu (2003) CLF. A power law fit to the data below 10^{37} ergs s^{-1} yields a power law index of 0.19 ± 0.04. The power law indices are not significantly steeper in the 0.5-2 keV band but are in the 2-8 keV band. The break is also more abrupt in the 2-8 keV CLF, than in the other energy bands. Thus, in terms of the simple prescriptions described by Grimm et al. (2002), it appears that the CLF of the bulge and nuclear region of M83 resembles that expected for an X-ray source population dominated by LMXBs. This result suggests that the bulge dominates over the starburst.

In light of this unexpected conclusion, we constructed the CLFs separating the inner starburst region from the outer region which is presumably more bulge dominated. The outer bulge region was set to be $0\rlap{.}''3 < r < 0\rlap{.}''6$, while the starburst was set to be $r < 0\rlap{.}''3$. The CLFs are shown in Figure 14. The 0.35-8 keV CLF of the inner nuclear starburst is quite flat with with a break at $\sim10^{37.3}$ ergs s^{-1}, while the 0.35-8 keV CLF for the outer bulge region is a well fit by a power law with a rather steep index of 0.84 ± 0.02. A Kolmogorov-Smirnov test shows that the two CLFs are not drawn from the same distribution to a high degree of

confidence. The CLF of the inner region resembles that of a canonical LMXB CLF, while the outer region resembles that expected from HMXB.

That the CLF of the outer bulge is not dominated by an old population suggests that the bulge population is either weak or more centrally concentrated. That the CLF of the starburst region is dominated by an old population is more problematic, and requires a closer consideration of observational factors. If the nuclear region were an intrinsic power law CLF, then our observed CLF would be missing faint sources. Missing faint sources is not unreasonable given the bright diffuse emission and confusion in the center of the nuclear region. Both issues are of more concern for the soft band than the hard band. To avoid source confusion issues, one requires less than 3-10% of the region to be occupied by sources depending on the slope of the CLF (see, e.g. Takeuchi & Ishii 2004). Assuming source radii of an arc second, sources cover 12% and 7% in the soft and hard bands respectively. The source coverage increases to $\sim 23\%$ in both bands as the radius of the nuclear region is decreased to $0\rlap{.}''1$. Thus we have significant confusion issues, particularly in the inner nucleus. Thus the true shape of the CLF in the nuclear starburst is ambiguous.

9.3.3. The CLF of the Disk

Outside the nuclear region, one might expect the situation to be simpler, with HMXBs prominent in the spiral arms and LMXBs in the interarm regions. We define the disk as the region outside of the bulge, but inside the D_{25} radius. As shown in Figure 12, the disk CLF does not appear to be a simple power law with a cutoff. Instead, the slope is steeper below $10^{36.5}$ ergs s^{-1} (96 sources, index $\sim$1.0) than between between $10^{36.5}$ and 10^{38} ergs s^{-1} (56 sources, index $\sim$0.4), where there is a break and the CLF steepens once again (19 sources, index $\sim$0.7). These features are not due to small-number statistics. The detailed structure structure cannot be explained easily within the context of the canonical LMXB/HMXB luminosity functions, but the break near $10^{37.5}$ ergs s^{-1} is the break associated with LMXB.

We have attempted to clarify our understanding of the CLF for the disk by considering subregions shown in Figure 13. As shown in Figure 12, the inner disk (the sum of the arm and inter-arm CLFs) and the outer disk have similar CLFs, save for the sharp increase in the number of sources in the lowest bin of the outer disk. The inner and outer disk CLFs are even more similar in the 0.5-2 keV band. Significant differences do appear in the 2-8 keV band; the inner and outer disks have very different indices, with the outer disk having a steeper index of 0.83 ± 0.06 and the inner disk having a shallower index of 0.24 ± 0.02. The inner disk does show the same type of roll-off at the higher luminosities seen in other bands. The difference between the 0.5-2 and 2-8 keV bands suggests a color difference between the

inner and outer sources, and that one should be aware of band pass effects when comparing results of different observers using different bandpasses. Any radial effects, such as changes in metallicity and star-formation history, are indistinguishable in the CLFs.

We also divided the inner disk into arm and inter-arm regions (see Figure 13). In the 0.35-8 and 0.5-2 keV bands, the arm CLF shows the increased index below $10^{36.5}$ ergs s^{-1} that is seen for the overall disk CLF, while the inter-arm CLF does not. Thus the $10^{36.5}$ ergs s^{-1} inflection is due to sources in the arms. Neither the arm nor inter-arm CLF has a slope as steep as expected for an HXRB-dominated population. Thus, a perhaps naïve expectation of finding HMXBs preferentially in the arms is not confirmed.

9.3.4. The Effect of Soft Sources on the CLF

In constructing the CLF of X-ray binaries in M83, we have excluded the 87 objects identified as likely SNRs. However, many more of the soft and very soft sources in our sample may also be SNRs (see Section 8). The lower right hand panel of Figure 12 shows what happens to the CLF if all sources with hardness ratio (M–S/T)< -0.8 are removed from the sample. Specifically, the disk CLF in the broad band becomes a broken power law with an index of 0.24 ± 0.08 below the break, a break at $10^{37.6}$ ergs s^{-1}, and an index of 0.61 ± 0.05 above the break. Since the soft sources are preferentially faint, the main effect of their removal is to flatten the CLFs, making the corrected CLF of M83 look even more like that expected for an LMXB population.

This effect is particularly strong in the disk, since many of the soft sources are located there. Moreover, the CLF shapes from the different subregions of the disk look much more similar. There is, for example, virtually no difference in the CLF for sources in the arm and inter-arm regions once the soft sources have been removed. This is consistent with the hypothesis that a majority of the binary X-ray sources in M83 are associated with older source populations. The corollary is that soft sources are sensitive to environment (and possibly to the existence of a young stellar population), and are thus found preferentially in the arms. It should also be noted that the bulk of these soft sources are not detected in the hard band, so removing these sources has little effect on the hard band CLFs.

9.4. Summary and Further Discussion of the CLF of M83

Our results on the CLF of M83 can be summarized as follow:

- The CLF of the nuclear starburst and bulge of M83, as derived from our point source catalog, resembles, *prima facie*, that of a population of LMXB. However, this result appears to be misleading, reflecting, primarily, the effects of source confusion in the innermost $0\!\!.\!3$ and the bright, diffuse, strongly structured background there. In fact, the outer bulge (the region between $0\!\!.\!3$ and $0\!\!.\!6$ of the center) surrounding the inner nuclear starburst region has the power law luminosity function expected from a HMXB population.

- The CLF of the disk shows a complex shape, with an inflection at $10^{36.5}$ ergs s^{-1} and a break at $10^{37.5}$ ergs s^{-1}. The $10^{37.5}$ ergs s^{-1} break is common to all the subregions of the disk, and appears to be a fundamental characteristic of the M83 XRB population. As this break is at roughly the luminosity expected for the break in the canonical LMXB luminosity function, the interpretation may be straight-forward. The $10^{36.5}$ ergs s^{-1} inflection is stronger in the arms than in the inter-arm regions, and disappears if one removes the soft and very soft sources. We suspect that a large fraction of the soft sources and part of the very soft source population (not currently identified) are in fact SNRs, and their association with spiral arms supports this hypothesis. The true XRB CLF below $10^{37.5}$ ergs s^{-1} is thus likely to be more like the CLF with the soft and very soft sources removed than the CLF. The CLF for the XRBs in the disk of M83 is thus well characterized as a broken power law. The index below the break is consistent with that of canonical LMXB luminosity functions, as is the break luminosity. That the index above the break does not roll off as quickly as the canonical LMXB luminosity function indicates the presence of *some* HMXB despite the dominance of LMXB. We would have significantly overestimated the HMXB contribution had we not removed (the majority of) the SNRs.

Since M83 clearly has a mixture of HMXBs and LMXBs, we may test the extent to which scaling of the canonical HMXB and LMXB luminosity functions (Gilfanov 2004; Grimm et al. 2003) provides a reasonable match to our observed CLFs. Gilfanov (2004) provides the canonical LMXB luminosity function with a normalization per galactic stellar mass (as measured from the K band luminosity) while Grimm et al. (2003) provides the canonical HMXB luminosity function with a normalization per unit star-formation rate. The Milky Way version of these functions are only slightly different and extend to $\sim 3 \times 10^{35}$ ergs s^{-1}. Our estimate of the mass in stars follows directly from from the K-band magnitude, which we take to be 4.62 from the 2MASS Large Galaxy Catalog (Jarrett et al. 2003), the distance to M83, the absolute K magnitude of the Sun (3.39), and a mass-to light-ratio estimate of 0.59 for M83 based on the B − V color of the galaxy (Bell & de Jong 2001). We expect M83 to have a stellar mass of 4×10^{10} $M_\odot$. We take the star-formation rate of 3.5 $M_\odot \mathrm{yr}^{-1}$ from

the value of 3-4 $M_\odot \mathrm{yr}^{-1}$ estimated by Boissier et al. (2005). In Figure 15, we compare the broad band CLF for the entire galaxy within the D_{25} after the removal of the AGN and SNRs (both with and without the removal of the soft and very soft sources) with the Grimm & Gilfanov canonical luminosity functions, scaled to the mass and star-formation rate of M83. The scaled combination of canonical luminosity functions fails to match the one we have derived from the observations rather badly.

For the CLF including the soft and very soft sources that we propose are dominated by SNRs, a better agreement can be found if the star-formation is only ~ 2 $M_\odot$ yr^{-1} and the stellar mass increased by a factor of 1.5-2.0. However, it is not clear that either of these is allowed; the alternative is that the scaling factors provided by Gilfanov (2004) are simply averages and vary significantly from galaxy to galaxy, depending on the star formation history and perhaps the metallicity. Better agreement would be obtained if one also allows the LMXB function to shift to higher luminosities by factors of two to four; variation in the cut-offs of individual galaxies have been observed previously (Gilfanov 2004). In any event, the X-ray CLF suggests that the current starburst has provided a very thin icing of HMXB over a substantial population of LMXB that has built up over a long period of steady star-formation over the last Gyr.

A recent study of the luminosity functions of star-forming galaxies (Mineo et al. 2012) examined only galaxies with a star-formation rate/stellar mass ratio $> 10^{-10} yr^{-1}$. M83 falls just below this value, suggesting that it is not HMXB dominated. Using the Gilfanov scaling from stellar mass to LMXB rate, Mineo et al. (2012) found an unexpectedly large number of LMXB in their "HMXB-dominated" galaxies. M83 suggests that LMXB scaling may not need to be reduced so much for the galaxies at the low end of the specific star-formation rate, and that the HMXB scaling may need to be reduced as well. Overall, M83 falls below their L_X-SFR relation, but within the observed scatter for that relation.

As we noted at the beginning of this Section, our current examination of the CLF in M83 was intended primarily to provide an initial exploration of the properties of the CLF. That the canonical luminosity functions do not describe the M83 CLF *well* was probably to be expected; more sophisticated models based on calculating the evolution of stellar populations (e.g. StarTrack, Belczynski et al. 2008) show that even simple star formation histories can produce complex CLFs (Luo et al. 2012; Fragos et al. 2008; Tzanavaris et al. 2013). We anticipate applying these more sophisticated models to these data in the near future. However, even before applying them, it is clear that the faint populations in M83 may pose some significant challenges. Further studies, including those we are carrying out with HST (Blair et al. 2013), are needed to identify as many of the soft and very soft sources as possible. Since a small variation in the number of high luminosity sources can make a

significant change in the shape of the CLF, and those source should be dominated by HMXB, optical efforts to identify HMXB hold are likely to shed some light on this mystery.

10. Discussion

We have surveyed point sources in M83 to a depth of about 10^{36} ergs s^{-1} in the 0.35-8 keV band, finding 378 sources within the D_{25} contours of the galaxy. As reported by Soria & Wu (2003), the sources are concentrated in the nuclear region of the galaxy, and in the spiral arms. The association with the spiral arms is mostly due to the sources with soft spectral indices; the harder sources, which tend to be brighter, are more evenly distributed across the face of the galaxy.

In an attempt to understand what fraction of the X-ray emission of the galaxy that has been resolved into point sources by our observations, we have carried out a simple two-component thermal fit to the spectrum obtained from all of the source counts within the D_{25} contours of the galaxy. Based on this we estimate the intrinsic 0.35-8 keV X-ray luminosity of M83 to be $1.85 \pm 0.20 \times 10^{40}$ ergs s^{-1}. Of this, 5.8×10^{39} ergs s^{-1} or 32% arises from the nuclear/bulge region of the galaxy, and 1.27×10^{40} ergs s^{-1} or 68% arises from the disk. About half of the luminosity of the disk, or 6.3×10^{39} ergs s^{-1} arises from sources brighter than 10^{38} ergs s^{-1}. The total intrinsic luminosity of the point sources, calculated by summing up all of the point source fluxes within the D25 contours, and fitting the resulting spectrum, is $1.30 \pm 0.15 \times 10^{40}$ ergs s^{-1}, or 70% of the total.

The remaining 30% of the X-ray emission is most likely dominated by a combination of emission from hot diffuse gas and unresolved point sources. If we exclude regions containing point sources within the D_{25} contours, and construct a spectrum of M83, the spectrum shows a very strong soft X-ray component with obvious emission from a hot plasma. If we carry out a two-component thermal fit, we find that about 6×10^{39} ergs s^{-1} arises from a soft component, clearly associated with emission from hot diffuse gas, and $1 - 2 \times 10^{39}$ ergs s^{-1} arises from a hard component, which we suspect is unresolved point sources.[13] A large portion of the unresolved emission, both in the soft component and the hard component, arises from the nuclear region where only 31% of the luminosity is resolved into point sources.

---

[13] Analyzed in this manner, the sum of the point source luminosity 1.30×10^{40} ergs s^{-1} and the two components to the unresolved emission, 6×10^{39} ergs s^{-1} and $1 - 2 \times 10^{39}$ ergs s^{-1} is 2×10^{40} ergs s^{-1}, which exceeds the total luminosity obtained by simply fitting all the counts within the D25 contours, $1.85 \pm 0.20 \times 10^{40}$ ergs s^{-1} slightly. Small differences of this type are to be expected given the relatively crude way in which these spectra have been extracted from the data and then fit.

The number of SNRs we appear to have found in M83 is remarkable: 87 if we count only sources with supporting information that they are SNRs, and ~ 130 if we assume that half of the unidentified sources with (M–S)/T hardness ratios less than -0.5 are SNRs. There are 378 sources within the D_{25} contour of M83. Of these, we estimate that 97 are AGN and we identify 2 as foreground stars. Thus of the approximately 279 sources that we believe are actually in M83 within the D_{25} contours, we estimate 31% are SNRs, or 47% if we include half the unidentified soft sources as likely SNRs.

Is the large number of SNRs unusual? M33, which is much nearer (817 ± 58 kpc, Freedman et al. 2001), much less massive ($3 - 6 \times 10^9$ $M_\odot$, Corbelli 2003), a lower SF rate (0.45 ± 0.10 $M_\odot yr^-1$, Verley et al. 2009) and similar foreground absorption (6×10^{20} cm^{-2}, Dickey & Lockman 1990), is one obvious point of comparison, since it was the subject of a very deep set of *Chandra* observations totaling 1.4 Msec of observing time (Plucinsky et al. 2008). Two separate analyses of this data set have been carried out. In a targeted search for SNRs, Long et al. (2010) found excess ($>2\sigma$) X-ray emission at the positions of 82 of the 135 optically-identified SNRs in M33. They estimated that there are no undiscovered SNRs in the region covered by the *Chandra* observations brighter than 4×10^{35} ergs s^{-1} in the 0.35-2 keV band. As a result, M33 is the only spiral galaxy with comparable numbers of identified X-ray SNRs to M83. Separately, in an analysis of point sources in M33 with detection criteria very similar to those adopted here, Tüllmann et al. (2011) found 45 SNRs out of a total of 662 sources, to a luminosity limit of 1.2×10^{35} ergs s^{-1} in the 0.5-2 keV band. In the case of M33, AGN constitute a much larger fraction of the sources in the survey than in M83; roughly 80% of the sources are background AGN, (see Figure 10 of Tüllmann et al. 2011), leaving about 130 sources from M33. Therefore in M33, as in M83, roughly one third of the sources are SNRs. Of the 56 sources reported in that study that have an an X-ray luminosity greater than 10^{36} ergs s^{-1}, five were SNRs.[14] Scaling by the SFR, 0.45 ± 0.10 $M_\odot yr^-1$ vs. 3-4 $M_\odot$, one would have expected to find 30-60 SNRs in M83 brighter than 10^{36} ergs s^{-1}, approximately what is found.

At a distance of 2 Mpc (Dalcanton et al. 2009), the Sculptor group spiral NGC300 is similar to M33 in terms of foreground absorption (6×10^{20} cm^{-2}, Dickey & Lockman 1990)and stellar mass (2.4×10^9 $M_\odot$, Puche et al. 1990). Binder et al. (2012) found 95 X-ray sources down to a luminosity limit of 10^{36} ergs s^{-1} in a 60 ksec *Chandra* observation. Of these, they suggest that 11 sources are SNRs based on hardness, of which seven turned out to be within 3.5″ of known optical SNR candidates. They estimate that about 47% of the sources are AGN, in which case about 22% of the sources located in NGC300 are SNRs, so it too has a

---

[14]As calculated by us from using the photon fluxes contained in Tüllmann et al. (2011) and assuming a power law with photon index -1.9.

relatively high SNR fraction.

For M31, the fraction of SNRs appears to be lower. Stiele et al. (2011), using XMM, found 1897 sources along the line of sight to M31 down to a luminosity limit of 10^{35} ergs s^{-1} in the 0.2-4.5 keV band. They detected 25 SNRs and 31 SNR candidates, roughly 3% of the total. The SNRs, along with the bright XRBs, are concentrated in the arms, and thus near regions of active star formation. However, the majority of their sources are, not surprisingly, unidentified. They did find 31 SSSs, 14 transients arising from optical novae, and a number of X-ray binaries, including 36 certain and 16 likely LMXBs in globular clusters. They classify about 260 as foreground objects, and about 90 as background objects (with various degrees of certainty), based on the sources' characteristics and comparisons to other surveys and optical data. They did not attempt a statistical analysis of the number of background sources in the sample, deferring this analysis to a future paper; they do note in passing that they expect about 2/3 of the 1247 hard spectrum objects that are unclassified objects to be background objects. If this is correct, there are a total of 715 sources in their sample located in M31, reflecting the fact that the mass of M31 is much larger than either M33 or NGC300. The SNRs and SNR candidates thus comprise about 8% of the sources, much less than the corresponding fraction in M33 or M83.

The fact that M31 has a lower fraction of SNRs is due to the specific SFR, which is lower in M31 because it is an earlier type galaxy. The SF rate in M31 is estimated to be 0.4 $M_\odot$ yr^{-1} (Barmby et al. 2006); the stellar mass is $10 - 15 \times 10^{10}$ $M_\odot$ (Tamm et al. 2012). This compares to $\sim$3-4 $M_\odot$ yr^{-1} (Boissier et al. 2005) and 4×10^{10} $M_\odot$ in M83 (see, Section 9.4) and to 0.45$\pm$0.1 $M_\odot$ yr^{-1} (Verley et al. 2009) and $3 - 6 \times 10^9$ $M_\odot$(Corbelli 2003) in M33.

The fact that the absolute numbers of SNRs are high in M83, despite its distance of 4.61 Mpc, is almost certainly due to the high star formation rate near $\sim$3-4 $M_\odot$yr^{-1} (Boissier et al. 2005), the depth of our *Chandra* observations, and low galactic absorption along the line of sight. While M83 and M33 have roughly the same number of X-ray detected SNRs, the majority of the SNRs that were detected in M33 would not have been detected at the distance of M83. M33 has not had a single historical SNe, and M31 has only had one; M83 has had six. There may also be some differences in the SNR populations in M33 that are not associated simply with the star formation rate. There is, for example, some indication (see Figure 15 of Blair et al. 2012) that M83 SNRs are systematically brighter in Hα than their M33 counterparts, presumably because they are on average expanding into a denser medium. If this is the case, then one might expect them to be systematically brighter in X-rays as well. However, a detailed discussion of the characteristics of the SNRs in M33 and a comparison to the properties of SNRs in other galaxies is beyond the scope of this

report.

As described in Section 8, there are 82 unidentified sources with (M–S)/T hardness ratios of -0.5 or less, and half of these have ratios <-0.88. Based on their variability, some of these sources, of order 20%, are supersoft sources. Some of these are likely to be WDs undergoing nuclear burning as a result of mass transfer, and others are likely BH transients. Like the SNRs, the supersoft sources are seen due to the fact that N_H is so low along the line of sight to M83. Further work is clearly required. Deeper narrow-band imaging of these sources with *HST* and our follow-up JVLA study of M83 may identify many of the SNRs and, by elimination, the remaining supersoft objects in the sample.

11. Summary

We have presented an overview of the sources identified from a series of new *Chandra* observations of M83 that total 729 ks of observing time distributed over a year, along with a new radio survey of M83 with ATCA. Combined with archival observations from a decade earlier, we have found 378 X-ray sources within the D_{25} contours of the galaxy to a limiting luminosity of about 8×10^{35} ergs s^{-1}, of which 45 are coincident with ATCA sources. About 1/4 of the X-ray sources are seen to be variable in our initial analysis. Despite the sensitivity of the survey, a large majority of the sources are associated with M83, as opposed to background or foreground objects.

The luminosity of the X-ray point sources totals $1.30 \pm 0.15 \times 10^{40}$ ergs s^{-1}. The brightest source in the galaxy is a ULX, discussed in detail by Soria et al. (2012), located in an inter-arm region of the galaxy. The total luminosity of the galaxy is about $1.85 \pm 0.2 \times 10^{40}$ ergs s^{-1}, and so about 70% of the X-ray luminosity has been resolved into point sources. Our main results are as follows:

- Most of the sources in the galaxy are binary X-ray sources. The binary X-ray sources in the disk are not strongly correlated with the spiral arms. The luminosity function of the binary X-ray sources in the disk resembles that expected from LMXBs, despite the fact that M83 has a high star formation rate of between 3 and 4 $M_\odot$ yr^{-1} (Boissier et al. 2005). The CLF outer bulge/nuclear region appears to be dominated by high mass X-ray binaries. The CLF of the inner bulge/nuclear starburst has the shape expected for a low mass binary population, contrary to expectations, but this unexpected result may be attributable to the effects of source crowding and strong diffuse emission in the region.

- There is a substantial number of SNRs in the sample, a higher percentage than has been

found in studies of most (but not all) other galaxies. A total of about 67 (73) sources lie within $1''$ ($2''$) of SNRs identified by Blair et al. (2012) from optical interference filter imagery. The spectra of these sources are soft, and in X-ray hardness-ratio diagrams they occupy a region where SNRs are expected. Counting sources from other optical surveys (Dopita et al. 2010) and objects with soft spectra coincident with ATCA radio sources, we find that 87 X-ray sources are most likely SNRs, fully 24% of the sample within the D_{25} contours of the galaxy, and 31% after AGN have been statistically removed. There are 82 other sources in the same region of the hardness-ratio diagram as SNRs; many of these are likely SNRs as well. The large number of SNRs detected in the survey is most likely due to a combination of factors, including the high sensitivity of the survey to soft sources, the fact that the density in the ISM in M83 is high, making SNRs relatively bright, and the fact that M83 lies along a line of sight with low foreground column. This is also consistent with the high SF and SN rates in M83. Unlike the binary X-ray sources, the SNRs (and indeed the soft sources as a whole) are concentrated in the spiral arms of the galaxy.

This data set represents a resource for understanding the X-ray properties of galaxies with active star formation, which we plan to exploit in conjunction with our on-going efforts to acquire additional data with *HST* and the JVLA. Future reports will address areas such as the global properties of the supernova remnant population in M83, the characteristics of the diffuse emission, and X-ray emission from the nuclear region.

REFERENCES

Arnaud, K. A. 1996, in Astronomical Society of the Pacific Conference Series, Vol. 101, Astronomical Data Analysis Software and Systems V, ed. G. H. Jacoby & J. Barnes, 17

Barmby, P., et al. 2006, ApJ, 650, L45

Barret, D. 2001, Advances in Space Research, 28, 307

Belczynski, K., Kalogera, V., Rasio, F. A., Taam, R. E., Zezas, A., Bulik, T., Maccarone, T. J., & Ivanova, N. 2008, ApJS, 174, 223

Bell, E. F., & de Jong, R. S. 2001, ApJ, 550, 212

Bertelli, G., Bressan, A., Chiosi, C., Fagotto, F., & Nasi, E. 1994, A&AS, 106, 275

Bertelli, G., Nasi, E., Girardi, L., & Marigo, P. 2009, A&A, 508, 355

Binder, B., et al. 2012, ApJ, 758, 15

Blair, W. P., & Long, K. S. 2004, ApJS, 155, 101

Blair, W. P., et al. 2014, ApJ, submitted

Blair, W. P., Winkler, P. F., & Long, K. S. 2012, ApJS, 203, 8

Boissier, S., et al. 2005, ApJ, 619, L83

Broos, P. S., Townsley, L. K., Feigelson, E. D., Getman, K. V., Bauer, F. E., & Garmire, G. P. 2010, ApJ, 714, 1582

Burstein, D., & Heiles, C. 1982, AJ, 87, 1165

Chandra, P., Dwarkadas, V. V., Ray, A., Immler, S., & Pooley, D. 2009, ApJ, 699, 388

Chevalier, R. A. 1982, ApJ, 259, 302

Corbelli, E. 2003, MNRAS, 342, 199

Cowan, J. J., & Branch, D. 1985, ApJ, 293, 400

Cowan, J. J., Roberts, D. A., & Branch, D. 1994, ApJ, 434, 128

Crawford, D. F., Jauncey, D. L., & Murdoch, H. S. 1970, ApJ, 162, 405

Dalcanton, J. J., et al. 2009, ApJS, 183, 67

Dickey, J. M., & Lockman, F. J. 1990, ARA&A, 28, 215

Di Stefano, R., & Kong, A. K. H. 2004, ApJ, 609, 710

Dopita, M. A., et al. 2010, ApJ, 710, 964

Dottori, H., Diaz, R., & Mast, D. 2008, AJ, 136, 2468

Ducci, L., Sasaki, M., Haberl, F., & Pietsch, W. 2013, A&A, 553, A7

Dwarkadas, V. V., & Gruszko, J. 2012, MNRAS, 419, 1515

Eck, C. R., Roberts, D. A., Cowan, J. J., & Branch, D. 1998, ApJ, 508, 664

Fabbiano, G. 2006, ARA&A, 44, 323

Flesch, E. 2010, PASA, 27, 283

Fragos, T., et al. 2008, ApJ, 683, 346

Freedman, W. L., et al. 2001, ApJ, 553, 47

Fridriksson, J. K., Homan, J., Lewin, W. H. G., Kong, A. K. H., & Pooley, D. 2008, ApJS, 177, 465

Fruchter, A. & Sosey, M. et al. 2009, "The MultiDrizzle Handbook", version 3.0, (Baltimore, STScI)

Fruscione, A., et al. 2006, in Society of Photo-Optical Instrumentation Engineers (SPIE) Conference Series, Vol. 6270, Society of Photo-Optical Instrumentation Engineers (SPIE) Conference Series

Gilfanov, M. 2004, MNRAS, 349, 146

Gradari, S., et al. 2011, MNRAS, 412, 2689

Green, D. A. 2009, Bulletin of the Astronomical Society of India, 37, 45

Grimm, H.-J., Gilfanov, M., & Sunyaev, R. 2002, A&A, 391, 923

Grimm, H.-J., Gilfanov, M., & Sunyaev, R. 2003, MNRAS, 339, 793

Hamuy, M., Walker, A. R., Suntzeff, N. B., Gigoux, P., Heathcote, S. R., & Phillips, M. M. 1992, PASP, 104, 533

Harris, J., Calzetti, D., Gallagher, J. S., III, Conselice, C. J., & Smith, D. A. 2001, AJ, 122, 3046

Hirayama, M., Nagase, F., Endo, T., Kawai, N., & Itoh, M. 2002, MNRAS, 333, 603

Houghton, R. C. W., & Thatte, N. 2008, MNRAS, 385, 1110

Hughes, J. P., Chugai, N., Chevalier, R., Lundqvist, P., & Schlegel, E. 2007, ApJ, 670, 1260

Immler, S., et al. 2005, ApJ, 632, 283

Immler, S., Vogler, A., Ehle, M., & Pietsch, W. 1999, A&A, 352, 415

Jarrett, T. H., Chester, T., Cutri, R., Schneider, S. E., & Huchra, J. P. 2003, AJ, 125, 525

Jensen, E. B., Talbot, R. J., Jr., & Dufour, R. J. 1981, ApJ, 243, 716

Jones, D. H., et al. 2009, MNRAS, 399, 683

Kalberla, P. M. W., Burton, W. B., Hartmann, D., Arnal, E. M., Bajaja, E., Morras, R., Pöppel, W. G. L. 2005, A&A, 440, 775

Kilgard, R. E., Kaaret, P., Krauss, M. I., Prestwich, A. H., Raley, M. T., & Zezas, A. 2002, ApJ, 573, 138

Kilgard, R. E., et al. 2005, ApJS, 159, 214

Kim, M., Wilkes, B. J., Kim, D.-W., Green, P. J., Barkhouse, W. A., Lee, M. G., Silverman, J. D., & Tananbaum, H. D. 2007, ApJ, 659, 29

Kim, H., Whitmore, B. C., Chandar, R., et al. 2012, ApJ, 753, 26

Knapen, J. H., Sharp, R. G., Ryder, S. D., Falcón-Barroso, J., Fathi, K., & Gutiérrez, L. 2010, MNRAS, 408, 797

Kong, A. K. H., DiStefano, R., Garcia, M. R., & Greiner, J. 2003, ApJ, 585, 298

Kubota, A., & Makishima, K. 2004, ApJ, 601, 428

Kubota, A., Tanaka, Y., Makishima, K., Ueda, Y., Dotani, T., Inoue, H., & Yamaoka, K. 1998, PASJ, 50, 667

Lin, D., Remillard, R. A., & Homan, J. 2007, ApJ, 667, 1073

Long, K. S., et al. 2010, ApJS, 187, 495

Long, K. S., et al. 2012, ApJ, 756, 18

Lundgren, A. A., Wiklind, T., Olofsson, H., & Rydbeck, G. 2004, A&A, 413, 505

Luo, B., et al. 2012, ApJ, 749, 130

Ma, C., et al. 2009, IERS Technical Note, 35, 1

Maddox, L. A., Cowan, J. J., Kilgard, R. E., Lacey, C. K., Prestwich, A. H., Stockdale, C. J., & Wolfing, E. 2006, AJ, 132, 310

Manchester, R. N., Staveley-Smith, L., & Kesteven, M. J. 1993, ApJ, 411, 756

Mast, D., Diaz, R., & Aguero, M. 2006, AJ, 131, 1394

Mateos, S., et al. 2008, A&A, 492, 51

McMullin, J. P., Waters, B., Schiebel, D., Young, W., & Golap, K. 2007, Astronomical Data Analysis Software and Systems XVI, 376, 127

Milisavljevic, D., Fesen, R., Chevalier, R., Kirshner, R., Challis, P., & Turatto, M. 2012, arXiv:1203.0006

Mineo, S., Gilfanov, M., & Sunyaev, R. 2012, MNRAS, 419, 2095

Mitsuda, K., Inoue, H., Nakamura, N., & Tanaka, Y. 1989, PASJ, 41, 97

Monet, D. G., et al. 2003, AJ, 125, 984

Morse, J. A., Smith, N., Blair, W. P., Kirshner, R. P., Winkler, P. F., & Hughes, J. P. 2006, ApJ, 644, 188

Park, S., Zhekov, S. A., Burrows, D. N., Racusin, J. L., Dewey, D., & McCray, R. 2011, ApJ, 733, L35

Paturel, G., Petit, C., Prugniel, P., Theureau, G., Rousseau, J., Brouty, M., Dubois, P., & Cambrésy, L. 2003, A&A, 412, 45

Patnaude, D. J., Loeb, A., & Jones, C. 2011, New A, 16, 187

Pennington, R. L., Talbot, R. J., Jr., & Dufour, R. J. 1982, AJ, 87, 1538

Piqueras López, J., Davies, R., Colina, L., & Orban de Xivry, G. 2012, ApJ, 752, 47

Plucinsky, P. P., et al. 2008, ApJS, 174, 366

Puche, D., Carignan, C., & Bosma, A. 1990, AJ, 100, 1468

Primini, F. A., Forman, W., & Jones, C. 1993, ApJ, 410, 615

Remillard, R. A., & McClintock, J. E. 2006, ARA&A, 44, 49

Reynolds, S. P., Borkowski, K. J., Green, D. A., Hwang, U., Harrus, I., & Petre, R. 2009, ApJ, 695, L149

Roeser, S., Demleitner, M., & Schilbach, E. 2010, AJ, 139, 2440

Saha, A., Thim, F., Tammann, G. A., Reindl, B., & Sandage, A. 2006, ApJS, 165, 108

Sault, R. J., Teuben, P. J., & Wright, M. C. H. 1995, Astronomical Data Analysis Software and Systems IV, 77, 433

Schlegel, D. J., Finkbeiner, D. P., & Davis, M. 1998, ApJ, 500, 525

Soria, R., Kuntz, K. D., Winkler, P. F., Blair, W. P., Long, K. S., Plucinsky, P. P., & Whitmore, B. C. 2012, ApJ, 750, 152

Soria, R., Long, K. S., Blair, W. P., et al., Science, in press

Soria, R., & Perna, R. 2008, ApJ, 683, 767

Soria, R., & Wu, K. 2002, A&A, 384, 99

Soria, R., & Wu, K. 2003, A&A, 410, 53

Stiele, H., Pietsch, W., Haberl, F., Hatzidimitriou, D., Barnard, R., Williams, B. F., Kong, A. K. H., & Kolb, U. 2011, A&A, 534, A55

Sutherland, R. S., & Dopita, M. A. 1995, ApJ, 439, 381

Stockdale, C. J., Maddox, L. A., Cowan, J. J., Prestwich, A., Kilgard, R., & Immler, S. 2006, AJ, 131, 889

Stockdale, C. J., Williams, C. L., Weiler, K. W., Panagia, N., Sramek, R. A., Van Dyk, S. D., & Kelley, M. T. 2007, ApJ, 671, 689

Takeuchi, T. T., & Ishii, T. T. 2004, ApJ, 604, 40

Talbot, R. J., Jr., Jensen, E. B., & Dufour, R. J. 1979, ApJ, 229, 91

Tamm, A., Tempel, E., Tenjes, P., Tihhonova, O., & Tuvikene, T. 2012, A&A, 546, A4

Tennant, A. F., Wu, K., Ghosh, K. K., Kolodziejczak, J. J., & Swartz, D. A. 2001, ApJ, 549, L43

Thatte, N., Tecza, M., & Genzel, R. 2000, A&A, 364, 47

Tüllmann, R., et al. 2011, ApJS, 193, 31

Trinchieri, G., Fabbiano, G., & Palumbo, G. G. C. 1985, ApJ, 290, 96

Turatto, M., Cappellaro, E., & Danziger, I. J. 1989, The Messenger, 56, 36

Tzanavaris, P., Fragos, T., Tremmel, M., Jenkins, L., Zezas , A., Lehmer, B. D., Horn-schemeier, A., Kalogera, V., Ptak, A., & Basu-Zych, A. R. 2013, ApJ, 774, 136

Verley, S., Corbelli, E., Giovanardi, C., & Hunt, L. K. 2009, A&A, 493, 453

Weiler, K. W., Panagia, N., Montes, M. J., & Sramek, R. A. 2002, ARA&A, 40, 387

Weiler, K. W., Williams, C. L., Panagia, N., Stockdale, C. J., Kelley, M. T., Sramek, R. A., Van Dyk, S. D., & Marcaide, J. M. 2007, ApJ, 671, 1959

Weisskopf, M. C., Guainazzi, M., Jahoda, K., Shaposhnikov, N., O'Dell, S. L., Zavlin, V. E., Wilson-Hodge, C., & Elsner, R. F. 2010, ApJ, 713, 912

White, N. E., Stella, L., & Parmar, A. N. 1988, ApJ, 324, 363

Williams, B. J., et al. 2008, ApJ, 687, 1054

Wilms, J., Allen, A., & McCray, R. 2000, ApJ, 542, 914

Wofford, A., Leitherer, C., & Chandar, R. 2011, ApJ, 727, 100

Wood, R. & Andrews, P. J. 1974, MNRAS, 167, 13

Wu, K. 2001, PASA, 18, 443

Zacharias, N., Monet, D. G., Levine, S. E., Urban, S. E., Gaume, R., & Wycoff, G. L. 2004, Bulletin of the American Astronomical Society, 36, 1418

A. Specific Comments on the 29 Brightest X-ray Sources

As discussed in the Section 6, there are 29 X-ray sources with more that 2000 counts that allow a more detailed treatment of there X-ray spectral fitting. Below we present these sources in increasing RA order, and provide a brief description of their position in the galaxy, any possible optical counterparts, and comments about the spectral results and what they say about the possible identification of the source type. The source luminosities quoted below are derived from our individual XSPEC spectral fits, and differ from those in Table 4 which assume a simple power-law model with fixed photon index and column density:

- Source X029 (=S03-005) is a persistent X-ray source, with little evidence of time variability. It is located along the line of sight to a small star-forming clump or OB association. It has a hard, featureless X-ray spectrum that can be fit (phenomenologically) with a power law with photon index $\Gamma = 1.58 \pm 0.08$ and 0.35–8 keV luminosity $2 - 3 \times 10^{38}$ ergs s^{-1}. We explained in Section 6 that the hard power-law spectrum cannot be physically interpreted as a canonical low/hard state, and is more likely the result of two optically-thick thermal (or thermal-Comptonization) components often found in the spectra of NS XRB at high luminosities. In this case, an equally good fit is obtained with a disk-blackbody with $T_{in} = 1.81^{+0.14}_{-0.10}$ keV and $r_{in} (\cos \theta)^{0.5} \approx 10$ km. Thus, we interpret this source as a NS XRB near its Eddington limit.

- Source X038 is a persistent source that is coincident with an AGN (z=0.078) in the 6dF galaxy survey Jones et al. (2009). The source varies by a factor of about four on timescales of months. Consistent with this identification, the spectrum is well fit with a power law spectrum with a photon index $\Gamma = 2.4 \pm 0.1$. The luminosity of the source is about 2.1×10^{42} ergs s^{-1} at this redshift.

- Source X138 (=S03-027) is a hard X-ray source, whose spectrum is well modeled in terms of a simple power law with $\Gamma = 1.24 \pm 0.10$ (unusually hard for an XRB). It is located well away from the star forming regions of M83 near the southern edge of the bright optical disk, and there is no evidence of emission from a background AGN in the optical images. The source varied by $\pm 30\%$ in late 2010 and 2011, but was considerably brighter in one of the archival observations. We also tried a disk-blackbody plus simple blackbody model, and a Comptonized disk model (`diskir`) but they give slightly worse fits than a simple power-law. If the source is in M83, it has an average 0.35–8 keV luminosity of 1.1×10^{38} ergs s^{-1}, too high for a BH system in the low hard state. Thus, it is possible that this source is a NS XRB in the high state, but its true nature remains unclear; the difficulty in obtaining a good fit to the average spectrum may be due to spectral variability between observations.

- Source X145 (=S03-031) is a persistent X-ray source with a 0.35–8 keV luminosity of about 1.5×10^{38} ergs s^{-1}, located north of the nucleus within one of the outer spiral arms. The source varies by $\pm 20\%$ between observations. There are no stellar clusters at the position of the source. As we discussed for several other sources, it is well fit by a hard power-law model ($\Gamma = 1.53 \pm 0.07$) which we regard as purely phenomenological. A disk-blackbody plus simple blackbody model provides a more physical interpretation, but has too many free parameters to constrain the fit. A disk-blackbody model provides an acceptable fit (statistically equivalent to the simple power-law model) with $T_{in} = 1.80^{+0.13}_{-0.11}$ keV and $r_{in} (\cos \theta)^{0.5} \approx 8$ km, as expected from a near-Eddington NS XRB.

- Source X152 (=S03-033) is a persistent source, varying by $\pm 20\%$ between observations; it is located in the southern spiral arm, but there is no obvious optical counterpart. As for several other cases already discussed, a power-law model gives a hard slope $\Gamma = 1.45 \pm 0.07$, but a more physical interpretation is to be found in a disk-blackbody plus blackbody model. The disk parameters are $T_{\rm in} = 1.97^{+0.27}_{-0.15}$ keV and $r_{\rm in} (\cos \theta)^{0.5} \approx 7$ km, and the unabsorbed 0.35–8 keV luminosity is 1.5×10^{38} ergs s^{-1}. Once again, we conclude this system is probably a NS XRB, with surface and disk emission, radiating near the Eddington limit.

- Source X168 was not detected in either 2000 or 2001, but appears as a bright X-ray source in observations in late 2010; it then faded gradually by at least a factor of 10 when observed in 2011 September, before brightening again in 2011 December. Its average 0.35–8 keV luminosity is 8×10^{37} ergs s^{-1}.The source is located in the inner portion of one of the spiral arms just south of the nucleus, but has no obvious specific optical counterpart in the Magellan images. The time-averaged spectrum is best modeled in terms of a standard disk-blackbody with $T_{\rm in} = 1.01 \pm 0.05$ keV and $r_{\rm in} (\cos \theta)^{0.5} \approx 20$ km. This suggests that it is more likely a BH transient reaching the high/soft state in some of the observations, but a NS XRB cannot be completely ruled out.

- Source X185 (=S03-44), one of the brightest in M83, is a persistent source located in one of the spiral arms due north of the nucleus, without an obvious optical counterpart. The flux from the source rose by about 10% gradually throughout 2011. The spectrum appears slightly curved, and is inconsistent with either a simple disk-blackbody or a simple power-law model. It is well fitted either by a broken power-law or by a disk-blackbody plus power-law model. The disk parameters ($T_{\rm in} = 2.2 \pm 0.1$ keV, $r_{\rm in} (\cos \theta)^{0.5} \approx 10$ km) suggest a NS and are inconsistent with those expected for a BH XRB. On the other hand, the 0.35–8 keV luminosity is $5 - 7 \times 10^{38}$ ergs s^{-1}, depending upon the model used, which is extremely high for a NS. We suggest that the system is more likely to be a NS XRB radiating at 2 or 3 times its Eddington luminosity, but further studies are merited.

- Source X193 (=S03-047) is a bright, modestly variable source just SW from the brightest portion of the nuclear region. The spectrum is moderately curved and cannot be fit by a simple power-law. Several more complicated models (broken power-law, or disk-blackbody plus power-law, or a variety of comptonized disk models) produce satisfactory fits, and yield consistent 0.3–8 keV luminosities of about 1.3×10^{38} ergs s^{-1}. In the disk-blackbody plus power-law model, the best-fit parameters are $\Gamma = 1.9^{+0.8}_{-0.5}$, $T_{\rm in} = 1.7 \pm 0.3$ keV and $r_{\rm in} (\cos \theta)^{0.5} \approx 7$ km, consistent with a NS XRB in the high

state.

- Source X198 (=S03-049) is one of a grouping of sources NW of the optical/IR nucleus and generally projected onto a region of high optical extinction. By our conservative definition of variability, the source appears to have been constant throughout the year. It can be fitted with a simple power-law model with $\Gamma = 1.54 \pm 0.09$ and total $N_{\rm H} = 1.5 \pm 0.3 \times 10^{21}$ cm^{-2}; however, there is a hint of curvature in the spectrum at about 3 keV. A disk-blackbody model provides a better fit, with only line-of-sight absorption, $T_{\rm in} = 1.75^{+0.08}_{-0.16}$ keV and $r_{\rm in}(\cos\theta)^{0.5} \approx 7$ km. In this model, the unabsorbed 0.3–8 keV luminosity of 9×10^{37} ergs s^{-1}. Once again, the luminosity and spectral properties point to a bright NS XRB.

- Source X216 (=S03-056) is a bright nuclear source with a thermal spectrum, showing prominent emission lines from Mg XI at 1.3 keV, Si XIII at 1.8 keV and S XV at 2.4 keV. The source flux appears constant with time, as one would expect from spatially extended hot plasma. A two-temperature thermal plasma model with $T_1 \approx 0.26$ keV and $T_1 \approx 0.72$ keV provides a good fit but only if the lower-temperature component sees a much lower absorption (line-of-sight only) than the one seen by the higher-temperature plasma ($N_{\rm H} \approx 5 \times 10^{21}$ cm^{-2}). The unabsorbed X-ray luminosity is about 1.3×10^{38} ergs s^{-1}. The source is consistent with the position of SN1968L, as reconstructed by Dopita et al. (2010), and if it is the remnant of SN1968L would be one of the brightest X-ray SNRs known. However, the connection of the SN to the X-ray source is far from conclusive. It is located in a region of extremely active star formation, directly adjacent to one of the brightest young star clusters. Two other SNRs listed in Dopita et al. (2010) lie close by (nuclear SNRs #5 to the NW and #6 to the SSW). In addition, there are several other nearby sources with very similar thermal-plasma spectra, and the general bright diffuse emission from hot gas in the nuclear region could significantly contaminate the spectrum of X216.

- Source X220 (=S03-057) is within the bright optical nucleus directly W of the optical/IR nucleus, with a thermal spectrum, showing Si XIII at 1.8 kev and S XV at 2.4 keV, very similar to X216. The spectrum requires both a multi-temperature thermal-plasma ($T \sim 0.4$–0.7 keV) and a steep power-law ($\Gamma = 3.1 \pm 0.3$) component, with intrinsic absorption of order 1×10^{21} cm^{-2}. The 0.35–8 keV luminosity is about 1×10^{38} ergs s^{-1}. No known SNR candidates align with this source. There is some evidence that the source was brighter in the archival observations, which suggests that we are seeing a combination of (one or more) unresolved XRBs in a compact knot of thermal-plasma emission.

- Source X223 is a nuclear source in close proximity to X216 and X220, and has a very

similar thermal spectrum, although it is somewhat less luminous, 5×10^{37} ergs s^{-1}. It is probably the same as S03-059. Dopita et al. (2010)'s nuclear SNR #8 is essentially coincident, and #10 is just to the ESE, but given the similar discussion of some of the other sources in the nucleus, the alignment with the SNR could be by chance. This source could again be a bright peak in thermal emission in the region rather than a single physical object. The source is not variable.

- Source X227 (=S03-60) is another hard, luminous source, that when fitted with a power law yields a photon index $\Gamma = 1.46 \pm 0.05$ but is too luminous for the canonical BH low/hard state. Once again, we favour a physical model based on simple blackbody plus disk-blackbody; the disk parameters are $T_{in} = 2.0^{+0.3}_{-0.1}$ keV and $r_{in} (\cos \theta)^{0.5} \approx 7$ km, and the intrinsic 0.35–8 keV luminosity is 2×10^{38} ergs s^{-1}. In two of the observations (one from 2011 and one from 2001), X227 was considerably fainter than in all the other epochs. The source is located in a southern spiral arm of M83, but is not associated with any particular star cluster or optical source. Two optical SNRs, B12-133 and B12-136 from the Magellan list (Blair et al. 2012) are within a few arcsec to the south, but X227 is most likely a luminous NS XRB.

- Source X228 (=S03-062) is a bright, variable, and relatively hard source on the southern edge of the bright optical nuclear region. It is adequately fit in terms of a simple power-law with $\Gamma = 1.67 \pm 0.10$, but also (more physically) by a disk-blackbody with $T_{in} = 1.47 \pm 0.10$ keV, $r_{in} (\cos \theta)^{0.5} \approx 8$ km, and intrinsic luminosity 7.4×10^{37} ergs s^{-1}. Statistically, the best fit is provided by a broken-power-law model, with a break at $E = 4.1 \pm 1.2$ keV, or by a bremsstrahlung model with $T_e = 8 \pm 2$ keV. Dopita et al. (2010)'s nuclear SNR #13 is very close to X228 and could contribute to its X-ray emission (for example via a pulsar wind nebula). This confusion leaves the true nature of the object uncertain, although a NS identification seems plausible.

- Source X229 technically misses out on our "bright source" classification, because it has only ≈ 1900 counts. However, this is due to its relatively high intrinsic absorption (total $N_H \approx 2.4 \times 10^{21}$ cm^{-2}). It has a soft thermal-plasma spectrum, with a temperature range ~ 0.1–0.6 keV and an intrinsic luminosity of about 1.1×10^{38} ergs s^{-1}. SNR #12 in Dopita et al. (2010) is quite close to X229, in the crowded nuclear region.

- Source X231 is a non-variable, soft source in the nuclear region, located just WSW of the optical/IR nucleus. It has a highly absorbed thermal-plasma spectrum, with obvious lines from Mg XI and Si XIII at 1.3 and 1.8 keV respectively. We fit the spectrum with a two-temperature thermal-plasma model ($T_1 = 0.26 \pm 0.03$ keV, $T_2 = 0.75 \pm 0.06$ keV), with intrinsic absorption of $3.5 \pm 0.6 \times 10^{21}$ cm^{-2}. The unabsorbed luminosity is $\sim 7.1 \times 10^{37}$ ergs s^{-1}. The spectral properties of X231 are consistent with

an SNR, and it might be identified with nuclear SNR #11 in Dopita et al. (2010); if this identification is correct, this would be one of the most luminous X-ray SNRs known. We cannot identify a compact radio source at this position, but this may simply be because an individual radio SNR would be swamped by the strong, extended radio emission (both synchrotron and free-free) from the starburst nuclear region.

- Source X233 (=S03-063) corresponds to the optical/IR galactic nucleus(red circle in the panels of Figure 9) and is also a radio source. The nucleus is the site of a massive 10^8 year-old star cluster, whose dynamical mass is estimated to be about $1.3 \times 10^7 \ M_\odot$ (Thatte et al. 2000). X233 varied by 15% in 2010 and 2011, but was somewhat brighter in the 2000 and 2001 observations. Its X-ray spectrum is well fitted with a simple absorbed power-law, with $N(H)_{Gal}$ fixed at $4 \times 10^{20} \ \mathrm{cm}^{-2}$, intrinsic N_H of $1.9 \pm 0.3 \times 10^{21} \ \mathrm{cm}^{-2}$, photon index $\Gamma = 1.45 \pm 0.05$ and average 0.35–8 keV luminosity of $3.2 \pm 0.2 \times 10^{38} \ \mathrm{ergs \, s}^{-1}$. These parameters are at least consistent with a supermassive BH at a luminosity $\sim 10^{-7} L_{\mathrm{Edd}}$, although we cannot rule out a luminous stellar-mass XRB at the same location as the nuclear star cluster.

- Source X234 (=S03-064) is located directly S of the optical/IR nucleus, at the SE end of the star forming bar in the nucleus. It aligns with a bright blue patch of optical emission, indicating intense star formation in the region. However, its X-ray properties show that it is not an SNR. The source varied in flux by a factor of about 5 during 2010–2011. Its average spectrum has a photon index $\Gamma = 2.65 \pm 0.07$ when fit with a simple power-law; this is typical of a BH in the steep-power-law state (Remillard & McClintock 2006). However, the source can also be fit with a power-law plus disk-blackbody model, consistent with other states of luminous XRBs. In the latter model, $\Gamma = 2.9 \pm 0.2$, $T_{\mathrm{in}} = 1.2 \pm 0.3$ keV, $r_{\mathrm{in}} \left(\cos \theta \right)^{0.5} \approx 9$ km, and the intrinsic 0.35–8 keV luminosity is $3.3 \times 10^{38} \ \mathrm{ergs \, s}^{-1}$. We cannot rule out a BH XRB, but we consider a NS XRB more likely, based on the small inner-disk radius.

- Source X236 (=S03-065) is located in a dense stellar field due south of the nucleus, near several young star clusters and an SNR. It was brightest in December 2010, and faded as 2011 progressed. As for many other sources discussed in this Appendix, a simple power-law model gives a hard photon index $\Gamma = 1.49 \pm 0.10$, but a disk-blackbody plus blackbody model (or more complex two component models with Comptonized thermal emission) provides a more physical interpretation, consistent with a NS XRB. The disk parameters are $T_{\mathrm{in}} = 1.7^{+0.3}_{-0.2}$ keV and $r_{\mathrm{in}} \left(\cos \theta \right)^{0.5} \approx 6$ km; the intrinsic 0.35–8 keV luminosity is $7 \times 10^{37} \ \mathrm{ergs \, s}^{-1}$.

- Source X248 (=S03-72) is a bright source that varies by about a factor of two over the *Chandra* observations. It is located in a dense stellar field in the southern spiral

arm, near a dust lane, but with no obvious optical counterpart. The spectrum is fairly soft, and is well-modeled by a disk-blackbody, with $T_{in} = 0.85 \pm 0.02$ keV and $r_{in} (\cos \theta)^{0.5} \approx 52$ km. With an X-ray luminosity of 3.5×10^{38} ergs s^{-1}, this is almost certainly a BH system in the canonical high/soft state.

- Source X251 (=S03-73) is a highly variable source located in the inner bar of M83, northeast of the nuclear region. The source flux sometimes changes by more than an order of magnitude on time-scales of less than an hour. A faint blue clump of optical emission on the edge of a dust lane appears to align with the X-ray source, and a cluster of young stars is directly adjacent to the NW. The spectrum is slightly curved, and is not well fitted by either a simple power-law or a simple disk-blackbody model. It is, instead, well fitted by a broken power-law (breaking at $E = 3.3^{+0.5}_{-0.4}$ keV) or by a blackbody plus disk-blackbody model; in the latter case, the disk parameters are $T_{in} = 1.40^{+0.07}_{-0.10}$ keV and $r_{in} (\cos \theta)^{0.5} \approx 13$ km; the intrinsic 0.35–8 keV luminosity is 1.8×10^{38} ergs s^{-1}, all consistent with a near-Eddington NS XRB. Occultation by a disk rim or rapid outflows may accounting for the intra-observational variability. This is another source that merits more detailed studies.

- Source X252 (=S03-075) is located at the outer edge of the stellar disk almost due north of the nucleus, and has a spectrum that is well fitted by a power-law with photon index $\Gamma = 1.73 \pm 0.10$, high intrinsic absorption $N_H = 3.8 \pm 0.5 \times 10^{21}$ cm^{-2} and intrinsic 0.35–8 keV luminosity 1.6×10^{38} ergs s^{-1}. Two-component optically-thick thermal or thermal Comptonization models provide similarly good fits, with a variety of parameters often not well constrained (several local minima in the Cash statistics) and inconsistent from model to model. A Comptonized disk model (`diskir`) works for a ranget of disk temperatures $T_{in} \sim 0.2$–0.8 keV and $r_{in} (\cos \theta)^{0.5} \sim 25$–225 km. The main reason why it is hard to constrain the spectral model and parameters is that most of the emission below 1 keV is wiped out by the high absorbing column density. The identification is therefore very uncertain.

- Source X258 (=S03-078) is located in a southern interarm region, but with a very young stellar population $\sim 12''$ to the S and SE. Modestly variable ($\pm 30\%$), its spectrum is not well fitted either in terms of a simple power-law or a disk-blackbody. Disk-blackbody plus simple blackbody fits approximate the shape of the spectrum better, and yield an X-ray luminosity of 1.7×10^{38} ergs s^{-1}, but the implied radius of the NS, ≈ 18 km, and location of the inner edge of the disk, $r_{in} (\cos \theta)^{0.5} \approx 170$ km, are both larger than expected. If it is a NS XRB, it may have an extended photosphere and a truncated inner disk. We conclude that we have not yet found a satisfying spectral model for this source.

- Source X281 (=S03-085) is a persistent, somewhat variable, source with a hard X-ray spectrum (power-law phton index $\Gamma = 1.38 \pm 0.07$) but an intrinsic X-ray luminosity (1.2×10^{38} ergs s^{-1}), too high for the canonical BH low/hard state. It is located in an inner spiral arm NE of the nucleus in a general region of very active star formation but with no specific optical counterpart. A cluster of optical SNRs, including the remnant of SN1957D, are adjacent within 10–20$''$ to the S and SE. Double-component thermal/thermal Comptonization models (*e.g.*, disk-blackbody plus blackbody) approximate the spectrum fairly well, although the implied NS radius of ≈ 20 km is a bit larger than expected. Nevertheless, the object is almost certainly a NS system.

- Source X284 (=S03-086) is a persistent source with a relatively soft X-ray spectrum located in the outer region of of the spiral arm SE of the nucleus. It was considerably (50%) brighter in 2000 and 2001 and 2012 December, than in the other observations. The spectrum of the source is well-fitted in terms of a pure disk-blackbody spectrum with a 0.35–8 keV luminosity of 3×10^{38} ergs s^{-1}. The best-fit parameters are $T_{\rm in} = 0.80 \pm 0.02$ keV and $r_{\rm in} (\cos\theta)^{0.5} \approx 56$ km, consistent with a BH XRB in the high/soft state. Interestingly, the object lies on the edge of a young stellar association, surrounded by a large (≈ 150 pc in radius) ionized bubble or ring-like feature, as seen in our Magellan Hα and [O III] images. Two optical SNRs are also directly adjacent (within a few arcsec), B12-154 and B12-158 from the Magellan SNR list (Blair et al. 2012).

- Source X286 (=S03-088) is another source with a soft X-ray spectrum that is well-modeled with an absorbed disk-blackbody, with an average luminosity 4.6×10^{38} ergs s^{-1}. It varied by $\pm 15\%$ in 2010 and 2011, but appears to have been brighter in 2001. The best-fit parameters are $T_{\rm in} = 0.96 \pm 0.02$ keV and $r_{\rm in} (\cos\theta)^{0.5} \approx 47$ km: almost certainly another BH XRB in the high/soft state. It is located in bright interarm region $\sim 1'$NE of the nucleus, and is less than $1'$ north of the ULX source X299.

- Source X299 is the ULX that appeared in our new observations of M83, which have discussed previously in detail (Soria et al. 2012). It is located in an interarm region $1'$ ESE of the nucleus, and its spectrum is consistent with that expected from binary system containing a black hole with mass between 10 and 40 $M_{\odot}$ and a low-mass companion. We identified a V$\simeq$24 blue stellar counterpart to this source that was not present prior to the turn-on of the source, indicating X-ray reprocessing is probably the likely source of the blue light. A recent XMM-Newton observation from 2013 August (about 3 years after the likely start of the outburst) indicates that the source is still active, with an intrinsic X-ray luminosity $\approx 2 \times 10^{39}$ erg s^{-1}, a factor of 2 lower than the average luminosity in the 2010–2011 *Chandra* observations.

- Source X321 (=S03-104) is located in the inner spiral arm, NE of the nucleus, directly adjacent to a region of massive star formation and Hα emission. The X-ray position is less than $0\rlap{.}''5$ from the SNR B12-179, but the X-ray properties of X321 are not compatible with an SNR interpretation. The source flux varies by a factor of four over the *Chandra* observations. The average spectrum is featureless and is well fitted by a disk-blackbody model, with $T_{\rm in} = 1.40 \pm 0.05$ keV, $r_{\rm in} (\cos\theta)^{0.5} \approx 27$ km and intrinsic 0.35–8 keV luminosity of 6.5×10^{38} ergs s^{-1}. Such parameters are consistent with a stellar-mass BH near its Eddington limit; Galactic BH transients with similarly high disk temperatures and relative low apparent radii are sometimes said to be in the "apparently standard regime" (Kubota & Makishima 2004). The source is quite absorbed, with an intrinsic $N_{\rm H} = 8.7 \pm 0.4 \times 10^{21}$ cm^{-2}.

- Source X386 (=S03-121) is located on the fringes of the stellar disk, NE of the nucleus and beyond the bright spiral arms; no specific optical counterpart is present. It is a hard X-ray source, with a power-law photon index $\Gamma = 1.42 \pm 0.06$. As in many other cases, we can more physically model the spectrum with a disk-blackbody plus blackbody component ($T_{\rm in} = 1.93^{+0.17}_{-0.08}$ keV, $r_{\rm in} (\cos\theta)^{0.5} \approx 8$ km), but broken power-law or Comptonized disk models are also acceptable. Its average 0.35–8 keV luminosity of 2.2×10^{38} ergs s^{-1} is still consistent with a near-Eddington NS XRB. The source flux decreased through the first half of 2011, brightening by a factor 2 in the second semester.

- Source X403 is a very bright, variable X-ray source at the edge of the stellar disk. Its spectrum is well modeled by a disk-blackbody with $T_{\rm in} = 1.10 \pm 0.17$ keV, $r_{\rm in} (\cos\theta)^{0.5} \approx 32$ km, plus a steep power-law with $\Gamma = 2.5^{+0.4}_{-0.3}$. Its intrinsic luminosity is 1.2×10^{39} ergs s^{-1}. These values are typical of a stellar-mass BH at the top of its high/soft state or apparently standard regime, near the Eddington limit. This source was originally classified as a ULX with *ROSAT* (Immler et al. 1999), when it was associated with a very bright optical source, suggested to be a compact HII region or a globular cluster. In the latter scenario, this would have been the first ULX associated with a globular cluster. However, by comparing our *Chandra* and Magellan images, we find that X403 is about $3''$ from the optical source. Moreover, the optical source appears to be a background galaxy rather than a globular cluster, with a faint Hα extension toward the X-ray source position. We conclude that X403 is probably a BH XRB in M83, with a low-mass donor star. This object was not discussed by Soria & Wu (2003) because they only analyzed data from the S3 chip, which did not cover this region.

Table 1.   ACIS-S Observations of M83

Obs. ID	Date	Exposure (s)
793[a]	2000-04-29	50981
2064[a]	2001-09-04	9842
12995	2010-12-23	59291
13202	2010-12-25	98780
12993	2011-03-15	49398
13241	2011-03-18	78963
12994	2011-03-23	150058
12996	2011-03-29	53044
13248	2011-04-03	54329
14332	2011-08-29	52381
12992	2011-09-05	66286
14342	2011-12-28	67103

[a]Archival observation of M83

Table 2.   ATCA Radio Sources

Object	RA (J2000)	Dec. (J2000)	$S_{5\ GHz}$ (mJy)	$S_{9\ GHz}$ (mJy)	Notes[a]
A001	13:36:40.38	-29:51:21.7	0.12±0.03		
A002	13:36:40.91	-29:51:17.9	0.07±0.03		X019; B12-003;
A003	13:36:40.99	-29:51:57.5	0.03±0.02		X020:;
A004	13:36:41.63	-29:52:16.8	0.06±0.02		B12-004:;
A005	13:36:42.22	-29:52:31.5	0.05±0.03		
A006	13:36:43.40	-29:52:23.8	0.16±0.03		
A007	13:36:44.16	-29:50:35.0	0.09±0.03		
A008	13:36:45.24	-29:52:45.3	0.10±0.03		
A009	13:36:49.01	-29:51:14.5	0.05±0.02		
A010	13:36:49.03	-29:49:27.6	0.05±0.02		
A011	13:36:50.06	-29:52:44.1	0.21±0.02	0.19±0.03	M06-01;
A012	13:36:50.87	-29:52:39.7	0.16±0.02	0.05±0.03	X063; M06-03; B12-045;
A013	13:36:50.98	-29:52:25.8	0.09±0.02	0.05±0.03	X065; B12-048;
A014	13:36:51.01	-29:52:36.8	0.08±0.02	0.05±0.03	
A015	13:36:51.19	-29:50:42.0	0.26±0.03	0.15±0.04	X067; M06-04; X-ray hardness suggests SNR;
A016	13:36:51.52	-29:53:00.6	0.18±0.02	0.12±0.03	M06-06;
A017	13:36:51.73	-29:54:09.2	0.08±0.03	0.08±0.03	
A018	13:36:51.79	-29:53:01.6	0.07±0.02	0.02±0.03	X078; X-ray hardness suggests SNR;
A019	13:36:52.57	-29:51:40.0	0.14±0.02	0.15±0.03	
A020	13:36:52.81	-29:52:31.6	0.08±0.02	0.06±0.03	X097; M06-07; X-ray hardness suggests SNR;
A021	13:36:52.82	-29:51:10.3	0.28±0.03	0.18±0.03	X095; M06-08;
A022	13:36:52.86	-29:51:37.5	0.15±0.02	0.06±0.03	X098; M06-09; Absorbed, thermal source in X-ray;
A023	13:36:52.91	-29:52:49.7	0.14±0.02	0.14±0.03	M06-10;
A024	13:36:52.92	-29:51:57.5	0.34±0.02	0.20±0.03	M06-11; SN1950B;
A025	13:36:53.13	-29:53:06.4	0.07±0.02	0.06±0.03	
A026	13:36:53.19	-29:51:33.6	0.72±0.02	0.56±0.03	X104; M06-12; X-ray hardness suggests SNR;
A027	13:36:53.28	-29:52:57.5	0.24±0.02	0.14±0.03	M06-13;
A028	13:36:53.30	-29:50:59.0	0.28±0.02	0.20±0.03	M06-14;
A029	13:36:53.34	-29:51:29.8	0.13±0.02	0.10±0.03	
A030	13:36:53.43	-29:51:11.7	0.11±0.03	0.09±0.03	M06-15;
A031	13:36:53.80	-29:48:49.8	0.12±0.02		X116:; B12-073:; X-ray source and SNR closer to A032;
A032	13:36:53.89	-29:48:48.2	0.12±0.02		X116; B12-073;
A033	13:36:54.14	-29:50:43.0	0.13±0.02	0.08±0.03	M06-16:;
A034	13:36:54.42	-29:53:05.0	0.29±0.02	0.24±0.03	M06-17;

Table 2—Continued

Object	RA (J2000)	Dec. (J2000)	$S_{5\ GHz}$ (mJy)	$S_{9\ GHz}$ (mJy)	Notes[a]
A035	13:36:54.74	-29:52:57.1	0.16±0.02	0.12±0.02	M06-18;
A036	13:36:54.95	-29:53:10.5	0.20±0.02	0.17±0.02	X133:; M06-19;
A037	13:36:55.02	-29:52:39.3	0.07±0.02	0.02±0.02	X129; M06-20:; B12-087;
A038	13:36:55.14	-29:53:09.6	0.12±0.02	0.08±0.02	X133:;
A039	13:36:55.46	-29:53:03.0	0.11±0.02	0.10±0.02	X139:; M06-22:; B12-096;
A040	13:36:55.49	-29:50:44.2	0.06±0.02	0.01±0.02	
A041	13:36:55.77	-29:49:52.4	0.38±0.03	0.27±0.04	M06-23;
A042	13:36:55.85	-29:50:45.2	0.07±0.02	0.10±0.02	
A043	13:36:56.23	-29:52:55.2	0.10±0.02	0.08±0.02	X141; M06-24; B12-106;
A044	13:36:56.39	-29:48:17.8	0.16±0.02		X143;
A045	13:36:56.49	-29:53:08.9	0.09±0.02	0.09±0.03	
A046	13:36:56.88	-29:52:48.7	0.08±0.02	0.07±0.03	M06-26;
A047	13:36:56.96	-29:50:43.2	1.02±0.07	0.42±0.04	M06-27; FRII galaxy (N lobe);
A048	13:36:57.21	-29:54:49.4	0.03±0.02		
A049	13:36:57.39	-29:52:47.6	0.09±0.02	0.06±0.03	
A050	13:36:58.38	-29:51:04.7	0.77±0.02	0.74±0.02	X165; M06-28; FRII galaxy (core); Background AGN;
A051	13:36:58.64	-29:52:36.5	0.11±0.02		X169; X-ray hardness suggests SNR;
A052	13:36:58.76	-29:48:05.7	0.06±0.02		
A053	13:36:59.06	-29:52:31.7	0.16±0.02	0.05±0.02	
A054	13:36:59.08	-29:51:16.3	0.35±0.03		M06-29; FRII galaxy (S lobe);
A055	13:36:59.15	-29:54:28.3	0.04±0.02		X179;
A056	13:36:59.36	-29:48:36.8	0.08±0.02		X184; B12-123:;
A057	13:36:59.51	-29:52:04.0	0.09±0.03		X186; B12-124;
A058	13:36:59.83	-29:52:26.0	0.15±0.02	0.15±0.04	
A059	13:37:00.04	-29:52:16.4	0.91±0.03	0.40±0.04	M06-31;
A060	13:37:00.42	-29:52:22.4	0.14±0.02	0.10±0.03	X219;
A061	13:37:00.57	-29:54:19.4	0.16±0.02	0.06±0.03	M06-33;
A062	13:37:01.12	-29:51:52.2	1.40±0.10	0.80±0.05	X237; Microquasar MQ1 (See text);
A063	13:37:01.36	-29:51:27.3	0.56±0.03	0.42±0.04	X245:; M06-34;
A064	13:37:01.50	-29:51:26.6	0.25±0.03	0.20±0.03	M06-34:;
A065	13:37:02.04	-29:55:32.5	0.06±0.02		
A066	13:37:02.21	-29:49:52.7	0.08±0.03	0.07±0.03	X261; B12-147;
A067	13:37:02.43	-29:51:25.9	0.20±0.03	0.15±0.04	X265; M06-35; B12-150;
A068	13:37:02.55	-29:49:56.6	0.08±0.02	0.06±0.03	

Table 2—Continued

Object	RA (J2000)	Dec. (J2000)	$S_{5\ GHz}$ (mJy)	$S_{9\ GHz}$ (mJy)	Notes[a]
A069	13:37:02.67	-29:49:59.8	0.09±0.02	0.08±0.03	
A070	13:37:03.02	-29:49:45.4	0.08±0.02	0.04±0.03	X272; B12-151;
A071	13:37:03.29	-29:52:26.7	0.21±0.02	0.10±0.02	X274; M06-36; Hard power law X-ray spectrum;
A072	13:37:03.44	-29:54:02.5	0.69±0.04	0.59±0.04	X275; M06-38; X-ray hardness suggests SNR;
A073	13:37:03.58	-29:49:41.0	0.17±0.02	0.04±0.03	X279; M06-39; SN1957D;
A074	13:37:04.04	-29:53:47.6	0.10±0.02	0.01±0.03	
A075	13:37:04.39	-29:49:39.4	0.07±0.02		X287; B12-156;
A076	13:37:04.49	-29:51:00.2	0.13±0.02	0.05±0.02	
A077	13:37:04.76	-29:50:59.5	0.15±0.02	0.08±0.02	X294; M06-40:; X-ray hardness suggests SNR;
A078	13:37:04.91	-29:49:25.8	0.15±0.02		
A079	13:37:04.92	-29:50:57.9	0.23±0.02	0.17±0.02	M06-40:;
A080	13:37:06.64	-29:53:32.9	0.19±0.02	0.10±0.03	X316; M06-41; B12-174;
A081	13:37:06.80	-29:49:24.0	0.09±0.03	0.08±0.03	
A082	13:37:06.97	-29:49:36.3	1.52±0.07	1.22±0.07	X318:; M06-42; X-ray hardness suggests SNR;
A083	13:37:07.43	-29:51:06.6	0.20±0.02	0.16±0.02	M06-43;
A084	13:37:07.47	-29:51:33.6	0.07±0.02	<0.03	X326; B12-180;
A085	13:37:07.69	-29:51:12.0	0.28±0.02	0.19±0.02	M06-45:;
A086	13:37:07.79	-29:53:14.8	0.08±0.02	0.04±0.03	M06-46;
A087	13:37:07.85	-29:52:41.9	0.09±0.03	<0.05	M06-47;
A088	13:37:07.89	-29:51:18.7	0.34±0.02	0.30±0.02	M06-48;
A089	13:37:07.96	-29:49:19.9	0.05±0.02		X330; B12-186;
A090	13:37:08.14	-29:52:56.3	0.16±0.02	0.12±0.03	X333:; M06-49; X-ray hardness suggests SNR;
A091	13:37:08.30	-29:52:11.4	0.18±0.01	0.09±0.02	M06-50;
A092	13:37:08.53	-29:52:12.8	0.11±0.02	0.03±0.02	
A093	13:37:08.76	-29:51:30.9	0.16±0.02	0.11±0.02	M06-51;
A094	13:37:08.76	-29:51:37.6	0.14±0.02	0.06±0.02	X342; B12-193;
A095	13:37:09.21	-29:51:33.5	0.17±0.02	0.06±0.03	X348; M06-52; B12-195;
A096	13:37:09.34	-29:51:00.8	0.05±0.02	0.05±0.02	M06-53; SN1923A? (See text);
A097	13:37:09.97	-29:49:11.4	0.10±0.02		
A098	13:37:10.06	-29:51:29.4	0.12±0.02	0.06±0.02	X350:; M06-54; B12-197:;
A099	13:37:11.14	-29:49:35.8	0.04±0.02		
A100	13:37:11.40	-29:49:53.3	0.07±0.03		X354; M06-55:;
A101	13:37:13.75	-29:51:42.2	0.06±0.02	0.06±0.02	
A102	13:37:15.96	-29:50:58.5	0.06±0.03		

Table 2—Continued

Object	RA (J2000)	Dec. (J2000)	$S_{5\ GHz}$ (mJy)	$S_{9\ GHz}$ (mJy)	Notes[a]
A103	13:37:17.20	-29:51:54.1	0.05±0.02		X389; B12-221;
A104	13:37:17.43	-29:51:54.4	0.21±0.04		X391; B12-223;
A105	13:37:18.37	-29:51:10.0	0.08±0.02		
A106	13:37:20.65	-29:50:26.7	0.43±0.03		
A107	13:37:20.81	-29:50:40.6	2.13±0.04		
A108	13:37:29.51	-29:50:29.4	0.58±0.07		X431:; Background galaxy;
A109	13:37:31.44	-29:52:20.4	1.10±0.09		X441:; Likely a backgroound AGN;

[a]Notes indicate objects which are spatially coincident with radio sources. If the offset between objects is larger than 1 arcsec, the name of the coincident object is followed by a ':'. Other comments provide additional information about the radio source.

Table 3.   M83 X-ray Point Sources

Object	RA (J2000)	Dec. (J2000)	Pos. Err.[a] (arcsec)	Exp. (ksec)	Rate(0.35-8.0 keV) $(10^{-3}s^{-1})$	(M-S)/T[b]	(H-M)/T[c]
X001	13:36:13.66	-29:59:38.0	0.46	514.2	0.963±0.064	-0.50± 0.08	-0.12± 0.05
X002	13:36:15.84	-29:58:00.1	0.30	395.6	3.045±0.107	-0.35± 0.04	-0.10± 0.03
X003	13:36:26.77	-29:55:36.1	0.29	514.2	0.788±0.050	-0.33± 0.08	-0.09± 0.05
X004	13:36:28.61	-29:57:20.2	0.49	514.2	0.252±0.036	-0.15± 0.16	-0.13± 0.10
X005	13:36:28.97	-29:55:39.3	0.18	514.2	1.805±0.066	-0.20± 0.04	-0.09± 0.03
X006	13:36:31.72	-29:57:09.2	0.34	514.2	0.542±0.044	-0.32± 0.09	-0.05± 0.06
X007	13:36:33.65	-30:00:18.6	0.35	739.4	0.528±0.040	0.20± 0.10	-0.10± 0.06
X008	13:36:35.24	-29:52:03.2	0.40	436.8	0.092±0.029	0.09± 0.30	-0.17± 0.26
X009	13:36:35.97	-29:51:18.7	0.24	436.8	0.377±0.040	-0.44± 0.11	0.02± 0.07
X010	13:36:36.79	-29:50:19.1	0.24	158.4	1.279±0.103	-0.37± 0.09	-0.04± 0.05
X011	13:36:37.00	-29:56:17.5	0.35	739.4	0.173±0.023	-0.41± 0.15	-0.03± 0.09
X012	13:36:37.44	-29:54:10.6	0.21	514.2	0.550±0.038	0.48± 0.07	0.13± 0.09
X013	13:36:37.69	-29:52:36.2	0.25	565.3	0.214±0.028	-0.32± 0.12	-0.07± 0.09
X014	13:36:38.56	-29:55:53.4	0.22	739.4	0.472±0.030	-0.19± 0.07	-0.07± 0.04
X015	13:36:40.00	-29:54:29.4	0.36	739.4	0.065±0.017	0.23± 0.33	0.41± 0.33
X016	13:36:40.01	-29:59:07.1	0.42	739.4	0.138±0.028	1.12± 0.63	0.31± 0.71
X017	13:36:40.28	-29:59:52.8	0.22	632.0	1.466±0.057	-0.40± 0.05	-0.10± 0.03
X018	13:36:40.49	-29:54:54.5	0.25	739.4	0.124±0.018	0.22± 0.15	0.24± 0.15
X019	13:36:40.87	-29:51:17.8	0.17	565.3	0.177±0.022	-0.80± 0.14	-0.11± 0.11
X020	13:36:40.91	-29:51:56.9	0.27	790.5	0.041±0.011	-0.81± 0.29	-0.00± 0.21
X021	13:36:41.03	-29:51:10.1	0.08	565.3	1.572±0.056	-0.15± 0.04	-0.25± 0.03
X022	13:36:41.40	-29:50:44.9	0.09	565.3	1.487±0.055	-0.17± 0.04	-0.09± 0.03
X023	13:36:42.30	-29:52:26.1	0.24	790.5	0.052±0.017	-0.88± 0.36	-0.17± 0.32
X024	13:36:42.35	-29:51:26.5	0.24	790.5	0.062±0.016	0.29± 0.27	0.32± 0.29
X025	13:36:42.79	-29:56:54.2	0.25	739.4	0.367±0.028	-0.05± 0.09	0.08± 0.05
X026	13:36:42.97	-29:52:54.1	0.13	790.5	0.302±0.024	0.43± 0.08	0.13± 0.09
X027	13:36:43.16	-29:49:54.4	0.14	724.2	0.322±0.025	-0.08± 0.08	-0.11± 0.05
X028	13:36:43.23	-29:50:55.2	0.13	790.5	0.260±0.022	0.17± 0.05	0.78± 0.12
X029	13:36:43.53	-29:51:06.9	0.03	790.5	5.431±0.085	0.08± 0.01	-0.01± 0.01
X030	13:36:43.60	-29:49:19.8	0.25	383.5	0.217±0.029	-0.24± 0.13	-0.01± 0.08
X031	13:36:44.27	-29:48:42.0	0.21	276.2	0.154±0.029	-0.37± 0.22	-0.21± 0.14
X032	13:36:44.60	-29:50:18.6	0.17	790.5	0.109±0.016	0.23± 0.13	0.44± 0.18
X033	13:36:44.99	-29:50:08.8	0.22	790.5	0.054±0.014	0.38± 0.30	0.08± 0.27
X034	13:36:45.62	-29:50:50.7	0.19	790.5	0.075±0.015	-0.22± 0.20	-0.11± 0.14

Table 3—Continued

Object	RA (J2000)	Dec. (J2000)	Pos. Err.[a] (arcsec)	Exp. (ksec)	Rate(0.35-8.0 keV) $(10^{-3}s^{-1})$	$(M-S)/T^b$	$(H-M)/T^c$
X035	13:36:45.63	-30:00:38.7	0.37	482.0	0.542±0.046	-0.69± 0.10	-0.13± 0.07
X036	13:36:45.70	-30:03:26.1	0.35	128.5	2.230±0.147	-0.38± 0.09	-0.08± 0.05
X037	13:36:45.71	-29:53:16.4	0.22	790.5	0.067±0.017	-0.33± 0.25	0.05± 0.16
X038	13:36:45.77	-29:59:12.6	0.10	632.0	5.969±0.102	-0.30± 0.02	-0.17± 0.01
X039	13:36:45.81	-29:49:50.0	0.18	790.5	0.063±0.013	-0.66± 0.23	-0.10± 0.16
X040	13:36:46.09	-30:00:01.3	0.36	632.0	0.249±0.031	-0.33± 0.15	-0.19± 0.10
X041	13:36:46.53	-29:47:08.4	0.54	276.1	0.095±0.025	-0.43± 0.30	0.37± 0.13
X042	13:36:47.16	-29:49:48.2	0.18	790.5	0.079±0.015	-0.90± 0.21	0.01± 0.15
X043	13:36:47.27	-29:51:38.9	0.23	790.5	0.035±0.013	-0.99± 0.39	-0.05± 0.32
X044	13:36:48.02	-29:53:24.6	0.06	790.5	0.978±0.039	-0.14± 0.04	-0.09± 0.03
X045	13:36:48.14	-29:46:49.4	0.19	276.1	0.506±0.048	-0.22± 0.11	-0.03± 0.06
X046	13:36:48.30	-29:52:44.6	0.13	790.5	0.164±0.019	-0.83± 0.14	-0.05± 0.10
X047	13:36:48.30	-29:51:37.0	0.18	790.5	0.044±0.013	0.61± 0.41	0.39± 0.49
X048	13:36:48.74	-29:52:29.6	0.14	790.5	0.140±0.018	0.01± 0.10	0.62± 0.13
X049	13:36:49.12	-29:52:58.4	0.04	512.0	1.834±0.062	-0.50± 0.04	-0.18± 0.03
X050	13:36:49.19	-29:51:25.0	0.14	790.5	0.093±0.015	0.10± 0.11	0.75± 0.20
X051	13:36:49.20	-29:53:03.0	0.04	179.5	1.870±0.108	-0.44± 0.06	-0.20± 0.05
X052	13:36:49.43	-29:50:14.8	0.13	790.5	0.119±0.016	0.20± 0.13	-0.06± 0.11
X053	13:36:49.80	-29:52:17.2	0.07	790.5	0.481±0.028	-0.87± 0.08	-0.04± 0.05
X054	13:36:49.92	-29:52:59.4	0.10	790.5	0.197±0.021	0.03± 0.10	0.11± 0.08
X055	13:36:49.94	-29:55:12.7	0.16	790.4	0.280±0.024	0.13± 0.08	-0.05± 0.07
X056	13:36:50.00	-29:52:30.6	0.15	790.5	0.075±0.017	-1.01± 0.27	-0.12± 0.22
X057	13:36:50.09	-29:53:08.4	0.15	790.5	0.090±0.017	-0.53± 0.22	-0.27± 0.18
X058	13:36:50.11	-29:53:20.1	0.15	790.5	0.100±0.017	-0.93± 0.20	-0.05± 0.16
X059	13:36:50.34	-29:52:33.3	0.14	790.5	0.061±0.017	-1.01± 0.34	-0.01± 0.26
X060	13:36:50.57	-29:45:32.6	0.64	276.1	0.098±0.029	0.00± 0.36	-0.16± 0.19
X061	13:36:50.59	-29:53:03.8	0.15	790.5	0.075±0.017	-0.92± 0.27	-0.14± 0.22
X062	13:36:50.66	-29:52:47.4	0.15	790.5	0.053±0.017	-0.83± 0.39	-0.18± 0.32
X063	13:36:50.85	-29:52:39.7	0.09	565.3	0.154±0.021	-0.87± 0.17	-0.05± 0.12
X064	13:36:50.91	-29:52:59.5	0.13	790.5	0.107±0.019	-0.89± 0.21	-0.05± 0.16
X065	13:36:50.96	-29:52:25.8	0.09	790.5	0.235±0.022	-0.88± 0.12	-0.08± 0.09
X066	13:36:51.10	-29:50:06.9	0.19	790.5	0.033±0.010	-0.81± 0.31	-0.03± 0.23
X067	13:36:51.19	-29:50:42.3	0.06	790.5	0.419±0.026	-0.60± 0.08	-0.17± 0.05
X068	13:36:51.21	-29:50:09.8	0.19	790.5	0.030±0.010	-0.85± 0.36	-0.08± 0.27

Table 3—Continued

Object	RA (J2000)	Dec. (J2000)	Pos. Err.[a] (arcsec)	Exp. (ksec)	Rate(0.35-8.0 keV) $(10^{-3}\mathrm{s}^{-1})$	(M-S)/T[b]	(H-M)/T[c]
X069	13:36:51.37	-30:00:00.8	0.52	353.7	0.242±0.045	0.44± 0.31	0.31± 0.30
X070	13:36:51.41	-30:00:45.1	0.51	353.7	0.389±0.048	-0.07± 0.15	0.05± 0.09
X071	13:36:51.47	-29:50:43.4	0.14	790.5	0.041±0.012	1.01± 0.58	0.28± 0.65
X072	13:36:51.52	-29:51:43.2	0.07	790.5	0.344±0.024	-0.14± 0.07	-0.07± 0.05
X073	13:36:51.65	-29:53:34.9	0.04	790.5	1.992±0.053	-0.22± 0.03	-0.10± 0.02
X074	13:36:51.65	-29:50:24.9	0.08	790.5	0.249±0.020	-0.68± 0.10	-0.15± 0.07
X075	13:36:51.74	-29:54:29.0	0.31	404.7	0.031±0.013	0.25± 0.40	-0.60± 0.30
X076	13:36:51.75	-29:54:31.1	0.14	404.7	0.114±0.020	-0.11± 0.15	-0.07± 0.12
X077	13:36:51.77	-29:52:28.4	0.15	790.5	0.049±0.014	-0.64± 0.34	-0.16± 0.25
X078	13:36:51.80	-29:53:01.6	0.13	790.5	0.071±0.018	-0.48± 0.32	-0.29± 0.25
X079	13:36:51.90	-29:53:09.4	0.13	790.5	0.071±0.018	-0.71± 0.31	-0.19± 0.24
X080	13:36:52.12	-29:52:22.8	0.16	790.5	0.038±0.013	-0.99± 0.37	-0.01± 0.28
X081	13:36:52.15	-29:46:40.6	0.37	276.1	0.127±0.027	-0.16± 0.16	0.83± 0.21
X082	13:36:52.17	-29:49:37.2	0.21	790.5	0.033±0.011	-0.88± 0.37	-0.11± 0.30
X083	13:36:52.23	-29:47:12.6	0.34	338.4	0.069±0.021	-0.21± 0.27	0.21± 0.18
X084	13:36:52.28	-29:49:20.1	0.21	790.5	0.041±0.011	-0.19± 0.26	0.03± 0.18
X085	13:36:52.33	-29:50:46.4	0.03	790.5	1.451±0.045	-0.08± 0.03	-0.06± 0.02
X086	13:36:52.35	-29:53:01.2	0.10	790.5	0.139±0.021	-0.83± 0.18	-0.03± 0.13
X087	13:36:52.39	-29:52:51.6	0.10	790.5	0.185±0.023	-1.00± 0.16	-0.03± 0.12
X088	13:36:52.41	-29:51:41.9	0.10	790.5	0.087±0.016	-0.87± 0.22	-0.09± 0.17
X089	13:36:52.46	-29:43:45.0	0.46	225.2	0.137±0.036	-0.16± 0.25	0.42± 0.18
X090	13:36:52.58	-29:55:31.6	0.23	790.4	0.092±0.018	0.21± 0.19	-0.17± 0.17
X091	13:36:52.61	-29:51:46.9	0.10	790.5	0.092±0.016	-0.61± 0.20	-0.13± 0.14
X092	13:36:52.67	-29:49:37.4	0.21	790.5	0.065±0.012	-1.01± 0.22	0.01± 0.16
X093	13:36:52.71	-29:52:41.2	0.11	790.5	0.088±0.018	-0.91± 0.26	-0.08± 0.20
X094	13:36:52.81	-29:53:27.7	0.15	790.5	0.068±0.017	0.02± 0.31	-0.24± 0.17
X095	13:36:52.82	-29:51:11.0	0.11	790.5	0.096±0.015	-0.69± 0.18	-0.11± 0.13
X096	13:36:52.82	-29:51:43.6	0.12	739.5	0.060±0.014	-0.90± 0.29	-0.10± 0.22
X097	13:36:52.83	-29:52:31.5	0.06	790.5	0.370±0.025	-0.57± 0.08	-0.20± 0.06
X098	13:36:52.88	-29:51:37.6	0.08	790.5	0.154±0.018	-0.44± 0.14	-0.23± 0.10
X099	13:36:52.88	-29:53:16.2	0.05	790.5	0.751±0.035	0.33± 0.05	-0.25± 0.04
X100	13:36:52.99	-29:52:16.3	0.17	790.5	0.040±0.012	-0.36± 0.28	-0.11± 0.20
X101	13:36:53.02	-29:53:10.1	0.12	790.5	0.099±0.019	-0.88± 0.25	-0.09± 0.19
X102	13:36:53.13	-29:50:02.5	0.11	790.5	0.088±0.014	-0.05± 0.10	0.91± 0.19

Table 3—Continued

Object	RA (J2000)	Dec. (J2000)	Pos. Err.[a] (arcsec)	Exp. (ksec)	Rate(0.35-8.0 keV) (10^{-3}s^{-1})	(M-S)/T[b]	(H-M)/T[c]
X103	13:36:53.14	-29:54:30.2	0.10	790.5	0.369±0.026	0.01± 0.07	-0.12± 0.05
X104	13:36:53.19	-29:51:32.6	0.10	790.5	0.093±0.015	-0.87± 0.20	-0.10± 0.15
X105	13:36:53.23	-29:53:25.3	0.06	790.5	0.574±0.031	-0.82± 0.07	-0.08± 0.05
X106	13:36:53.23	-29:52:47.7	0.09	790.5	0.136±0.019	-0.91± 0.17	-0.06± 0.13
X107	13:36:53.29	-29:52:42.5	0.06	790.5	0.442±0.027	-0.69± 0.08	-0.15± 0.06
X108	13:36:53.39	-29:56:08.4	0.24	790.4	0.082±0.016	-0.23± 0.18	-0.01± 0.14
X109	13:36:53.51	-29:48:21.6	0.19	790.5	0.076±0.014	-0.09± 0.14	0.76± 0.19
X110	13:36:53.61	-29:56:00.9	0.14	790.4	0.375±0.027	-0.71± 0.08	-0.09± 0.06
X111	13:36:53.61	-29:53:36.5	0.02	790.5	2.491±0.059	-0.28± 0.03	-0.25± 0.02
X112	13:36:53.66	-29:51:54.5	0.13	790.5	0.053±0.012	-0.28± 0.23	-0.23± 0.17
X113	13:36:53.68	-29:54:47.4	0.23	790.5	0.045±0.014	0.41± 0.36	-0.01± 0.33
X114	13:36:53.81	-29:53:08.3	0.11	790.5	0.105±0.018	-0.89± 0.21	-0.02± 0.15
X115	13:36:53.82	-29:51:01.1	0.13	790.5	0.045±0.011	-0.87± 0.29	-0.06± 0.22
X116	13:36:53.89	-29:48:48.4	0.10	790.5	0.274±0.022	-0.90± 0.10	-0.05± 0.07
X117	13:36:53.92	-29:51:14.6	0.03	790.5	1.094±0.039	-0.37± 0.04	-0.12± 0.03
X118	13:36:54.09	-29:49:33.1	0.12	790.5	0.124±0.016	-0.37± 0.14	-0.22± 0.10
X119	13:36:54.14	-29:52:09.4	0.13	790.5	0.062±0.012	-0.97± 0.23	-0.03± 0.17
X120	13:36:54.21	-29:53:07.3	0.11	790.5	0.112±0.018	-0.79± 0.20	-0.08± 0.14
X121	13:36:54.25	-29:50:28.0	0.08	790.5	0.145±0.016	-0.90± 0.14	-0.03± 0.10
X122	13:36:54.31	-29:51:43.7	0.12	790.5	0.057±0.011	0.22± 0.16	0.03± 0.16
X123	13:36:54.38	-29:52:57.3	0.11	790.5	0.124±0.017	-0.74± 0.16	-0.17± 0.13
X124	13:36:54.55	-29:50:26.7	0.12	790.5	0.052±0.012	-0.70± 0.26	-0.10± 0.19
X125	13:36:54.66	-29:55:19.7	0.22	790.5	0.076±0.017	-0.36± 0.21	0.03± 0.16
X126	13:36:54.79	-29:53:09.0	0.12	790.5	0.102±0.017	-0.92± 0.21	0.00± 0.15
X127	13:36:54.81	-29:52:59.8	0.11	790.5	0.108±0.017	-0.65± 0.18	-0.10± 0.13
X128	13:36:54.87	-29:50:18.7	0.10	790.5	0.098±0.014	-0.74± 0.17	-0.11± 0.13
X129	13:36:55.03	-29:52:39.4	0.06	790.5	0.308±0.022	-0.90± 0.09	-0.04± 0.07
X130	13:36:55.05	-29:52:48.5	0.19	790.5	0.022±0.010	-0.87± 0.51	-0.32± 0.50
X131	13:36:55.06	-29:53:04.6	0.05	790.5	0.473±0.028	-0.67± 0.07	-0.14± 0.05
X132	13:36:55.08	-29:53:15.4	0.15	790.5	0.039±0.013	-0.86± 0.38	-0.18± 0.32
X133	13:36:55.09	-29:53:10.9	0.13	790.5	0.063±0.014	-0.31± 0.23	0.21± 0.12
X134	13:36:55.16	-29:50:39.9	0.12	790.5	0.058±0.012	-0.93± 0.24	-0.04± 0.18
X135	13:36:55.20	-29:54:03.1	0.09	790.5	0.262±0.023	-0.27± 0.09	-0.11± 0.06
X136	13:36:55.36	-29:50:53.5	0.14	790.5	0.024±0.008	-0.92± 0.39	-0.05± 0.29

Table 3—Continued

Object	RA (J2000)	Dec. (J2000)	Pos. Err.[a] (arcsec)	Exp. (ksec)	Rate(0.35-8.0 keV) $(10^{-3}\mathrm{s}^{-1})$	(M-S)/T[b]	(H-M)/T[c]
X137	13:36:55.37	-29:48:40.7	0.19	790.5	0.048±0.013	1.10± 0.57	0.50± 0.75
X138	13:36:55.48	-29:55:09.8	0.04	790.5	3.080±0.065	-0.11± 0.02	0.01± 0.02
X139	13:36:55.56	-29:53:03.5	0.06	790.5	0.455±0.028	-0.29± 0.06	-0.03± 0.04
X140	13:36:56.04	-29:45:08.6	0.37	225.2	0.086±0.027	0.03± 0.24	0.37± 0.25
X141	13:36:56.23	-29:52:55.1	0.05	790.5	0.438±0.026	-0.04± 0.06	-0.39± 0.05
X142	13:36:56.29	-29:45:48.2	0.16	276.1	0.417±0.044	0.15± 0.11	-0.13± 0.07
X143	13:36:56.38	-29:48:17.7	0.06	611.0	0.203±0.020	-0.13± 0.10	-0.13± 0.07
X144	13:36:56.45	-29:52:57.6	0.22	790.5	0.034±0.011	-0.99± 0.38	-0.12± 0.32
X145	13:36:56.64	-29:49:12.4	0.02	790.5	5.184±0.083	-0.06± 0.01	-0.04± 0.01
X146	13:36:56.66	-29:48:19.2	0.12	790.5	0.072±0.012	-0.28± 0.19	-0.20± 0.12
X147	13:36:56.69	-29:53:21.3	0.11	790.5	0.115±0.016	-0.41± 0.15	0.04± 0.09
X148	13:36:56.79	-29:53:16.4	0.15	790.5	0.086±0.014	-0.97± 0.20	0.03± 0.14
X149	13:36:56.84	-29:49:50.3	0.18	790.5	0.030±0.010	-1.10± 0.37	-0.02± 0.29
X150	13:36:57.25	-29:51:47.2	0.07	790.5	0.100±0.014	0.45± 0.13	0.14± 0.16
X151	13:36:57.25	-29:56:00.3	0.22	790.5	0.075±0.014	-0.30± 0.15	0.23± 0.12
X152	13:36:57.27	-29:53:39.4	0.02	790.5	5.625±0.086	-0.15± 0.01	-0.03± 0.01
X153	13:36:57.29	-29:50:31.9	0.08	790.5	0.101±0.014	-0.13± 0.13	-0.02± 0.09
X154	13:36:57.37	-29:50:35.4	0.07	790.5	0.140±0.016	-0.85± 0.14	-0.07± 0.10
X155	13:36:57.48	-29:47:29.0	0.05	790.4	1.295±0.043	0.02± 0.03	0.00± 0.02
X156	13:36:57.64	-29:40:47.0	0.32	225.2	1.114±0.083	0.19± 0.05	0.57± 0.09
X157	13:36:57.69	-29:50:39.2	0.07	790.5	0.114±0.015	0.18± 0.09	0.30± 0.13
X158	13:36:57.80	-29:50:42.7	0.05	790.5	0.202±0.018	0.22± 0.08	-0.11± 0.07
X159	13:36:57.88	-29:53:02.8	0.04	790.5	0.849±0.035	-0.86± 0.05	-0.06± 0.04
X160	13:36:57.91	-29:49:23.5	0.05	790.5	0.435±0.026	0.13± 0.03	0.50± 0.07
X161	13:36:58.19	-29:51:24.1	0.04	790.5	0.306±0.022	-0.16± 0.07	-0.10± 0.05
X162	13:36:58.23	-29:52:15.8	0.05	790.5	0.187±0.018	-0.64± 0.12	-0.14± 0.08
X163	13:36:58.29	-29:48:33.3	0.03	790.5	2.099±0.054	0.06± 0.02	-0.03± 0.02
X164	13:36:58.34	-29:51:27.5	0.11	790.5	0.036±0.010	-0.93± 0.31	-0.04± 0.24
X165	13:36:58.38	-29:51:04.7	0.02	790.5	1.658±0.047	0.29± 0.02	0.16± 0.03
X166	13:36:58.56	-29:48:20.0	0.20	790.5	0.069±0.015	-0.99± 0.25	-0.17± 0.21
X167	13:36:58.61	-29:53:38.9	0.19	790.5	0.056±0.014	-1.04± 0.28	0.05± 0.20
X168	13:36:58.63	-29:52:46.4	0.02	790.5	3.919±0.072	-0.19± 0.02	-0.18± 0.01
X169	13:36:58.63	-29:52:36.8	0.09	790.5	0.089±0.013	-0.49± 0.16	-0.22± 0.12
X170	13:36:58.66	-29:51:06.7	0.08	790.5	0.090±0.013	-0.87± 0.18	-0.02± 0.13

Table 3—Continued

Object	RA (J2000)	Dec. (J2000)	Pos. Err.[a] (arcsec)	Exp. (ksec)	Rate(0.35-8.0 keV) $(10^{-3}s^{-1})$	(M-S)/T[b]	(H-M)/T[c]
X171	13:36:58.67	-29:43:36.4	0.11	225.2	2.571±0.114	-0.37± 0.05	-0.09± 0.03
X172	13:36:58.71	-29:51:00.6	0.06	790.5	0.137±0.016	-0.88± 0.14	-0.07± 0.10
X173	13:36:58.80	-29:48:31.7	0.19	790.5	0.054±0.013	0.61± 0.30	0.55± 0.43
X174	13:36:58.81	-29:44:33.3	0.31	225.2	0.165±0.035	0.25± 0.13	0.60± 0.26
X175	13:36:58.91	-29:50:38.7	0.13	790.5	0.028±0.009	0.38± 0.31	0.63± 0.47
X176	13:36:58.91	-29:52:25.6	0.12	790.5	0.029±0.011	-0.95± 0.42	-0.17± 0.35
X177	13:36:58.96	-29:50:25.0	0.12	790.5	0.048±0.011	-0.90± 0.26	-0.11± 0.20
X178	13:36:59.09	-29:53:36.2	0.07	790.5	0.254±0.021	-0.90± 0.10	-0.07± 0.08
X179	13:36:59.11	-29:54:27.7	0.19	790.5	0.052±0.014	-0.71± 0.30	-0.23± 0.26
X180	13:36:59.19	-29:51:44.8	0.08	790.5	0.050±0.014	-0.92± 0.35	-0.12± 0.28
X181	13:36:59.19	-29:51:48.0	0.06	790.5	0.074±0.017	-1.02± 0.28	0.02± 0.20
X182	13:36:59.32	-29:53:17.5	0.17	790.5	0.036±0.011	-0.97± 0.35	0.01± 0.26
X183	13:36:59.33	-29:55:08.8	0.14	790.5	0.186±0.020	-0.78± 0.13	-0.11± 0.10
X184	13:36:59.36	-29:48:37.4	0.18	790.5	0.059±0.013	-0.37± 0.25	-0.33± 0.20
X185	13:36:59.45	-29:49:59.0	0.01	790.5	17.885±0.152	-0.10± 0.01	-0.01± 0.01
X186	13:36:59.51	-29:52:04.0	0.04	790.5	0.327±0.026	-0.83± 0.10	-0.09± 0.08
X187	13:36:59.58	-29:54:13.7	0.04	790.5	1.233±0.042	0.26± 0.03	0.15± 0.03
X188	13:36:59.65	-29:51:55.8	0.05	790.5	0.098±0.020	-0.98± 0.25	-0.03± 0.18
X189	13:36:59.65	-29:52:22.7	0.10	790.5	0.055±0.011	-0.75± 0.24	-0.13± 0.18
X190	13:36:59.67	-29:51:08.8	0.05	790.5	0.144±0.016	0.36± 0.08	0.31± 0.13
X191	13:36:59.74	-29:52:16.1	0.10	790.5	0.035±0.012	-0.76± 0.39	-0.15± 0.30
X192	13:36:59.75	-29:51:54.8	0.04	790.5	0.125±0.023	-0.91± 0.22	-0.06± 0.16
X193	13:36:59.77	-29:52:05.4	0.01	790.5	5.097±0.083	-0.17± 0.02	-0.05± 0.01
X194	13:36:59.82	-29:52:02.4	0.03	790.5	0.313±0.029	-0.68± 0.12	-0.15± 0.08
X195	13:36:59.83	-29:55:26.0	0.14	790.5	0.237±0.022	-0.94± 0.11	-0.01± 0.08
X196	13:36:59.83	-29:52:20.3	0.08	790.5	0.085±0.014	-0.56± 0.18	-0.16± 0.13
X197	13:36:59.98	-29:51:57.4	0.03	790.5	0.264±0.032	-0.34± 0.14	-0.12± 0.08
X198	13:36:59.99	-29:51:50.3	0.01	790.5	3.529±0.071	-0.12± 0.02	-0.05± 0.01
X199	13:37:00.01	-29:54:17.1	0.13	790.5	0.109±0.016	-0.80± 0.17	-0.10± 0.13
X200	13:37:00.04	-29:52:19.6	0.06	790.5	0.133±0.017	-0.51± 0.14	-0.24± 0.11
X201	13:37:00.06	-29:51:37.9	0.04	790.5	0.239±0.021	-0.13± 0.09	-0.08± 0.06
X202	13:37:00.06	-29:52:02.0	0.04	790.5	0.107±0.029	-1.05± 0.32	-0.01± 0.24
X203	13:37:00.09	-29:53:29.6	0.04	790.5	0.635±0.031	0.24± 0.04	0.05± 0.04
X204	13:37:00.10	-29:51:45.7	0.03	790.5	0.650±0.033	-0.67± 0.06	-0.16± 0.05

Table 3—Continued

Object	RA (J2000)	Dec. (J2000)	Pos. Err.[a] (arcsec)	Exp. (ksec)	Rate(0.35-8.0 keV) $(10^{-3}\mathrm{s}^{-1})$	(M-S)/T[b]	(H-M)/T[c]
X205	13:37:00.18	-29:48:10.3	0.24	790.5	0.051±0.013	-0.90± 0.28	0.05± 0.20
X206	13:37:00.22	-29:51:52.4	0.02	790.5	1.080±0.045	0.05± 0.04	-0.03± 0.03
X207	13:37:00.22	-29:52:06.5	0.02	790.5	0.847±0.039	-0.86± 0.06	-0.07± 0.04
X208	13:37:00.24	-29:52:11.6	0.04	790.5	0.266±0.024	-0.81± 0.11	-0.09± 0.08
X209	13:37:00.28	-29:51:49.9	0.02	790.5	0.621±0.033	-0.29± 0.06	-0.30± 0.04
X210	13:37:00.28	-29:51:51.3	0.03	790.5	0.240±0.023	0.17± 0.11	-0.45± 0.07
X211	13:37:00.31	-29:52:18.7	0.08	790.5	0.057±0.014	-0.50± 0.28	-0.13± 0.19
X212	13:37:00.33	-29:52:05.5	0.02	790.5	0.924±0.042	-0.85± 0.06	-0.08± 0.04
X213	13:37:00.35	-29:51:52.7	0.02	790.5	1.246±0.047	-0.25± 0.04	-0.29± 0.03
X214	13:37:00.37	-29:51:44.4	0.04	790.5	0.205±0.020	-0.66± 0.12	-0.14± 0.09
X215	13:37:00.37	-29:53:23.1	0.10	790.5	0.103±0.015	-0.78± 0.17	-0.03± 0.12
X216	13:37:00.42	-29:51:59.8	0.01	790.5	4.645±0.083	-0.76± 0.02	-0.11± 0.02
X217	13:37:00.43	-29:50:54.1	0.07	790.5	0.284±0.021	-1.00± 0.10	0.00± 0.07
X218	13:37:00.44	-29:52:10.6	0.03	790.5	0.387±0.026	-0.85± 0.09	-0.07± 0.06
X219	13:37:00.44	-29:52:23.0	0.11	790.5	0.038±0.010	-0.03± 0.29	-0.37± 0.20
X220	13:37:00.48	-29:51:55.9	0.01	790.5	4.104±0.078	-0.73± 0.02	-0.11± 0.02
X221	13:37:00.50	-29:57:58.8	0.52	353.7	0.105±0.029	0.36± 0.35	0.55± 0.44
X222	13:37:00.55	-29:52:10.3	0.03	790.5	0.362±0.025	-0.90± 0.09	-0.06± 0.07
X223	13:37:00.55	-29:51:59.2	0.01	790.5	3.272±0.072	-0.82± 0.03	-0.08± 0.02
X224	13:37:00.57	-29:52:04.0	0.02	790.5	1.539±0.050	-0.83± 0.04	-0.08± 0.03
X225	13:37:00.60	-29:51:46.9	0.02	790.5	1.002±0.039	0.04± 0.04	-0.05± 0.03
X226	13:37:00.64	-29:51:53.6	0.02	790.5	0.616±0.037	-0.88± 0.07	-0.04± 0.05
X227	13:37:00.64	-29:53:19.7	0.01	790.5	6.291±0.091	-0.14± 0.01	-0.03± 0.01
X228	13:37:00.68	-29:52:06.3	0.01	790.5	2.975±0.065	-0.19± 0.02	-0.06± 0.01
X229	13:37:00.68	-29:52:00.5	0.01	790.5	1.907±0.057	-0.80± 0.04	-0.09± 0.03
X230	13:37:00.69	-29:52:04.3	0.02	790.5	1.147±0.042	-0.82± 0.05	-0.09± 0.03
X231	13:37:00.71	-29:51:56.8	0.01	790.5	2.899±0.067	-0.76± 0.03	-0.10± 0.02
X232	13:37:00.89	-29:51:58.3	0.01	790.5	1.879±0.055	-0.63± 0.04	-0.08± 0.02
X233	13:37:00.89	-29:51:56.0	0.01	790.5	9.900±0.115	-0.18± 0.01	0.02± 0.01
X234	13:37:00.95	-29:52:02.8	0.01	790.5	10.460±0.118	-0.45± 0.01	-0.16± 0.01
X235	13:37:01.03	-29:50:56.5	0.06	790.5	0.149±0.016	-0.94± 0.14	-0.00± 0.10
X236	13:37:01.06	-29:52:45.5	0.02	790.5	2.536±0.058	-0.18± 0.02	-0.06± 0.02
X237	13:37:01.11	-29:51:52.1	0.01	790.5	1.823±0.052	0.28± 0.03	-0.38± 0.02
X238	13:37:01.13	-29:41:30.9	0.49	225.2	0.305±0.051	-0.32± 0.17	0.11± 0.10

Table 3—Continued

Object	RA (J2000)	Dec. (J2000)	Pos. Err.[a] (arcsec)	Exp. (ksec)	Rate(0.35-8.0 keV) (10^{-3}s^{-1})	(M-S)/T[b]	(H-M)/T[c]
X239	13:37:01.14	-29:51:55.2	0.02	790.5	1.079±0.042	-0.81± 0.05	-0.09± 0.04
X240	13:37:01.17	-29:54:49.2	0.17	790.5	0.138±0.018	-1.05± 0.16	-0.05± 0.12
X241	13:37:01.19	-29:51:57.3	0.01	790.5	1.977±0.054	-0.75± 0.04	-0.11± 0.03
X242	13:37:01.26	-29:52:02.3	0.02	790.5	0.635±0.033	0.14± 0.03	0.74± 0.07
X243	13:37:01.28	-29:52:00.1	0.02	790.5	1.448±0.047	-0.60± 0.04	-0.12± 0.03
X244	13:37:01.30	-29:51:36.5	0.02	790.5	1.124±0.040	0.16± 0.01	0.64± 0.04
X245	13:37:01.31	-29:51:28.8	0.07	790.5	0.069±0.013	-0.82± 0.22	-0.07± 0.16
X246	13:37:01.46	-29:51:41.5	0.08	790.5	0.042±0.012	-0.81± 0.33	-0.25± 0.29
X247	13:37:01.46	-29:51:54.5	0.05	790.5	0.112±0.018	-0.81± 0.20	-0.08± 0.14
X248	13:37:01.48	-29:53:26.5	0.01	790.5	11.596±0.123	0.17± 0.01	-0.27± 0.01
X249	13:37:01.57	-29:49:59.0	0.19	790.5	0.023±0.009	-1.00± 0.42	-0.13± 0.35
X250	13:37:01.61	-29:52:02.2	0.04	790.5	0.275±0.022	-0.84± 0.10	-0.10± 0.08
X251	13:37:01.63	-29:51:28.2	0.01	790.5	7.892±0.101	-0.22± 0.01	-0.11± 0.01
X252	13:37:01.63	-29:47:42.8	0.03	790.4	3.328±0.067	0.09± 0.02	-0.06± 0.02
X253	13:37:01.67	-29:54:10.0	0.17	790.5	0.061±0.013	-0.91± 0.24	-0.09± 0.20
X254	13:37:01.68	-29:52:11.3	0.09	790.5	0.042±0.012	-0.82± 0.33	0.08± 0.21
X255	13:37:01.70	-29:54:40.6	0.23	790.5	0.030±0.013	-1.19± 0.45	-0.12± 0.40
X256	13:37:01.73	-29:51:13.4	0.04	790.5	0.234±0.019	-0.84± 0.10	-0.08± 0.08
X257	13:37:01.84	-29:51:19.1	0.09	790.5	0.036±0.011	-0.89± 0.34	0.00± 0.24
X258	13:37:02.01	-29:55:17.9	0.03	790.5	4.310±0.076	-0.16± 0.02	0.16± 0.01
X259	13:37:02.15	-29:55:06.0	0.09	790.5	0.438±0.027	-0.22± 0.06	-0.14± 0.04
X260	13:37:02.20	-29:51:44.1	0.06	790.5	0.097±0.014	0.57± 0.18	-0.02± 0.16
X261	13:37:02.21	-29:49:52.5	0.05	790.5	0.290±0.021	-0.62± 0.09	-0.16± 0.06
X262	13:37:02.31	-29:50:07.3	0.17	790.5	0.024±0.009	-1.06± 0.41	-0.02± 0.32
X263	13:37:02.34	-29:44:25.5	0.21	353.6	0.651±0.049	0.26± 0.07	0.16± 0.07
X264	13:37:02.34	-29:52:06.3	0.09	790.5	0.041±0.011	-0.92± 0.33	-0.02± 0.24
X265	13:37:02.42	-29:51:26.1	0.02	790.5	0.845±0.034	-0.80± 0.05	-0.09± 0.04
X266	13:37:02.44	-29:51:19.6	0.10	790.5	0.028±0.010	-0.84± 0.39	-0.15± 0.31
X267	13:37:02.45	-29:53:19.2	0.03	790.5	1.198±0.041	0.03± 0.03	-0.05± 0.03
X268	13:37:02.47	-29:53:45.3	0.15	790.5	0.046±0.012	0.17± 0.23	0.57± 0.30
X269	13:37:02.67	-29:48:24.4	0.17	790.5	0.093±0.014	-0.17± 0.16	-0.16± 0.11
X270	13:37:02.83	-29:51:40.5	0.07	790.5	0.041±0.012	-0.92± 0.34	-0.06± 0.25
X271	13:37:02.93	-29:57:37.9	0.28	404.6	0.288±0.034	-0.35± 0.13	-0.04± 0.08
X272	13:37:03.02	-29:49:45.5	0.06	790.5	0.258±0.021	-0.69± 0.10	-0.18± 0.07

Table 3—Continued

Object	RA (J2000)	Dec. (J2000)	Pos. Err.[a] (arcsec)	Exp. (ksec)	Rate(0.35-8.0 keV) (10^{-3}s^{-1})	(M-S)/T[b]	(H-M)/T[c]
X273	13:37:03.11	-29:55:31.5	0.20	790.5	0.044±0.015	-0.63± 0.36	-0.18± 0.31
X274	13:37:03.29	-29:52:26.7	0.03	790.5	0.668±0.031	0.12± 0.04	-0.01± 0.04
X275	13:37:03.46	-29:54:01.7	0.17	790.5	0.046±0.012	-0.86± 0.29	-0.03± 0.22
X276	13:37:03.48	-29:51:42.9	0.11	790.5	0.025±0.009	-0.91± 0.38	-0.06± 0.28
X277	13:37:03.50	-29:53:31.2	0.10	790.5	0.099±0.014	-0.85± 0.17	-0.04± 0.12
X278	13:37:03.56	-29:53:19.9	0.12	790.5	0.052±0.011	0.35± 0.21	-0.13± 0.18
X279	13:37:03.58	-29:49:40.8	0.07	790.5	0.170±0.017	0.08± 0.07	0.53± 0.11
X280	13:37:03.84	-29:52:22.9	0.14	790.5	0.035±0.010	-1.07± 0.32	0.01± 0.24
X281	13:37:03.88	-29:49:30.4	0.01	790.5	4.437±0.077	-0.18± 0.02	-0.03± 0.01
X282	13:37:03.93	-29:53:22.0	0.18	790.5	0.021±0.009	-1.04± 0.46	-0.04± 0.37
X283	13:37:04.18	-29:53:12.2	0.11	790.5	0.073±0.012	-0.84± 0.20	-0.09± 0.15
X284	13:37:04.28	-29:54:03.6	0.01	790.5	14.091±0.135	-0.12± 0.01	-0.25± 0.01
X285	13:37:04.37	-29:51:30.7	0.02	790.5	1.062±0.038	-0.20± 0.04	-0.11± 0.03
X286	13:37:04.37	-29:51:21.5	0.00	790.5	21.980±0.168	-0.11± 0.01	-0.21± 0.01
X287	13:37:04.41	-29:49:38.7	0.09	790.5	0.153±0.017	-0.83± 0.13	-0.03± 0.09
X288	13:37:04.52	-29:49:35.4	0.12	790.5	0.052±0.012	-0.85± 0.26	-0.07± 0.19
X289	13:37:04.56	-29:51:07.8	0.12	790.5	0.038±0.010	-0.85± 0.29	-0.06± 0.22
X290	13:37:04.65	-29:51:20.4	0.04	790.5	0.284±0.021	-0.26± 0.07	-0.04± 0.05
X291	13:37:04.65	-29:50:54.5	0.07	790.5	0.110±0.015	-0.22± 0.15	-0.27± 0.10
X292	13:37:04.66	-29:55:34.1	0.21	790.5	0.074±0.015	-0.86± 0.22	0.03± 0.16
X293	13:37:04.70	-29:50:40.2	0.10	790.5	0.045±0.011	0.33± 0.21	0.69± 0.34
X294	13:37:04.73	-29:50:58.9	0.09	790.5	0.041±0.011	-0.72± 0.31	-0.13± 0.23
X295	13:37:04.74	-29:48:52.0	0.05	790.5	0.710±0.032	-0.16± 0.04	-0.12± 0.03
X296	13:37:04.83	-29:51:07.4	0.12	790.5	0.034±0.010	-0.95± 0.35	0.04± 0.24
X297	13:37:04.88	-29:44:50.1	0.48	353.6	0.164±0.031	-0.27± 0.20	-0.07± 0.12
X298	13:37:04.90	-29:53:39.5	0.15	790.5	0.047±0.011	-0.93± 0.26	-0.12± 0.22
X299	13:37:05.13	-29:52:07.1	0.00	790.5	108.327±0.372	-0.33± 0.00	-0.07± 0.00
X300	13:37:05.15	-29:53:17.1	0.20	790.5	0.025±0.010	-0.94± 0.41	-0.07± 0.33
X301	13:37:05.26	-29:51:21.8	0.06	790.5	0.090±0.013	-0.47± 0.15	-0.10± 0.10
X302	13:37:05.41	-29:54:09.6	0.20	790.5	0.034±0.012	0.12± 0.29	0.65± 0.38
X303	13:37:05.47	-29:52:34.0	0.02	790.5	1.079±0.039	0.28± 0.02	0.20± 0.04
X304	13:37:05.50	-29:50:32.6	0.16	790.5	0.047±0.011	-1.01± 0.28	-0.10± 0.22
X305	13:37:05.53	-29:57:57.2	0.29	342.4	0.580±0.048	0.02± 0.09	-0.21± 0.06
X306	13:37:05.61	-29:47:28.5	0.28	790.4	0.060±0.014	-0.25± 0.21	0.00± 0.15

Table 3—Continued

Object	RA (J2000)	Dec. (J2000)	Pos. Err.[a] (arcsec)	Exp. (ksec)	Rate(0.35-8.0 keV) (10^{-3}s^{-1})	(M-S)/T[b]	(H-M)/T[c]
X307	13:37:05.76	-29:49:23.2	0.19	790.5	0.022±0.009	-0.08± 0.30	0.89± 0.41
X308	13:37:05.84	-29:48:21.9	0.25	790.5	0.046±0.012	0.28± 0.20	0.74± 0.37
X309	13:37:05.99	-29:51:59.1	0.04	790.5	0.208±0.018	0.20± 0.07	0.00± 0.08
X310	13:37:06.02	-29:55:14.4	0.08	790.5	0.576±0.030	-0.85± 0.07	-0.06± 0.05
X311	13:37:06.17	-29:54:44.2	0.09	790.5	0.299±0.023	-0.82± 0.09	-0.02± 0.06
X312	13:37:06.19	-29:52:32.0	0.06	790.5	0.126±0.015	-0.99± 0.15	-0.00± 0.11
X313	13:37:06.44	-29:50:25.4	0.14	790.5	0.036±0.010	-0.79± 0.32	0.01± 0.22
X314	13:37:06.61	-29:49:44.2	0.09	790.5	0.045±0.010	0.18± 0.11	0.76± 0.27
X315	13:37:06.63	-29:51:07.6	0.16	790.5	0.033±0.009	0.00± 0.26	-0.11± 0.19
X316	13:37:06.64	-29:53:32.7	0.06	790.5	0.343±0.024	-0.50± 0.08	-0.06± 0.05
X317	13:37:06.78	-29:50:57.8	0.07	790.5	0.122±0.015	-0.87± 0.15	-0.04± 0.11
X318	13:37:06.97	-29:49:34.6	0.20	790.5	0.046±0.011	-0.57± 0.27	-0.17± 0.21
X319	13:37:07.03	-29:49:08.1	0.23	790.5	0.037±0.012	-1.02± 0.35	0.05± 0.26
X320	13:37:07.07	-29:53:20.9	0.14	790.5	0.039±0.011	-0.68± 0.28	-0.06± 0.21
X321	13:37:07.11	-29:51:01.6	0.01	790.5	12.763±0.129	0.34± 0.01	0.10± 0.01
X322	13:37:07.12	-29:52:02.1	0.05	790.5	0.191±0.018	-0.72± 0.11	-0.11± 0.08
X323	13:37:07.15	-29:51:08.8	0.15	790.5	0.027±0.010	-0.87± 0.38	-0.09± 0.30
X324	13:37:07.29	-29:46:50.1	0.08	225.2	0.185±0.033	-0.24± 0.19	-0.13± 0.11
X325	13:37:07.40	-29:46:49.3	0.12	225.2	0.087±0.025	-0.00± 0.26	-0.19± 0.16
X326	13:37:07.48	-29:51:33.4	0.07	790.5	0.104±0.014	-0.78± 0.15	-0.07± 0.11
X327	13:37:07.52	-29:48:59.4	0.09	790.5	0.247±0.021	-0.80± 0.10	-0.10± 0.08
X328	13:37:07.56	-29:49:18.8	0.12	790.5	0.104±0.015	-0.20± 0.16	-0.42± 0.12
X329	13:37:07.68	-29:50:56.9	0.15	790.5	0.036±0.011	-0.19± 0.28	0.32± 0.18
X330	13:37:07.92	-29:49:20.3	0.15	790.5	0.045±0.011	-0.59± 0.26	-0.10± 0.19
X331	13:37:07.94	-29:52:14.3	0.13	790.5	0.024±0.009	-0.92± 0.39	-0.08± 0.31
X332	13:37:08.19	-29:49:16.8	0.11	790.5	0.158±0.017	-0.35± 0.12	-0.15± 0.08
X333	13:37:08.21	-29:52:57.4	0.14	790.5	0.031±0.010	-0.95± 0.35	0.07± 0.25
X334	13:37:08.22	-29:43:23.1	0.56	353.6	0.174±0.037	-0.88± 0.22	-0.02± 0.16
X335	13:37:08.25	-29:51:25.0	0.12	790.5	0.039±0.011	-0.61± 0.31	-0.17± 0.23
X336	13:37:08.31	-29:50:56.3	0.12	790.5	0.044±0.011	-0.88± 0.31	-0.08± 0.24
X337	13:37:08.36	-29:52:55.6	0.13	790.5	0.039±0.011	-0.76± 0.26	0.27± 0.15
X338	13:37:08.48	-29:52:01.7	0.09	790.5	0.077±0.013	-0.54± 0.18	-0.05± 0.12
X339	13:37:08.57	-29:51:35.0	0.08	790.5	0.102±0.014	-0.91± 0.16	-0.04± 0.12
X340	13:37:08.63	-29:55:30.5	0.24	790.5	0.050±0.014	0.34± 0.27	0.60± 0.41

<div align="center">Table 3—Continued</div>

Object	RA (J2000)	Dec. (J2000)	Pos. Err.[a] (arcsec)	Exp. (ksec)	Rate(0.35-8.0 keV) (10^{-3}s^{-1})	(M-S)/T[b]	(H-M)/T[c]
X341	13:37:08.69	-29:52:43.3	0.14	790.5	0.027±0.010	-1.06± 0.40	-0.04± 0.31
X342	13:37:08.77	-29:51:37.6	0.07	790.5	0.086±0.013	-0.65± 0.17	-0.18± 0.13
X343	13:37:08.79	-29:52:06.3	0.14	790.5	0.023±0.009	-0.99± 0.47	-0.31± 0.44
X344	13:37:08.79	-29:53:34.9	0.12	790.5	0.081±0.015	0.18± 0.17	0.28± 0.18
X345	13:37:09.05	-29:49:38.5	0.06	790.5	0.287±0.022	0.28± 0.06	0.22± 0.08
X346	13:37:09.07	-29:51:25.1	0.13	790.5	0.035±0.010	0.49± 0.29	0.63± 0.45
X347	13:37:09.20	-29:49:24.8	0.22	790.5	0.034±0.012	-0.65± 0.38	-0.28± 0.33
X348	13:37:09.25	-29:51:33.8	0.12	790.5	0.047±0.011	-0.42± 0.24	-0.19± 0.18
X349	13:37:09.87	-29:50:26.8	0.13	790.5	0.073±0.013	0.24± 0.18	-0.16± 0.13
X350	13:37:10.06	-29:51:28.0	0.10	790.5	0.080±0.014	-0.80± 0.21	-0.10± 0.16
X351	13:37:10.31	-29:49:18.4	0.19	790.5	0.059±0.013	0.11± 0.22	-0.10± 0.16
X352	13:37:10.36	-29:51:29.4	0.10	790.5	0.034±0.010	-0.92± 0.34	-0.08± 0.26
X353	13:37:10.99	-29:50:46.5	0.13	790.5	0.066±0.013	-0.64± 0.21	-0.17± 0.16
X354	13:37:11.48	-29:49:53.4	0.28	790.5	0.024±0.010	-1.04± 0.45	-0.09± 0.39
X355	13:37:11.48	-29:50:13.7	0.14	790.5	0.066±0.012	-0.75± 0.21	-0.08± 0.15
X356	13:37:11.50	-29:51:41.5	0.13	790.5	0.051±0.011	-0.79± 0.24	0.09± 0.16
X357	13:37:11.84	-29:48:33.9	0.13	790.4	0.127±0.015	-0.08± 0.12	-0.16± 0.08
X358	13:37:11.88	-29:52:15.5	0.05	790.5	0.416±0.025	-0.91± 0.08	-0.05± 0.06
X359	13:37:11.94	-29:48:42.0	0.14	790.4	0.134±0.016	-0.18± 0.11	-0.05± 0.08
X360	13:37:12.06	-29:50:57.1	0.09	790.5	0.142±0.016	-0.83± 0.14	-0.12± 0.11
X361	13:37:12.07	-29:49:35.0	0.15	790.5	0.098±0.014	0.21± 0.11	0.26± 0.15
X362	13:37:12.28	-29:48:03.9	0.15	610.9	0.036±0.010	-0.51± 0.28	0.13± 0.15
X363	13:37:12.45	-29:51:40.1	0.04	790.5	0.408±0.025	-0.50± 0.07	-0.25± 0.05
X364	13:37:12.45	-29:50:20.2	0.14	790.5	0.102±0.015	-0.78± 0.17	-0.06± 0.12
X365	13:37:12.52	-29:49:39.8	0.21	790.5	0.028±0.010	-1.01± 0.35	0.01± 0.28
X366	13:37:12.53	-29:51:54.9	0.02	790.5	1.844±0.050	0.33± 0.02	0.21± 0.03
X367	13:37:12.61	-29:43:10.0	0.28	353.6	1.117±0.066	-0.31± 0.07	-0.10± 0.04
X368	13:37:12.81	-29:50:12.3	0.07	790.5	0.279±0.021	-0.89± 0.10	-0.04± 0.07
X369	13:37:12.94	-29:45:09.6	0.19	632.0	0.530±0.033	-0.24± 0.07	-0.05± 0.04
X370	13:37:13.13	-29:52:38.2	0.07	790.5	0.253±0.020	0.31± 0.06	0.27± 0.09
X371	13:37:13.65	-29:52:00.1	0.18	790.5	0.033±0.010	0.12± 0.25	0.16± 0.25
X372	13:37:13.86	-29:50:06.1	0.25	790.5	0.036±0.011	0.32± 0.24	0.54± 0.39
X373	13:37:13.87	-29:56:12.0	0.34	276.1	0.178±0.041	-0.34± 0.22	0.00± 0.15
X374	13:37:14.07	-29:49:05.9	0.31	790.4	0.042±0.012	-0.09± 0.25	-0.32± 0.22

Table 3—Continued

Object	RA (J2000)	Dec. (J2000)	Pos. Err.[a] (arcsec)	Exp. (ksec)	Rate(0.35-8.0 keV) (10^{-3}s^{-1})	(M-S)/T[b]	(H-M)/T[c]
X375	13:37:14.15	-29:54:58.5	0.34	790.4	0.019±0.011	-0.96± 0.51	-0.30± 0.49
X376	13:37:14.33	-29:43:55.7	0.45	632.0	0.150±0.024	-0.23± 0.18	-0.11± 0.11
X377	13:37:14.40	-29:51:30.3	0.12	790.5	0.052±0.011	0.46± 0.23	-0.06± 0.23
X378	13:37:14.45	-29:51:48.8	0.03	790.5	1.248±0.041	0.00± 0.03	-0.12± 0.02
X379	13:37:14.67	-29:49:44.4	0.08	790.5	0.364±0.024	-0.28± 0.06	-0.09± 0.05
X380	13:37:14.75	-29:54:28.1	0.05	790.4	1.101±0.040	-0.07± 0.04	-0.13± 0.02
X381	13:37:15.01	-29:51:38.7	0.14	790.5	0.062±0.012	0.14± 0.17	0.09± 0.16
X382	13:37:15.13	-29:47:59.6	0.29	739.4	0.035±0.010	-0.19± 0.32	-0.35± 0.22
X383	13:37:16.19	-29:56:56.5	0.29	209.0	0.311±0.048	0.23± 0.15	-0.21± 0.12
X384	13:37:16.20	-29:52:02.2	0.07	790.5	0.323±0.023	0.22± 0.05	0.11± 0.07
X385	13:37:16.27	-29:41:59.6	0.41	353.6	0.721±0.060	-0.15± 0.09	-0.05± 0.06
X386	13:37:16.38	-29:49:39.4	0.02	790.4	6.105±0.090	-0.10± 0.01	-0.01± 0.01
X387	13:37:16.41	-29:46:29.0	0.32	739.4	0.102±0.016	0.35± 0.17	0.10± 0.17
X388	13:37:17.03	-29:48:15.3	0.32	739.4	0.063±0.012	-0.88± 0.23	-0.06± 0.17
X389	13:37:17.21	-29:51:53.3	0.03	790.5	0.894±0.035	-0.73± 0.05	-0.13± 0.04
X390	13:37:17.31	-29:53:37.2	0.20	790.5	0.054±0.013	-0.29± 0.22	0.10± 0.14
X391	13:37:17.40	-29:51:54.0	0.06	790.5	0.214±0.018	-0.64± 0.10	-0.14± 0.07
X392	13:37:17.56	-29:44:42.6	0.44	632.0	0.140±0.023	-0.05± 0.18	-0.06± 0.11
X393	13:37:17.98	-29:52:11.8	0.19	790.5	0.046±0.012	-0.60± 0.26	0.03± 0.17
X394	13:37:18.11	-29:43:01.5	0.42	632.0	0.252±0.029	0.14± 0.14	0.07± 0.10
X395	13:37:18.42	-29:51:18.5	0.21	790.5	0.057±0.012	0.39± 0.17	0.40± 0.27
X396	13:37:18.57	-29:52:07.6	0.26	790.5	0.034±0.011	-0.98± 0.32	0.11± 0.23
X397	13:37:18.89	-29:50:13.7	0.16	790.4	0.146±0.017	-0.04± 0.12	-0.16± 0.08
X398	13:37:18.98	-29:47:04.0	0.35	739.4	0.053±0.012	-0.42± 0.23	0.07± 0.13
X399	13:37:19.27	-29:57:09.8	0.24	51.0	0.842±0.151	-0.21± 0.16	-0.03± 0.11
X400	13:37:19.31	-29:48:38.4	0.18	739.4	0.089±0.013	0.13± 0.10	0.73± 0.19
X401	13:37:19.53	-29:47:50.7	0.52	739.4	0.031±0.011	0.30± 0.44	-0.35± 0.27
X402	13:37:19.64	-29:51:31.6	0.09	790.5	0.329±0.023	0.09± 0.04	0.50± 0.07
X403	13:37:19.79	-29:53:48.5	0.01	436.8	27.491±0.254	-0.38± 0.01	-0.15± 0.01
X404	13:37:19.98	-29:53:17.5	0.09	565.3	0.407±0.030	-0.32± 0.08	-0.11± 0.05
X405	13:37:20.02	-29:51:30.5	0.23	790.5	0.027±0.009	0.00± 0.21	0.79± 0.36
X406	13:37:20.59	-29:45:23.0	0.49	739.4	0.089±0.018	-0.27± 0.21	0.15± 0.12
X407	13:37:20.90	-29:47:23.1	0.28	739.4	0.135±0.017	0.09± 0.10	0.62± 0.15
X408	13:37:21.11	-29:52:42.6	0.28	565.3	0.056±0.015	-0.12± 0.25	-0.04± 0.19

Table 3—Continued

Object	RA (J2000)	Dec. (J2000)	Pos. Err.[a] (arcsec)	Exp. (ksec)	Rate(0.35-8.0 keV) $(10^{-3}\mathrm{s}^{-1})$	(M-S)/T[b]	(H-M)/T[c]
X409	13:37:21.43	-29:51:21.3	0.23	790.5	0.069±0.013	-0.47± 0.18	0.03± 0.12
X410	13:37:21.53	-29:57:37.5	0.30	51.0	0.880±0.155	-0.60± 0.19	-0.10± 0.13
X411	13:37:22.11	-29:40:34.2	0.42	225.2	0.826±0.078	-0.29± 0.11	-0.08± 0.07
X412	13:37:22.15	-29:52:07.9	0.16	565.3	0.236±0.024	-0.28± 0.10	-0.00± 0.07
X413	13:37:23.51	-29:50:60.0	0.37	565.2	0.062±0.016	-0.71± 0.26	-0.02± 0.19
X414	13:37:24.73	-29:58:56.2	0.27	51.0	2.570±0.249	-0.26± 0.10	-0.09± 0.06
X415	13:37:24.85	-29:48:57.4	0.26	514.3	0.207±0.025	-0.26± 0.13	-0.04± 0.08
X416	13:37:25.32	-29:49:32.0	0.22	385.8	0.070±0.017	-0.01± 0.23	0.04± 0.16
X417	13:37:25.53	-29:54:32.3	0.22	51.0	0.770±0.145	-0.42± 0.18	-0.03± 0.12
X418	13:37:26.28	-29:49:16.0	0.56	514.3	0.050±0.016	0.22± 0.28	1.09± 0.59
X419	13:37:26.29	-30:00:29.1	0.46	51.0	1.677±0.215	-0.21± 0.13	-0.22± 0.09
X420	13:37:26.47	-29:48:33.0	0.10	514.3	1.177±0.051	-0.17± 0.05	-0.05± 0.03
X421	13:37:26.68	-30:01:46.4	0.67	51.0	1.109±0.195	-0.16± 0.17	-0.14± 0.12
X422	13:37:26.83	-29:44:46.6	0.39	739.4	0.114±0.020	-0.41± 0.19	-0.05± 0.12
X423	13:37:27.29	-29:55:48.4	0.27	51.0	0.896±0.155	-0.86± 0.20	-0.08± 0.15
X424	13:37:27.36	-30:02:29.8	0.82	51.0	0.281±0.100	-0.30± 0.30	0.07± 0.20
X425	13:37:28.01	-29:42:41.4	0.43	632.0	0.318±0.036	0.03± 0.14	0.03± 0.09
X426	13:37:28.39	-29:55:23.9	0.36	51.0	0.480±0.121	0.01± 0.22	-0.35± 0.16
X427	13:37:28.50	-29:54:24.0	0.36	51.0	0.385±0.111	0.20± 0.27	-0.57± 0.19
X428	13:37:28.93	-29:49:42.7	0.13	514.3	0.626±0.038	0.23± 0.06	0.05± 0.05
X429	13:37:28.99	-29:44:13.3	0.59	581.4	0.110±0.027	0.10± 0.28	0.20± 0.21
X430	13:37:29.18	-29:52:23.3	0.36	158.3	0.123±0.037	0.40± 0.26	-0.04± 0.26
X431	13:37:29.53	-29:50:28.3	0.19	514.3	0.237±0.025	-0.31± 0.13	-0.19± 0.08
X432	13:37:29.62	-29:50:08.2	0.10	514.3	1.042±0.048	-0.26± 0.06	-0.07± 0.03
X433	13:37:29.80	-29:52:30.5	0.21	158.3	0.393±0.058	-0.16± 0.11	0.65± 0.13
X434	13:37:30.03	-29:41:56.9	0.43	632.0	0.206±0.032	-0.62± 0.17	-0.07± 0.12
X435	13:37:30.08	-29:48:28.9	0.44	514.3	0.095±0.021	-0.04± 0.25	-0.35± 0.18
X436	13:37:30.43	-29:43:20.5	0.41	514.3	0.223±0.032	0.26± 0.16	0.05± 0.14
X437	13:37:30.53	-29:59:37.0	0.27	51.0	4.850±0.336	-0.33± 0.07	-0.13± 0.05
X438	13:37:30.92	-29:42:34.9	0.17	474.0	4.115±0.101	-0.11± 0.03	-0.05± 0.02
X439	13:37:31.18	-29:43:49.8	0.42	514.3	0.296±0.036	-0.13± 0.13	-0.02± 0.08
X440	13:37:31.22	-29:51:56.2	0.15	107.4	1.240±0.118	-0.17± 0.11	0.02± 0.06
X441	13:37:31.38	-29:52:18.9	0.27	158.3	0.293±0.052	-0.49± 0.20	0.00± 0.11
X442	13:37:33.10	-29:51:01.0	0.15	385.8	0.454±0.039	-0.47± 0.11	0.11± 0.05

Table 3—Continued

Object	RA (J2000)	Dec. (J2000)	Pos. Err.[a] (arcsec)	Exp. (ksec)	Rate(0.35-8.0 keV) (10^{-3}s^{-1})	(M-S)/T[b]	(H-M)/T[c]
X443	13:37:33.40	-29:55:14.2	0.43	51.0	0.686±0.140	-0.46± 0.20	-0.05± 0.13
X444	13:37:33.40	-29:57:02.9	0.34	51.0	1.564±0.200	-0.27± 0.12	0.00± 0.08
X445	13:37:33.79	-29:59:56.4	0.83	51.0	0.549±0.147	-0.06± 0.19	0.39± 0.20
X446	13:37:34.00	-29:56:22.8	0.61	51.0	0.439±0.121	-0.38± 0.25	-0.12± 0.17
X447	13:37:35.15	-29:50:13.2	0.36	385.8	0.084±0.022	-0.01± 0.29	0.26± 0.20
X448	13:37:36.20	-29:51:22.5	0.28	107.4	0.663±0.092	0.12± 0.15	-0.21± 0.09
X449	13:37:36.75	-29:48:19.1	0.10	514.3	2.446±0.073	-0.31± 0.04	-0.07± 0.02
X450	13:37:39.37	-29:43:22.5	0.22	514.3	2.626±0.081	-0.30± 0.04	-0.11± 0.02
X451	13:37:39.66	-29:54:08.3	0.80	51.0	0.301±0.111	0.88± 0.46	-0.27± 0.42
X452	13:37:42.31	-29:49:12.6	0.43	385.8	0.127±0.028	0.00± 0.25	0.07± 0.15
X453	13:37:42.45	-29:51:36.5	0.34	107.4	0.788±0.097	-0.34± 0.17	-0.08± 0.09
X454	13:37:43.87	-29:58:48.3	0.99	51.0	0.504±0.150	-0.15± 0.24	-0.01± 0.19
X455	13:37:45.57	-29:58:00.6	1.50	51.0	0.297±0.121	-0.79± 0.38	0.05± 0.28
X456	13:37:48.54	-29:57:00.9	0.99	51.0	0.547±0.150	-0.19± 0.23	0.00± 0.17
X457	13:37:49.73	-29:55:45.0	0.63	51.0	1.435±0.203	0.00± 0.13	-0.14± 0.09
X458	13:37:50.32	-29:56:42.4	0.48	51.0	3.190±0.284	-0.24± 0.08	0.02± 0.06

[a]1-σ statistical error in the position.

[b]Hardness ratio (M-S)/T calculated from photon fluxes for the 0.35-1.1 kev (S), 1.1-2.6 kev (M) and 0.35-8.0 keV (T) bands.

[c]Hardness ratio (H-M)/T calculated from photon fluxes for the 1.1-2.6 kev (M), 2.6-8 keV (H), and 0.35-8.0 keV (T) bands.

Table 4.   M83 X-ray Point Source Fluxes & Luminosities

Object	F(0.35-8 keV)[a]	F(0.35-1.1 keV)[a]	F(1.1-2.6 keV)[a]	F(2.6-8 keV)[a]	F(0.5-2 keV)[a]	F(2-8 keV)[a]	L_X(0.35-8 keV)[b]	
X001	11.100 ± 0.715	8.910 ± 0.838	2.620 ± 0.202	1.100 ± 0.317	6.530 ± 0.412	1.900 ± 0.350	63.34 ±	4.05
X002	20.700 ± 0.713	12.400 ± 0.763	5.130 ± 0.222	3.010 ± 0.300	11.700 ± 0.436	4.270 ± 0.333	117.81 ±	4.05
X003	5.100 ± 0.307	2.840 ± 0.338	1.240 ± 0.093	0.796 ± 0.128	2.820 ± 0.186	1.090 ± 0.141	28.88 ±	1.75
X004	1.830 ± 0.250	0.729 ± 0.227	0.505 ± 0.073	0.304 ± 0.123	0.849 ± 0.127	0.515 ± 0.137	10.39 ±	1.42
X005	11.100 ± 0.395	4.760 ± 0.392	2.850 ± 0.130	1.980 ± 0.156	5.850 ± 0.248	2.720 ± 0.177	62.83 ±	2.24
X006	3.310 ± 0.257	1.790 ± 0.263	0.765 ± 0.076	0.614 ± 0.118	1.710 ± 0.147	0.855 ± 0.131	18.80 ±	1.46
X007	4.580 ± 0.338	0.699 ± 0.271	1.290 ± 0.102	0.985 ± 0.160	2.160 ± 0.179	1.370 ± 0.177	26.09 ±	1.92
X008	0.507 ± 0.144	0.126 ± 0.105	0.162 ± 0.045	0.098 ± 0.087	0.258 ± 0.073	0.137 ± 0.091	2.86 ±	0.82
X009	2.020 ± 0.200	1.340 ± 0.205	0.390 ± 0.058	0.423 ± 0.101	1.040 ± 0.116	0.504 ± 0.106	11.45 ±	1.14
X010	7.910 ± 0.598	4.640 ± 0.660	1.760 ± 0.187	1.440 ± 0.244	4.190 ± 0.379	1.890 ± 0.267	44.84 ±	3.39
X011	1.260 ± 0.159	0.790 ± 0.172	0.267 ± 0.043	0.231 ± 0.074	0.687 ± 0.089	0.279 ± 0.080	7.17 ±	0.90
X012	3.310 ± 0.219	-0.062 ± 0.086	0.847 ± 0.072	1.090 ± 0.109	1.140 ± 0.112	1.390 ± 0.121	18.77 ±	1.24
X013	1.000 ± 0.120	0.562 ± 0.106	0.249 ± 0.039	0.182 ± 0.067	0.572 ± 0.070	0.209 ± 0.068	5.70 ±	0.68
X014	3.850 ± 0.234	1.610 ± 0.224	0.975 ± 0.076	0.727 ± 0.097	1.910 ± 0.139	1.010 ± 0.111	21.86 ±	1.32
X015	0.404 ± 0.097	0.011 ± 0.081	0.073 ± 0.025	0.180 ± 0.054	0.111 ± 0.045	0.188 ± 0.056	2.29 ±	0.55
X016	0.880 ± 0.172	-0.188 ± 0.126	0.219 ± 0.045	0.331 ± 0.093	0.118 ± 0.070	0.519 ± 0.103	4.99 ±	0.98
X017	10.500 ± 0.399	6.810 ± 0.467	2.530 ± 0.125	1.470 ± 0.155	5.990 ± 0.252	2.120 ± 0.175	59.54 ±	2.27
X018	0.865 ± 0.117	0.062 ± 0.078	0.189 ± 0.033	0.325 ± 0.066	0.242 ± 0.054	0.427 ± 0.071	4.91 ±	0.67
X019	1.240 ± 0.139	1.550 ± 0.188	0.174 ± 0.036	-0.010 ± 0.041	0.865 ± 0.097	0.008 ± 0.043	7.02 ±	0.79
X020	0.312 ± 0.076	0.386 ± 0.095	0.028 ± 0.017	0.028 ± 0.036	0.223 ± 0.050	0.022 ± 0.035	1.77 ±	0.43
X021	7.440 ± 0.258	3.350 ± 0.226	2.360 ± 0.102	0.734 ± 0.086	4.580 ± 0.177	1.320 ± 0.106	42.31 ±	1.46
X022	7.360 ± 0.264	3.100 ± 0.226	1.990 ± 0.096	1.430 ± 0.115	3.850 ± 0.168	1.990 ± 0.130	41.80 ±	1.50
X023	0.207 ± 0.065	0.283 ± 0.075	0.028 ± 0.016	-0.021 ± 0.032	0.178 ± 0.041	-0.008 ± 0.033	1.18 ±	0.37
X024	0.288 ± 0.066	0.008 ± 0.051	0.068 ± 0.019	0.135 ± 0.041	0.070 ± 0.032	0.168 ± 0.043	1.63 ±	0.37
X025	2.400 ± 0.177	0.630 ± 0.149	0.536 ± 0.053	0.678 ± 0.086	0.985 ± 0.095	0.825 ± 0.093	13.60 ±	1.00
X026	1.240 ± 0.094	0.002 ± 0.044	0.380 ± 0.034	0.494 ± 0.060	0.434 ± 0.048	0.621 ± 0.064	7.02 ±	0.53
X027	2.090 ± 0.153	0.712 ± 0.129	0.580 ± 0.053	0.401 ± 0.068	1.090 ± 0.095	0.534 ± 0.074	11.83 ±	0.87
X028	1.130 ± 0.092	-0.035 ± 0.039	0.113 ± 0.021	0.808 ± 0.069	0.037 ± 0.026	0.882 ± 0.070	6.41 ±	0.52
X029	23.300 ± 0.360	5.090 ± 0.224	6.630 ± 0.136	6.520 ± 0.181	10.200 ± 0.211	8.710 ± 0.203	132.25 ±	2.04
X030	2.120 ± 0.257	0.979 ± 0.237	0.503 ± 0.084	0.492 ± 0.124	1.030 ± 0.154	0.581 ± 0.128	12.03 ±	1.46
X031	1.860 ± 0.306	1.190 ± 0.364	0.516 ± 0.105	0.131 ± 0.089	1.310 ± 0.222	0.170 ± 0.096	10.59 ±	1.74
X032	0.481 ± 0.067	0.011 ± 0.037	0.090 ± 0.019	0.241 ± 0.043	0.125 ± 0.031	0.276 ± 0.044	2.74 ±	0.38
X033	0.243 ± 0.056	0.009 ± 0.041	0.071 ± 0.017	0.083 ± 0.032	0.104 ± 0.030	0.096 ± 0.033	1.38 ±	0.31
X034	0.311 ± 0.055	0.146 ± 0.054	0.084 ± 0.018	0.053 ± 0.028	0.161 ± 0.033	0.088 ± 0.031	1.77 ±	0.31
X035	5.000 ± 0.407	5.940 ± 0.582	1.040 ± 0.116	0.127 ± 0.143	3.720 ± 0.275	0.269 ± 0.158	28.37 ±	2.31

Table 4—Continued

Object	F(0.35-8 keV)[a]	F(0.35-1.1 keV)[a]	F(1.1-2.6 keV)[a]	F(2.6-8 keV)[a]	F(0.5-2 keV)[a]	F(2-8 keV)[a]	L_X(0.35-8 keV)[b]
X036	17.800 ± 1.110	10.900 ± 1.480	4.080 ± 0.342	2.750 ± 0.370	9.580 ± 0.729	3.940 ± 0.435	100.83 ± 6.28
X037	0.262 ± 0.060	0.143 ± 0.061	0.054 ± 0.016	0.068 ± 0.033	0.134 ± 0.035	0.075 ± 0.034	1.49 ± 0.34
X038	37.200 ± 0.625	20.700 ± 0.711	10.200 ± 0.218	4.200 ± 0.191	22.700 ± 0.433	6.390 ± 0.229	211.29 ± 3.55
X039	0.323 ± 0.059	0.328 ± 0.074	0.061 ± 0.016	0.018 ± 0.025	0.216 ± 0.038	0.033 ± 0.026	1.83 ± 0.33
X040	2.120 ± 0.247	1.240 ± 0.279	0.573 ± 0.071	0.196 ± 0.106	1.370 ± 0.146	0.330 ± 0.116	12.03 ± 1.40
X041	0.730 ± 0.166	0.365 ± 0.199	0.049 ± 0.032	0.319 ± 0.086	0.151 ± 0.075	0.342 ± 0.090	4.13 ± 0.94
X042	0.346 ± 0.057	0.484 ± 0.079	0.017 ± 0.011	0.019 ± 0.024	0.250 ± 0.038	0.023 ± 0.024	1.96 ± 0.33
X043	0.140 ± 0.045	0.211 ± 0.056	0.004 ± 0.010	-0.006 ± 0.020	0.088 ± 0.029	-0.001 ± 0.021	0.79 ± 0.26
X044	3.740 ± 0.143	1.520 ± 0.118	1.050 ± 0.054	0.760 ± 0.067	2.030 ± 0.092	1.000 ± 0.073	21.21 ± 0.81
X045	3.140 ± 0.276	1.350 ± 0.293	0.750 ± 0.089	0.655 ± 0.106	1.620 ± 0.179	0.819 ± 0.118	17.81 ± 1.56
X046	0.630 ± 0.068	0.761 ± 0.086	0.061 ± 0.016	0.019 ± 0.025	0.407 ± 0.045	0.019 ± 0.025	3.57 ± 0.39
X047	0.171 ± 0.046	-0.025 ± 0.036	0.049 ± 0.014	0.096 ± 0.029	0.037 ± 0.024	0.118 ± 0.030	0.97 ± 0.26
X048	0.535 ± 0.064	0.057 ± 0.045	0.064 ± 0.017	0.369 ± 0.047	0.112 ± 0.031	0.369 ± 0.047	3.04 ± 0.36
X049	9.730 ± 0.320	7.360 ± 0.335	2.310 ± 0.117	0.476 ± 0.075	6.230 ± 0.225	1.000 ± 0.104	55.23 ± 1.81
X050	0.357 ± 0.052	0.005 ± 0.034	0.037 ± 0.012	0.278 ± 0.041	0.021 ± 0.020	0.298 ± 0.041	2.02 ± 0.29
X051	6.420 ± 0.353	4.430 ± 0.344	1.640 ± 0.136	0.338 ± 0.088	4.630 ± 0.264	0.471 ± 0.100	36.48 ± 2.00
X052	0.470 ± 0.057	0.079 ± 0.039	0.151 ± 0.021	0.128 ± 0.031	0.218 ± 0.033	0.171 ± 0.034	2.66 ± 0.32
X053	1.830 ± 0.103	2.340 ± 0.142	0.142 ± 0.022	0.035 ± 0.022	1.310 ± 0.076	0.052 ± 0.024	10.41 ± 0.59
X054	0.757 ± 0.074	0.184 ± 0.060	0.202 ± 0.026	0.274 ± 0.043	0.275 ± 0.042	0.322 ± 0.045	4.31 ± 0.42
X055	1.180 ± 0.097	0.244 ± 0.065	0.366 ± 0.035	0.322 ± 0.056	0.534 ± 0.054	0.450 ± 0.061	6.69 ± 0.55
X056	0.282 ± 0.058	0.441 ± 0.078	0.015 ± 0.012	-0.033 ± 0.016	0.221 ± 0.042	-0.035 ± 0.016	1.60 ± 0.33
X057	0.345 ± 0.059	0.285 ± 0.067	0.089 ± 0.018	-0.009 ± 0.021	0.262 ± 0.041	0.012 ± 0.024	1.96 ± 0.33
X058	0.384 ± 0.061	0.531 ± 0.080	0.022 ± 0.012	-0.004 ± 0.023	0.287 ± 0.042	0.003 ± 0.024	2.18 ± 0.35
X059	0.229 ± 0.061	0.353 ± 0.080	-0.000 ± 0.011	-0.005 ± 0.021	0.175 ± 0.043	-0.003 ± 0.021	1.30 ± 0.34
X060	0.578 ± 0.148	0.169 ± 0.152	0.171 ± 0.046	0.101 ± 0.063	0.351 ± 0.091	0.133 ± 0.070	3.29 ± 0.84
X061	0.289 ± 0.059	0.395 ± 0.076	0.028 ± 0.014	-0.027 ± 0.018	0.246 ± 0.043	-0.034 ± 0.018	1.64 ± 0.34
X062	0.199 ± 0.057	0.235 ± 0.071	0.028 ± 0.015	-0.016 ± 0.018	0.165 ± 0.041	-0.021 ± 0.019	1.13 ± 0.32
X063	0.896 ± 0.111	1.070 ± 0.144	0.069 ± 0.024	0.013 ± 0.020	0.651 ± 0.082	0.022 ± 0.024	5.09 ± 0.63
X064	0.401 ± 0.066	0.516 ± 0.084	0.029 ± 0.015	0.002 ± 0.021	0.280 ± 0.046	0.014 ± 0.023	2.28 ± 0.37
X065	0.892 ± 0.079	1.150 ± 0.107	0.081 ± 0.018	-0.018 ± 0.015	0.675 ± 0.059	-0.020 ± 0.016	5.07 ± 0.45
X066	0.149 ± 0.039	0.178 ± 0.047	0.015 ± 0.009	0.009 ± 0.017	0.084 ± 0.024	0.019 ± 0.018	0.85 ± 0.22
X067	1.610 ± 0.095	1.420 ± 0.111	0.340 ± 0.031	0.033 ± 0.020	1.180 ± 0.071	0.077 ± 0.025	9.12 ± 0.54
X068	0.133 ± 0.038	0.171 ± 0.049	0.014 ± 0.009	-0.000 ± 0.014	0.097 ± 0.026	0.008 ± 0.016	0.75 ± 0.22
X069	1.500 ± 0.262	-0.052 ± 0.226	0.326 ± 0.069	0.591 ± 0.140	0.241 ± 0.109	0.821 ± 0.155	8.51 ± 1.49
X070	3.310 ± 0.385	0.895 ± 0.361	0.726 ± 0.108	0.853 ± 0.185	1.600 ± 0.215	0.979 ± 0.196	18.77 ± 2.19

Table 4—Continued

Object	F(0.35-8 keV)[a]	F(0.35-1.1 keV)[a]	F(1.1-2.6 keV)[a]	F(2.6-8 keV)[a]	F(0.5-2 keV)[a]	F(2-8 keV)[a]	L_X(0.35-8 keV)[b]
X071	0.164 ± 0.043	-0.043 ± 0.033	0.057 ± 0.015	0.084 ± 0.025	0.056 ± 0.025	0.095 ± 0.026	0.93 ± 0.24
X072	1.290 ± 0.087	0.519 ± 0.077	0.358 ± 0.032	0.280 ± 0.040	0.654 ± 0.055	0.391 ± 0.045	7.30 ± 0.49
X073	7.680 ± 0.199	3.650 ± 0.174	2.090 ± 0.076	1.410 ± 0.087	4.140 ± 0.129	2.050 ± 0.100	43.58 ± 1.13
X074	0.977 ± 0.074	0.978 ± 0.092	0.185 ± 0.023	0.007 ± 0.015	0.688 ± 0.054	0.043 ± 0.020	5.55 ± 0.42
X075	0.186 ± 0.062	0.050 ± 0.044	0.084 ± 0.028	0.002 ± 0.023	0.104 ± 0.038	0.040 ± 0.033	1.06 ± 0.35
X076	0.601 ± 0.094	0.237 ± 0.073	0.176 ± 0.037	0.136 ± 0.049	0.310 ± 0.059	0.199 ± 0.056	3.42 ± 0.53
X077	0.185 ± 0.049	0.175 ± 0.059	0.037 ± 0.014	0.003 ± 0.016	0.147 ± 0.035	0.007 ± 0.017	1.05 ± 0.28
X078	0.269 ± 0.065	0.207 ± 0.076	0.075 ± 0.019	-0.006 ± 0.020	0.205 ± 0.047	0.005 ± 0.021	1.53 ± 0.37
X079	0.267 ± 0.064	0.283 ± 0.079	0.051 ± 0.016	-0.009 ± 0.020	0.195 ± 0.045	-0.002 ± 0.021	1.52 ± 0.36
X080	0.144 ± 0.044	0.220 ± 0.056	0.002 ± 0.010	-0.001 ± 0.016	0.101 ± 0.030	0.005 ± 0.018	0.82 ± 0.25
X081	0.800 ± 0.149	0.105 ± 0.102	0.003 ± 0.016	0.539 ± 0.099	0.063 ± 0.046	0.528 ± 0.099	4.53 ± 0.84
X082	0.131 ± 0.038	0.170 ± 0.048	0.014 ± 0.009	-0.006 ± 0.015	0.114 ± 0.026	-0.016 ± 0.014	0.74 ± 0.22
X083	0.458 ± 0.115	0.160 ± 0.100	0.076 ± 0.031	0.160 ± 0.063	0.156 ± 0.057	0.191 ± 0.068	2.61 ± 0.65
X084	0.157 ± 0.039	0.066 ± 0.035	0.038 ± 0.012	0.043 ± 0.022	0.048 ± 0.020	0.076 ± 0.025	0.89 ± 0.22
X085	5.570 ± 0.167	1.990 ± 0.125	1.600 ± 0.065	1.320 ± 0.081	2.820 ± 0.105	1.790 ± 0.092	31.67 ± 0.94
X086	0.534 ± 0.076	0.639 ± 0.098	0.049 ± 0.018	0.025 ± 0.024	0.352 ± 0.054	0.034 ± 0.025	3.04 ± 0.43
X087	0.712 ± 0.084	1.080 ± 0.117	0.010 ± 0.015	-0.024 ± 0.015	0.352 ± 0.057	-0.022 ± 0.017	4.03 ± 0.48
X088	0.324 ± 0.056	0.417 ± 0.074	0.033 ± 0.012	-0.007 ± 0.015	0.246 ± 0.040	-0.008 ± 0.015	1.84 ± 0.31
X089	1.010 ± 0.228	0.242 ± 0.188	0.113 ± 0.052	0.450 ± 0.123	0.237 ± 0.099	0.495 ± 0.131	5.73 ± 1.29
X090	0.397 ± 0.072	0.075 ± 0.050	0.138 ± 0.024	0.088 ± 0.045	0.173 ± 0.037	0.152 ± 0.048	2.25 ± 0.41
X091	0.368 ± 0.058	0.326 ± 0.069	0.073 ± 0.017	0.018 ± 0.017	0.230 ± 0.040	0.033 ± 0.019	2.09 ± 0.33
X092	0.265 ± 0.044	0.433 ± 0.065	-0.004 ± 0.006	0.002 ± 0.014	0.046 ± 0.019	0.002 ± 0.015	1.50 ± 0.25
X093	0.331 ± 0.064	0.438 ± 0.084	0.026 ± 0.015	-0.012 ± 0.016	0.251 ± 0.046	0.004 ± 0.019	1.88 ± 0.36
X094	0.260 ± 0.061	0.087 ± 0.064	0.090 ± 0.019	0.038 ± 0.025	0.150 ± 0.040	0.058 ± 0.028	1.48 ± 0.34
X095	0.362 ± 0.051	0.354 ± 0.062	0.059 ± 0.014	0.014 ± 0.017	0.233 ± 0.035	0.024 ± 0.018	2.05 ± 0.29
X096	0.239 ± 0.052	0.329 ± 0.072	0.022 ± 0.011	-0.011 ± 0.010	0.184 ± 0.038	-0.019 ± 0.010	1.36 ± 0.29
X097	1.390 ± 0.090	1.180 ± 0.102	0.318 ± 0.031	0.019 ± 0.019	0.992 ± 0.066	0.100 ± 0.027	7.88 ± 0.51
X098	0.576 ± 0.063	0.408 ± 0.069	0.154 ± 0.022	0.019 ± 0.017	0.417 ± 0.045	0.032 ± 0.019	3.27 ± 0.36
X099	2.830 ± 0.128	0.413 ± 0.085	1.090 ± 0.055	0.571 ± 0.056	1.300 ± 0.079	1.060 ± 0.073	16.04 ± 0.72
X100	0.149 ± 0.038	0.091 ± 0.038	0.038 ± 0.012	0.021 ± 0.018	0.077 ± 0.024	0.032 ± 0.020	0.85 ± 0.22
X101	0.374 ± 0.069	0.473 ± 0.090	0.034 ± 0.016	-0.008 ± 0.018	0.310 ± 0.051	-0.013 ± 0.018	2.12 ± 0.39
X102	0.352 ± 0.051	0.021 ± 0.034	0.004 ± 0.008	0.323 ± 0.043	0.009 ± 0.018	0.316 ± 0.041	2.00 ± 0.29
X103	1.410 ± 0.093	0.433 ± 0.069	0.448 ± 0.036	0.309 ± 0.049	0.762 ± 0.058	0.404 ± 0.052	7.98 ± 0.53
X104	0.345 ± 0.051	0.443 ± 0.067	0.036 ± 0.012	-0.012 ± 0.010	0.267 ± 0.037	-0.009 ± 0.012	1.96 ± 0.29
X105	2.170 ± 0.114	2.590 ± 0.151	0.247 ± 0.028	0.009 ± 0.023	1.560 ± 0.084	0.038 ± 0.026	12.34 ± 0.65

Table 4—Continued

Object	F(0.35-8 keV)[a]	F(0.35-1.1 keV)[a]	F(1.1-2.6 keV)[a]	F(2.6-8 keV)[a]	F(0.5-2 keV)[a]	F(2-8 keV)[a]	L$_X$(0.35-8 keV)[b]
X106	0.532 ± 0.070	0.710 ± 0.093	0.038 ± 0.015	-0.006 ± 0.017	0.383 ± 0.050	-0.001 ± 0.018	3.01 ± 0.40
X107	1.660 ± 0.098	1.650 ± 0.120	0.300 ± 0.030	0.003 ± 0.018	1.230 ± 0.073	0.032 ± 0.021	9.45 ± 0.56
X108	0.422 ± 0.076	0.194 ± 0.066	0.103 ± 0.024	0.097 ± 0.045	0.180 ± 0.039	0.164 ± 0.050	2.40 ± 0.43
X109	0.322 ± 0.054	0.042 ± 0.040	0.014 ± 0.011	0.241 ± 0.040	0.032 ± 0.021	0.228 ± 0.039	1.83 ± 0.31
X110	1.650 ± 0.113	1.720 ± 0.135	0.261 ± 0.031	0.070 ± 0.045	1.150 ± 0.076	0.106 ± 0.047	9.35 ± 0.64
X111	9.460 ± 0.218	5.290 ± 0.203	2.860 ± 0.087	0.654 ± 0.061	6.140 ± 0.154	1.300 ± 0.080	53.71 ± 1.24
X112	0.196 ± 0.039	0.108 ± 0.037	0.057 ± 0.014	0.016 ± 0.016	0.119 ± 0.025	0.043 ± 0.020	1.11 ± 0.22
X113	0.172 ± 0.050	0.008 ± 0.036	0.060 ± 0.016	0.059 ± 0.033	0.081 ± 0.027	0.078 ± 0.034	0.98 ± 0.28
X114	0.444 ± 0.069	0.565 ± 0.092	0.026 ± 0.015	0.015 ± 0.019	0.304 ± 0.049	0.023 ± 0.021	2.52 ± 0.39
X115	0.174 ± 0.039	0.222 ± 0.051	0.015 ± 0.009	0.002 ± 0.013	0.128 ± 0.028	-0.002 ± 0.012	0.99 ± 0.22
X116	1.110 ± 0.083	1.550 ± 0.121	0.085 ± 0.018	0.000 ± 0.019	0.831 ± 0.061	0.006 ± 0.020	6.31 ± 0.47
X117	4.110 ± 0.142	2.520 ± 0.137	1.020 ± 0.052	0.545 ± 0.053	2.430 ± 0.096	0.750 ± 0.060	23.33 ± 0.81
X118	0.480 ± 0.057	0.311 ± 0.059	0.135 ± 0.020	0.032 ± 0.020	0.302 ± 0.038	0.060 ± 0.023	2.71 ± 0.32
X119	0.233 ± 0.041	0.337 ± 0.054	0.007 ± 0.008	-0.003 ± 0.014	0.163 ± 0.028	-0.004 ± 0.015	1.32 ± 0.23
X120	0.431 ± 0.065	0.484 ± 0.082	0.054 ± 0.016	0.009 ± 0.019	0.327 ± 0.047	0.008 ± 0.019	2.44 ± 0.37
X121	0.575 ± 0.059	0.762 ± 0.081	0.035 ± 0.012	0.014 ± 0.014	0.400 ± 0.042	0.021 ± 0.015	3.27 ± 0.33
X122	0.213 ± 0.037	0.030 ± 0.022	0.067 ± 0.014	0.073 ± 0.022	0.081 ± 0.020	0.103 ± 0.025	1.21 ± 0.21
X123	0.469 ± 0.059	0.501 ± 0.071	0.081 ± 0.017	-0.016 ± 0.016	0.367 ± 0.043	-0.009 ± 0.017	2.66 ± 0.33
X124	0.204 ± 0.042	0.204 ± 0.050	0.032 ± 0.012	0.009 ± 0.013	0.137 ± 0.029	0.009 ± 0.014	1.16 ± 0.24
X125	0.289 ± 0.061	0.169 ± 0.054	0.061 ± 0.018	0.071 ± 0.038	0.162 ± 0.035	0.059 ± 0.037	1.64 ± 0.35
X126	0.383 ± 0.061	0.511 ± 0.081	0.015 ± 0.011	0.015 ± 0.021	0.255 ± 0.042	0.013 ± 0.020	2.18 ± 0.35
X127	0.404 ± 0.058	0.382 ± 0.068	0.072 ± 0.017	0.022 ± 0.020	0.286 ± 0.042	0.023 ± 0.020	2.29 ± 0.33
X128	0.375 ± 0.050	0.405 ± 0.062	0.058 ± 0.014	0.006 ± 0.015	0.265 ± 0.035	0.015 ± 0.016	2.13 ± 0.28
X129	1.160 ± 0.079	1.520 ± 0.108	0.074 ± 0.016	0.011 ± 0.017	0.824 ± 0.057	0.008 ± 0.017	6.56 ± 0.45
X130	0.084 ± 0.033	0.104 ± 0.037	0.015 ± 0.009	-0.017 ± 0.014	0.086 ± 0.023	-0.022 ± 0.013	0.48 ± 0.19
X131	1.790 ± 0.101	1.700 ± 0.120	0.317 ± 0.031	0.034 ± 0.022	1.330 ± 0.075	0.048 ± 0.023	10.13 ± 0.57
X132	0.164 ± 0.047	0.207 ± 0.059	0.023 ± 0.011	-0.015 ± 0.016	0.132 ± 0.033	-0.011 ± 0.016	0.93 ± 0.27
X133	0.250 ± 0.052	0.124 ± 0.056	0.042 ± 0.013	0.096 ± 0.028	0.084 ± 0.031	0.113 ± 0.029	1.42 ± 0.29
X134	0.222 ± 0.041	0.306 ± 0.055	0.012 ± 0.008	-0.001 ± 0.013	0.154 ± 0.029	0.001 ± 0.013	1.26 ± 0.23
X135	0.975 ± 0.080	0.519 ± 0.077	0.262 ± 0.028	0.157 ± 0.035	0.531 ± 0.051	0.258 ± 0.041	5.52 ± 0.45
X136	0.106 ± 0.030	0.135 ± 0.039	0.006 ± 0.006	-0.001 ± 0.010	0.070 ± 0.021	-0.003 ± 0.009	0.60 ± 0.17
X137	0.193 ± 0.047	-0.062 ± 0.031	0.058 ± 0.015	0.112 ± 0.030	0.037 ± 0.023	0.142 ± 0.032	1.09 ± 0.27
X138	11.900 ± 0.245	4.360 ± 0.184	3.150 ± 0.093	3.220 ± 0.130	5.650 ± 0.149	4.130 ± 0.142	67.39 ± 1.39
X139	1.730 ± 0.100	0.900 ± 0.096	0.412 ± 0.034	0.356 ± 0.045	0.889 ± 0.064	0.542 ± 0.053	9.80 ± 0.57
X140	0.534 ± 0.135	0.074 ± 0.086	0.087 ± 0.037	0.234 ± 0.075	0.119 ± 0.059	0.263 ± 0.080	3.04 ± 0.77

Table 4—Continued

Object	F(0.35-8 keV)[a]	F(0.35-1.1 keV)[a]	F(1.1-2.6 keV)[a]	F(2.6-8 keV)[a]	F(0.5-2 keV)[a]	F(2-8 keV)[a]	L$_X$(0.35-8 keV)[b]
X141	1.660 ± 0.094	0.661 ± 0.078	0.612 ± 0.041	0.086 ± 0.026	1.080 ± 0.066	0.252 ± 0.038	9.40 ± 0.53
X142	2.690 ± 0.259	0.523 ± 0.175	0.804 ± 0.096	0.566 ± 0.103	1.340 ± 0.162	0.772 ± 0.120	15.30 ± 1.47
X143	1.070 ± 0.099	0.435 ± 0.084	0.311 ± 0.037	0.190 ± 0.041	0.561 ± 0.063	0.290 ± 0.048	6.08 ± 0.56
X144	0.134 ± 0.038	0.191 ± 0.048	0.008 ± 0.009	-0.014 ± 0.013	0.004 ± 0.018	-0.010 ± 0.014	0.76 ± 0.22
X145	19.800 ± 0.311	6.620 ± 0.226	5.610 ± 0.122	4.980 ± 0.155	9.650 ± 0.192	6.680 ± 0.174	112.49 ± 1.77
X146	0.342 ± 0.053	0.188 ± 0.054	0.098 ± 0.019	0.033 ± 0.019	0.219 ± 0.036	0.061 ± 0.023	1.94 ± 0.30
X147	0.431 ± 0.056	0.273 ± 0.058	0.084 ± 0.017	0.101 ± 0.027	0.210 ± 0.035	0.111 ± 0.027	2.44 ± 0.32
X148	0.323 ± 0.049	0.465 ± 0.067	-0.000 ± 0.007	0.013 ± 0.018	0.126 ± 0.028	0.018 ± 0.018	1.83 ± 0.28
X149	0.113 ± 0.033	0.203 ± 0.046	-0.006 ± 0.004	-0.009 ± 0.012	0.078 ± 0.022	-0.008 ± 0.012	0.64 ± 0.19
X150	0.380 ± 0.048	-0.005 ± 0.023	0.123 ± 0.019	0.163 ± 0.031	0.128 ± 0.026	0.210 ± 0.034	2.16 ± 0.27
X151	0.484 ± 0.079	0.230 ± 0.065	0.080 ± 0.022	0.196 ± 0.055	0.142 ± 0.037	0.241 ± 0.056	2.74 ± 0.45
X152	21.000 ± 0.317	8.500 ± 0.250	5.650 ± 0.122	4.990 ± 0.156	10.600 ± 0.199	6.630 ± 0.174	119.07 ± 1.80
X153	0.379 ± 0.047	0.148 ± 0.040	0.103 ± 0.017	0.097 ± 0.024	0.203 ± 0.030	0.113 ± 0.025	2.15 ± 0.27
X154	0.521 ± 0.055	0.630 ± 0.071	0.050 ± 0.013	0.003 ± 0.012	0.381 ± 0.040	0.005 ± 0.014	2.96 ± 0.31
X155	6.650 ± 0.213	1.690 ± 0.149	1.770 ± 0.077	1.770 ± 0.102	2.990 ± 0.127	2.260 ± 0.112	37.75 ± 1.21
X156	7.720 ± 0.544	0.076 ± 0.212	1.050 ± 0.134	3.910 ± 0.327	1.370 ± 0.208	4.320 ± 0.344	43.83 ± 3.09
X157	0.425 ± 0.050	0.040 ± 0.028	0.105 ± 0.017	0.210 ± 0.034	0.155 ± 0.027	0.224 ± 0.034	2.41 ± 0.28
X158	0.747 ± 0.062	0.130 ± 0.037	0.259 ± 0.026	0.197 ± 0.032	0.324 ± 0.037	0.320 ± 0.039	4.23 ± 0.35
X159	3.150 ± 0.124	3.870 ± 0.167	0.285 ± 0.028	0.021 ± 0.017	2.260 ± 0.092	0.042 ± 0.019	17.84 ± 0.70
X160	1.640 ± 0.092	0.112 ± 0.038	0.296 ± 0.028	1.000 ± 0.071	0.332 ± 0.038	1.140 ± 0.073	9.27 ± 0.52
X161	1.130 ± 0.076	0.484 ± 0.063	0.322 ± 0.029	0.218 ± 0.034	0.593 ± 0.048	0.324 ± 0.040	6.38 ± 0.43
X162	0.734 ± 0.066	0.662 ± 0.078	0.137 ± 0.021	0.025 ± 0.015	0.468 ± 0.046	0.061 ± 0.020	4.15 ± 0.37
X163	8.330 ± 0.208	2.080 ± 0.134	2.470 ± 0.082	2.270 ± 0.107	3.810 ± 0.124	3.080 ± 0.121	47.38 ± 1.18
X164	0.134 ± 0.033	0.183 ± 0.042	0.007 ± 0.007	-0.001 ± 0.010	0.088 ± 0.022	0.003 ± 0.012	0.76 ± 0.18
X165	6.260 ± 0.174	0.427 ± 0.058	1.870 ± 0.070	2.650 ± 0.115	2.070 ± 0.088	3.420 ± 0.126	35.47 ± 0.99
X166	0.276 ± 0.053	0.440 ± 0.072	0.026 ± 0.012	-0.047 ± 0.016	0.219 ± 0.037	-0.045 ± 0.016	1.57 ± 0.30
X167	0.209 ± 0.046	0.331 ± 0.063	-0.010 ± 0.006	0.007 ± 0.017	0.047 ± 0.025	0.009 ± 0.017	1.19 ± 0.26
X168	14.400 ± 0.260	6.810 ± 0.220	4.300 ± 0.105	1.950 ± 0.097	8.340 ± 0.174	3.150 ± 0.120	81.58 ± 1.47
X169	0.327 ± 0.045	0.251 ± 0.047	0.083 ± 0.016	0.007 ± 0.013	0.241 ± 0.032	0.013 ± 0.015	1.86 ± 0.25
X170	0.339 ± 0.046	0.414 ± 0.059	0.022 ± 0.010	0.012 ± 0.013	0.215 ± 0.032	0.017 ± 0.013	1.92 ± 0.26
X171	15.600 ± 0.664	9.480 ± 0.756	3.750 ± 0.222	2.380 ± 0.229	9.110 ± 0.451	3.090 ± 0.259	88.67 ± 3.77
X172	0.513 ± 0.053	0.646 ± 0.072	0.044 ± 0.012	-0.003 ± 0.009	0.382 ± 0.040	-0.002 ± 0.010	2.91 ± 0.30
X173	0.219 ± 0.047	-0.039 ± 0.032	0.053 ± 0.014	0.136 ± 0.031	0.039 ± 0.023	0.166 ± 0.033	1.24 ± 0.26
X174	0.941 ± 0.172	-0.019 ± 0.058	0.131 ± 0.044	0.496 ± 0.105	0.185 ± 0.069	0.528 ± 0.109	5.35 ± 0.97
X175	0.102 ± 0.030	-0.011 ± 0.021	0.021 ± 0.009	0.074 ± 0.021	0.008 ± 0.014	0.098 ± 0.023	0.58 ± 0.17

Table 4—Continued

Object	F(0.35-8 keV)[a]	F(0.35-1.1 keV)[a]	F(1.1-2.6 keV)[a]	F(2.6-8 keV)[a]	F(0.5-2 keV)[a]	F(2-8 keV)[a]	L_X(0.35-8 keV)[b]
X176	0.112 ± 0.036	0.162 ± 0.046	0.011 ± 0.008	-0.015 ± 0.010	0.096 ± 0.025	-0.012 ± 0.012	0.64 ± 0.20
X177	0.177 ± 0.034	0.234 ± 0.045	0.016 ± 0.008	-0.009 ± 0.007	0.133 ± 0.025	-0.005 ± 0.010	1.00 ± 0.19
X178	0.953 ± 0.074	1.250 ± 0.100	0.072 ± 0.015	-0.014 ± 0.014	0.674 ± 0.053	-0.000 ± 0.016	5.40 ± 0.42
X179	0.196 ± 0.048	0.206 ± 0.055	0.041 ± 0.014	-0.013 ± 0.019	0.158 ± 0.033	-0.013 ± 0.021	1.11 ± 0.28
X180	0.187 ± 0.049	0.250 ± 0.064	0.017 ± 0.013	-0.014 ± 0.003	0.136 ± 0.036	-0.014 ± 0.007	1.06 ± 0.28
X181	0.301 ± 0.062	0.445 ± 0.084	-0.006 ± 0.013	0.003 ± 0.011	0.210 ± 0.046	-0.001 ± 0.012	1.71 ± 0.35
X182	0.132 ± 0.037	0.189 ± 0.047	0.001 ± 0.007	0.004 ± 0.013	0.066 ± 0.023	-0.003 ± 0.013	0.75 ± 0.21
X183	0.718 ± 0.072	0.819 ± 0.087	0.100 ± 0.019	-0.000 ± 0.026	0.526 ± 0.050	0.024 ± 0.028	4.08 ± 0.41
X184	0.228 ± 0.046	0.150 ± 0.050	0.070 ± 0.015	-0.002 ± 0.016	0.163 ± 0.031	0.014 ± 0.019	1.29 ± 0.26
X185	66.200 ± 0.558	24.200 ± 0.415	18.000 ± 0.216	17.200 ± 0.288	31.800 ± 0.342	22.900 ± 0.321	374.95 ± 3.17
X186	1.350 ± 0.102	1.560 ± 0.134	0.151 ± 0.025	-0.004 ± 0.012	0.974 ± 0.076	0.019 ± 0.017	7.68 ± 0.58
X187	4.590 ± 0.151	0.408 ± 0.065	1.340 ± 0.060	1.880 ± 0.097	1.630 ± 0.080	2.360 ± 0.105	26.09 ± 0.86
X188	0.414 ± 0.079	0.611 ± 0.106	0.010 ± 0.019	-0.007 ± 0.012	0.309 ± 0.059	-0.010 ± 0.013	2.35 ± 0.45
X189	0.218 ± 0.041	0.236 ± 0.050	0.033 ± 0.011	-0.000 ± 0.011	0.158 ± 0.029	0.006 ± 0.013	1.24 ± 0.23
X190	0.536 ± 0.054	-0.003 ± 0.018	0.146 ± 0.020	0.275 ± 0.038	0.136 ± 0.025	0.352 ± 0.042	3.04 ± 0.31
X191	0.145 ± 0.043	0.160 ± 0.055	0.023 ± 0.012	-0.004 ± 0.010	0.119 ± 0.032	-0.009 ± 0.010	0.82 ± 0.25
X192	0.487 ± 0.084	0.642 ± 0.107	0.034 ± 0.023	-0.006 ± 0.013	0.383 ± 0.063	-0.005 ± 0.016	2.76 ± 0.47
X193	20.500 ± 0.328	8.770 ± 0.268	5.580 ± 0.126	4.570 ± 0.156	10.600 ± 0.209	6.200 ± 0.176	116.29 ± 1.86
X194	1.230 ± 0.109	1.220 ± 0.135	0.227 ± 0.032	0.010 ± 0.015	0.928 ± 0.082	0.044 ± 0.022	7.02 ± 0.62
X195	0.937 ± 0.082	1.330 ± 0.110	0.033 ± 0.014	0.017 ± 0.032	0.654 ± 0.055	0.009 ± 0.031	5.32 ± 0.47
X196	0.371 ± 0.053	0.295 ± 0.059	0.078 ± 0.017	0.017 ± 0.015	0.273 ± 0.039	0.022 ± 0.016	2.11 ± 0.30
X197	1.000 ± 0.118	0.593 ± 0.129	0.255 ± 0.040	0.141 ± 0.032	0.624 ± 0.085	0.213 ± 0.039	5.70 ± 0.67
X198	13.100 ± 0.256	5.100 ± 0.205	3.630 ± 0.099	3.090 ± 0.123	6.570 ± 0.162	4.200 ± 0.139	74.23 ± 1.45
X199	0.413 ± 0.056	0.465 ± 0.067	0.052 ± 0.015	0.002 ± 0.020	0.262 ± 0.037	0.004 ± 0.021	2.34 ± 0.32
X200	0.568 ± 0.065	0.442 ± 0.072	0.144 ± 0.023	0.003 ± 0.012	0.420 ± 0.048	0.015 ± 0.015	3.22 ± 0.37
X201	0.893 ± 0.075	0.358 ± 0.069	0.253 ± 0.028	0.191 ± 0.032	0.474 ± 0.050	0.247 ± 0.035	5.07 ± 0.43
X202	0.422 ± 0.109	0.662 ± 0.139	-0.008 ± 0.029	-0.016 ± 0.014	0.341 ± 0.082	-0.014 ± 0.019	2.39 ± 0.62
X203	2.360 ± 0.109	0.295 ± 0.054	0.745 ± 0.045	0.833 ± 0.065	0.931 ± 0.061	1.120 ± 0.073	13.40 ± 0.62
X204	2.440 ± 0.121	2.360 ± 0.147	0.466 ± 0.038	0.007 ± 0.013	1.850 ± 0.092	0.027 ± 0.017	13.86 ± 0.68
X205	0.228 ± 0.053	0.305 ± 0.067	0.006 ± 0.010	0.023 ± 0.026	0.150 ± 0.033	0.019 ± 0.025	1.29 ± 0.30
X206	4.190 ± 0.169	1.110 ± 0.134	1.270 ± 0.066	1.150 ± 0.079	1.990 ± 0.109	1.560 ± 0.089	23.79 ± 0.96
X207	3.500 ± 0.156	4.270 ± 0.209	0.326 ± 0.036	0.003 ± 0.014	2.550 ± 0.117	0.036 ± 0.020	19.86 ± 0.88
X208	1.070 ± 0.091	1.230 ± 0.119	0.128 ± 0.022	0.000 ± 0.013	0.782 ± 0.068	0.007 ± 0.015	6.05 ± 0.51
X209	2.860 ± 0.147	1.670 ± 0.142	0.888 ± 0.059	0.098 ± 0.030	2.060 ± 0.109	0.201 ± 0.040	16.21 ± 0.84
X210	1.430 ± 0.129	0.392 ± 0.104	0.572 ± 0.057	0.097 ± 0.034	0.909 ± 0.092	0.250 ± 0.050	8.11 ± 0.73

Table 4—Continued

Object	F(0.35-8 keV)[a]	F(0.35-1.1 keV)[a]	F(1.1-2.6 keV)[a]	F(2.6-8 keV)[a]	F(0.5-2 keV)[a]	F(2-8 keV)[a]	L_X(0.35-8 keV)[b]
X211	0.232 ± 0.051	0.173 ± 0.058	0.051 ± 0.016	0.019 ± 0.016	0.158 ± 0.037	0.025 ± 0.017	1.32 ± 0.29
X212	3.710 ± 0.162	4.440 ± 0.213	0.372 ± 0.039	-0.003 ± 0.015	2.700 ± 0.121	0.046 ± 0.023	21.05 ± 0.92
X213	4.830 ± 0.179	2.670 ± 0.173	1.540 ± 0.072	0.237 ± 0.039	3.250 ± 0.130	0.553 ± 0.057	27.36 ± 1.02
X214	0.757 ± 0.071	0.702 ± 0.083	0.137 ± 0.022	0.018 ± 0.014	0.563 ± 0.053	0.041 ± 0.018	4.31 ± 0.40
X215	0.382 ± 0.050	0.407 ± 0.060	0.040 ± 0.013	0.027 ± 0.018	0.256 ± 0.035	0.025 ± 0.018	2.17 ± 0.28
X216	17.400 ± 0.306	18.800 ± 0.387	2.480 ± 0.087	0.175 ± 0.034	12.500 ± 0.229	0.422 ± 0.049	98.55 ± 1.74
X217	1.040 ± 0.073	1.560 ± 0.107	-0.004 ± 0.004	0.002 ± 0.010	0.219 ± 0.032	-0.001 ± 0.010	5.88 ± 0.41
X218	1.670 ± 0.107	2.040 ± 0.144	0.166 ± 0.025	0.003 ± 0.014	1.260 ± 0.081	-0.003 ± 0.013	9.50 ± 0.61
X219	0.157 ± 0.037	0.063 ± 0.035	0.059 ± 0.014	0.010 ± 0.014	0.107 ± 0.026	0.018 ± 0.015	0.89 ± 0.21
X220	15.100 ± 0.283	15.600 ± 0.348	2.290 ± 0.084	0.264 ± 0.040	10.800 ± 0.211	0.618 ± 0.058	85.63 ± 1.60
X221	0.627 ± 0.156	-0.033 ± 0.111	0.099 ± 0.039	0.303 ± 0.087	0.115 ± 0.062	0.358 ± 0.095	3.55 ± 0.88
X222	1.590 ± 0.106	2.060 ± 0.144	0.117 ± 0.022	-0.016 ± 0.010	1.160 ± 0.079	-0.010 ± 0.012	9.04 ± 0.60
X223	12.400 ± 0.267	14.500 ± 0.347	1.420 ± 0.071	0.072 ± 0.025	9.000 ± 0.200	0.224 ± 0.040	70.43 ± 1.52
X224	5.990 ± 0.191	6.990 ± 0.249	0.649 ± 0.049	0.033 ± 0.020	4.360 ± 0.143	0.084 ± 0.027	33.95 ± 1.09
X225	3.740 ± 0.140	1.020 ± 0.097	1.150 ± 0.057	1.000 ± 0.071	1.810 ± 0.088	1.320 ± 0.080	21.21 ± 0.80
X226	2.270 ± 0.130	2.830 ± 0.166	0.165 ± 0.034	0.046 ± 0.022	1.610 ± 0.096	0.035 ± 0.025	12.87 ± 0.73
X227	23.300 ± 0.331	9.340 ± 0.257	6.290 ± 0.128	5.620 ± 0.165	11.700 ± 0.208	7.310 ± 0.182	131.99 ± 1.88
X228	11.400 ± 0.243	5.090 ± 0.205	3.080 ± 0.093	2.420 ± 0.112	5.880 ± 0.155	3.510 ± 0.130	64.60 ± 1.38
X229	7.470 ± 0.219	8.480 ± 0.279	0.907 ± 0.059	0.056 ± 0.024	5.420 ± 0.163	0.146 ± 0.035	42.31 ± 1.24
X230	5.200 ± 0.187	6.030 ± 0.242	0.591 ± 0.048	0.021 ± 0.017	3.820 ± 0.140	0.086 ± 0.027	29.39 ± 1.06
X231	10.700 ± 0.243	11.400 ± 0.303	1.520 ± 0.070	0.148 ± 0.031	7.750 ± 0.182	0.322 ± 0.044	60.55 ± 1.38
X232	7.520 ± 0.214	6.770 ± 0.248	1.300 ± 0.066	0.619 ± 0.059	4.980 ± 0.154	0.903 ± 0.070	42.56 ± 1.21
X233	36.400 ± 0.418	15.100 ± 0.334	9.110 ± 0.155	9.940 ± 0.220	17.600 ± 0.258	12.900 ± 0.243	206.73 ± 2.37
X234	38.600 ± 0.429	27.100 ± 0.440	9.360 ± 0.157	3.100 ± 0.124	24.500 ± 0.301	5.140 ± 0.154	218.89 ± 2.43
X235	0.543 ± 0.054	0.747 ± 0.076	0.016 ± 0.008	0.015 ± 0.013	0.373 ± 0.039	0.015 ± 0.013	3.09 ± 0.31
X236	9.890 ± 0.223	4.320 ± 0.181	2.680 ± 0.086	2.120 ± 0.105	5.080 ± 0.141	2.970 ± 0.120	56.24 ± 1.26
X237	6.700 ± 0.186	1.330 ± 0.121	2.730 ± 0.086	0.863 ± 0.066	3.780 ± 0.125	1.710 ± 0.089	38.00 ± 1.06
X238	1.890 ± 0.288	0.910 ± 0.272	0.343 ± 0.080	0.543 ± 0.145	0.717 ± 0.148	0.631 ± 0.155	10.74 ± 1.63
X239	4.410 ± 0.166	5.010 ± 0.212	0.530 ± 0.044	0.021 ± 0.016	3.190 ± 0.123	0.092 ± 0.027	25.03 ± 0.94
X240	0.523 ± 0.062	0.861 ± 0.087	0.001 ± 0.009	-0.040 ± 0.020	0.165 ± 0.032	-0.033 ± 0.021	2.96 ± 0.35
X241	7.380 ± 0.197	7.860 ± 0.248	1.080 ± 0.056	0.077 ± 0.023	5.450 ± 0.149	0.175 ± 0.032	41.80 ± 1.12
X242	2.520 ± 0.125	-0.016 ± 0.065	0.318 ± 0.034	2.090 ± 0.106	0.165 ± 0.047	2.270 ± 0.107	14.31 ± 0.71
X243	5.370 ± 0.168	4.620 ± 0.192	1.040 ± 0.054	0.334 ± 0.042	3.660 ± 0.122	0.528 ± 0.051	30.40 ± 0.95
X244	4.240 ± 0.144	0.038 ± 0.029	0.661 ± 0.042	3.120 ± 0.125	0.491 ± 0.045	3.490 ± 0.128	24.09 ± 0.82
X245	0.260 ± 0.044	0.305 ± 0.056	0.028 ± 0.012	0.006 ± 0.012	0.185 ± 0.032	0.015 ± 0.014	1.47 ± 0.25

Table 4—Continued

Object	F(0.35-8 keV)[a]	F(0.35-1.1 keV)[a]	F(1.1-2.6 keV)[a]	F(2.6-8 keV)[a]	F(0.5-2 keV)[a]	F(2-8 keV)[a]	L_X(0.35-8 keV)[b]
X246	0.157 ± 0.040	0.187 ± 0.049	0.029 ± 0.012	-0.021 ± 0.008	0.118 ± 0.029	-0.016 ± 0.010	0.89 ± 0.23
X247	0.413 ± 0.062	0.472 ± 0.079	0.046 ± 0.016	0.005 ± 0.011	0.307 ± 0.046	0.002 ± 0.012	2.34 ± 0.35
X248	43.100 ± 0.451	10.300 ± 0.270	16.000 ± 0.205	6.920 ± 0.184	23.600 ± 0.294	12.000 ± 0.234	244.48 ± 2.56
X249	0.085 ± 0.028	0.130 ± 0.036	0.005 ± 0.006	-0.010 ± 0.009	0.069 ± 0.019	-0.011 ± 0.010	0.48 ± 0.16
X250	1.010 ± 0.078	1.220 ± 0.103	0.113 ± 0.019	-0.016 ± 0.008	0.747 ± 0.058	-0.003 ± 0.011	5.73 ± 0.44
X251	29.200 ± 0.371	13.900 ± 0.313	8.060 ± 0.145	5.140 ± 0.158	16.200 ± 0.243	7.420 ± 0.184	165.69 ± 2.10
X252	14.600 ± 0.288	3.400 ± 0.184	4.380 ± 0.113	3.660 ± 0.137	6.820 ± 0.174	5.000 ± 0.156	82.84 ± 1.63
X253	0.225 ± 0.043	0.296 ± 0.053	0.018 ± 0.010	-0.009 ± 0.016	0.153 ± 0.029	-0.012 ± 0.016	1.27 ± 0.25
X254	0.158 ± 0.040	0.174 ± 0.051	0.006 ± 0.008	0.023 ± 0.014	0.092 ± 0.028	0.022 ± 0.014	0.89 ± 0.23
X255	0.117 ± 0.045	0.240 ± 0.057	-0.005 ± 0.009	-0.029 ± 0.019	0.085 ± 0.028	-0.031 ± 0.020	0.67 ± 0.25
X256	0.852 ± 0.066	1.020 ± 0.087	0.086 ± 0.015	-0.001 ± 0.009	0.615 ± 0.048	0.006 ± 0.010	4.84 ± 0.37
X257	0.132 ± 0.036	0.171 ± 0.046	0.007 ± 0.008	0.007 ± 0.012	0.103 ± 0.026	0.006 ± 0.013	0.75 ± 0.20
X258	16.800 ± 0.292	6.140 ± 0.221	3.580 ± 0.099	6.150 ± 0.176	6.500 ± 0.160	7.400 ± 0.187	95.51 ± 1.66
X259	1.700 ± 0.099	0.824 ± 0.087	0.480 ± 0.037	0.261 ± 0.044	0.939 ± 0.063	0.405 ± 0.050	9.63 ± 0.56
X260	0.357 ± 0.048	-0.010 ± 0.032	0.132 ± 0.020	0.128 ± 0.026	0.126 ± 0.028	0.191 ± 0.031	2.03 ± 0.28
X261	1.080 ± 0.075	0.985 ± 0.086	0.223 ± 0.025	0.022 ± 0.017	0.781 ± 0.055	0.052 ± 0.020	6.13 ± 0.42
X262	0.090 ± 0.028	0.140 ± 0.036	-0.002 ± 0.005	-0.004 ± 0.010	0.074 ± 0.020	-0.003 ± 0.011	0.51 ± 0.16
X263	6.190 ± 0.435	0.416 ± 0.213	1.430 ± 0.138	2.060 ± 0.215	2.090 ± 0.224	2.530 ± 0.236	35.22 ± 2.47
X264	0.150 ± 0.037	0.195 ± 0.048	0.006 ± 0.008	0.003 ± 0.010	0.097 ± 0.026	0.014 ± 0.012	0.85 ± 0.21
X265	3.070 ± 0.121	3.490 ± 0.157	0.373 ± 0.031	0.034 ± 0.015	2.230 ± 0.090	0.066 ± 0.019	17.43 ± 0.68
X266	0.102 ± 0.031	0.124 ± 0.038	0.014 ± 0.008	-0.006 ± 0.007	0.083 ± 0.022	-0.009 ± 0.007	0.58 ± 0.17
X267	4.530 ± 0.149	1.250 ± 0.097	1.380 ± 0.061	1.190 ± 0.078	2.160 ± 0.090	1.670 ± 0.089	25.59 ± 0.84
X268	0.174 ± 0.040	0.005 ± 0.030	0.029 ± 0.011	0.113 ± 0.028	0.042 ± 0.021	0.118 ± 0.028	0.99 ± 0.23
X269	0.373 ± 0.053	0.160 ± 0.046	0.106 ± 0.019	0.055 ± 0.025	0.214 ± 0.033	0.093 ± 0.028	2.12 ± 0.30
X270	0.160 ± 0.040	0.215 ± 0.054	0.010 ± 0.008	-0.002 ± 0.008	0.131 ± 0.031	-0.003 ± 0.007	0.90 ± 0.23
X271	1.970 ± 0.212	1.100 ± 0.233	0.440 ± 0.064	0.368 ± 0.087	1.020 ± 0.129	0.481 ± 0.097	11.17 ± 1.20
X272	0.969 ± 0.072	0.958 ± 0.087	0.186 ± 0.023	-0.018 ± 0.012	0.752 ± 0.054	0.003 ± 0.016	5.50 ± 0.41
X273	0.174 ± 0.056	0.164 ± 0.057	0.038 ± 0.016	0.001 ± 0.029	0.138 ± 0.034	0.006 ± 0.031	0.99 ± 0.32
X274	2.530 ± 0.113	0.542 ± 0.067	0.784 ± 0.046	0.761 ± 0.063	1.130 ± 0.067	1.030 ± 0.070	14.39 ± 0.64
X275	0.173 ± 0.041	0.218 ± 0.050	0.014 ± 0.010	0.006 ± 0.018	0.116 ± 0.028	0.005 ± 0.017	0.98 ± 0.23
X276	0.095 ± 0.028	0.125 ± 0.035	0.006 ± 0.007	-0.001 ± 0.007	0.076 ± 0.020	-0.004 ± 0.007	0.54 ± 0.16
X277	0.375 ± 0.048	0.453 ± 0.061	0.032 ± 0.011	0.011 ± 0.016	0.270 ± 0.034	0.010 ± 0.017	2.13 ± 0.27
X278	0.200 ± 0.037	0.021 ± 0.024	0.073 ± 0.015	0.053 ± 0.020	0.100 ± 0.022	0.073 ± 0.022	1.13 ± 0.21
X279	0.626 ± 0.060	0.058 ± 0.034	0.104 ± 0.017	0.408 ± 0.046	0.091 ± 0.024	0.480 ± 0.048	3.55 ± 0.34
X280	0.132 ± 0.032	0.219 ± 0.046	-0.006 ± 0.003	-0.004 ± 0.009	0.034 ± 0.017	-0.007 ± 0.009	0.75 ± 0.18

Table 4—Continued

Object	F(0.35-8 keV)[a]	F(0.35-1.1 keV)[a]	F(1.1-2.6 keV)[a]	F(2.6-8 keV)[a]	F(0.5-2 keV)[a]	F(2-8 keV)[a]	L_X(0.35-8 keV)[b]
X281	16.300 ± 0.277	6.960 ± 0.224	4.310 ± 0.106	3.820 ± 0.135	8.240 ± 0.174	5.100 ± 0.151	92.72 ± 1.57
X282	0.084 ± 0.031	0.135 ± 0.040	0.000 ± 0.005	-0.006 ± 0.013	0.078 ± 0.022	-0.010 ± 0.012	0.48 ± 0.17
X283	0.281 ± 0.042	0.331 ± 0.053	0.029 ± 0.010	-0.002 ± 0.013	0.191 ± 0.029	0.014 ± 0.016	1.60 ± 0.24
X284	53.900 ± 0.512	23.400 ± 0.417	17.700 ± 0.217	5.770 ± 0.169	32.800 ± 0.353	10.400 ± 0.220	306.55 ± 2.91
X285	3.850 ± 0.135	1.800 ± 0.113	1.080 ± 0.053	0.681 ± 0.058	2.090 ± 0.087	1.020 ± 0.068	21.86 ± 0.76
X286	79.900 ± 0.607	33.300 ± 0.479	25.500 ± 0.255	11.000 ± 0.229	46.000 ± 0.406	18.500 ± 0.287	453.49 ± 3.45
X287	0.569 ± 0.057	0.666 ± 0.074	0.047 ± 0.012	0.028 ± 0.017	0.383 ± 0.040	0.035 ± 0.018	3.22 ± 0.32
X288	0.202 ± 0.040	0.242 ± 0.052	0.020 ± 0.009	0.001 ± 0.011	0.146 ± 0.028	0.010 ± 0.013	1.15 ± 0.22
X289	0.140 ± 0.031	0.172 ± 0.041	0.012 ± 0.007	0.002 ± 0.010	0.089 ± 0.022	0.001 ± 0.009	0.79 ± 0.18
X290	1.030 ± 0.073	0.523 ± 0.064	0.262 ± 0.027	0.217 ± 0.034	0.536 ± 0.046	0.302 ± 0.038	5.88 ± 0.41
X291	0.402 ± 0.051	0.212 ± 0.052	0.129 ± 0.019	0.029 ± 0.016	0.260 ± 0.036	0.057 ± 0.019	2.28 ± 0.29
X292	0.314 ± 0.060	0.410 ± 0.074	0.017 ± 0.013	0.032 ± 0.029	0.217 ± 0.038	0.023 ± 0.028	1.78 ± 0.34
X293	0.165 ± 0.035	-0.016 ± 0.025	0.030 ± 0.010	0.126 ± 0.026	0.004 ± 0.015	0.152 ± 0.028	0.93 ± 0.20
X294	0.155 ± 0.037	0.157 ± 0.044	0.025 ± 0.010	0.002 ± 0.010	0.097 ± 0.025	0.008 ± 0.012	0.88 ± 0.21
X295	2.660 ± 0.116	1.150 ± 0.096	0.775 ± 0.045	0.475 ± 0.051	1.440 ± 0.075	0.695 ± 0.059	15.07 ± 0.66
X296	0.126 ± 0.032	0.161 ± 0.042	0.001 ± 0.005	0.008 ± 0.011	0.093 ± 0.023	0.006 ± 0.010	0.71 ± 0.18
X297	1.020 ± 0.173	0.503 ± 0.178	0.251 ± 0.052	0.188 ± 0.077	0.573 ± 0.101	0.230 ± 0.085	5.78 ± 0.98
X298	0.186 ± 0.039	0.256 ± 0.048	0.017 ± 0.010	-0.014 ± 0.012	0.142 ± 0.027	-0.018 ± 0.013	1.05 ± 0.22
X299	396.000 ± 1.360	225.000 ± 1.250	97.000 ± 0.500	69.200 ± 0.576	216.000 ± 0.883	99.900 ± 0.670	2249.71 ± 7.70
X300	0.097 ± 0.032	0.135 ± 0.039	0.006 ± 0.007	-0.003 ± 0.013	0.047 ± 0.019	-0.005 ± 0.014	0.55 ± 0.18
X301	0.329 ± 0.042	0.235 ± 0.044	0.073 ± 0.014	0.038 ± 0.017	0.210 ± 0.029	0.055 ± 0.018	1.87 ± 0.24
X302	0.131 ± 0.039	0.004 ± 0.031	0.018 ± 0.011	0.092 ± 0.027	0.008 ± 0.019	0.105 ± 0.028	0.74 ± 0.22
X303	4.130 ± 0.143	0.253 ± 0.046	1.190 ± 0.057	1.850 ± 0.097	1.350 ± 0.072	2.280 ± 0.104	23.46 ± 0.81
X304	0.179 ± 0.037	0.274 ± 0.051	0.008 ± 0.007	-0.018 ± 0.006	0.092 ± 0.023	-0.015 ± 0.008	1.02 ± 0.21
X305	4.360 ± 0.341	1.290 ± 0.277	1.350 ± 0.123	0.670 ± 0.134	2.350 ± 0.213	1.070 ± 0.159	24.73 ± 1.94
X306	0.318 ± 0.066	0.150 ± 0.058	0.075 ± 0.021	0.076 ± 0.036	0.164 ± 0.037	0.094 ± 0.038	1.80 ± 0.38
X307	0.086 ± 0.031	0.008 ± 0.026	0.001 ± 0.006	0.081 ± 0.023	0.002 ± 0.015	0.076 ± 0.022	0.49 ± 0.17
X308	0.206 ± 0.048	-0.017 ± 0.030	0.031 ± 0.013	0.160 ± 0.037	0.020 ± 0.020	0.168 ± 0.038	1.17 ± 0.27
X309	0.758 ± 0.062	0.120 ± 0.035	0.240 ± 0.025	0.243 ± 0.036	0.306 ± 0.035	0.348 ± 0.041	4.31 ± 0.35
X310	2.320 ± 0.115	2.970 ± 0.160	0.224 ± 0.027	0.040 ± 0.028	1.650 ± 0.084	0.072 ± 0.031	13.15 ± 0.65
X311	1.210 ± 0.086	1.440 ± 0.113	0.108 ± 0.019	0.080 ± 0.029	0.784 ± 0.059	0.098 ± 0.030	6.84 ± 0.49
X312	0.478 ± 0.051	0.711 ± 0.074	0.003 ± 0.006	-0.000 ± 0.010	0.229 ± 0.031	-0.004 ± 0.010	2.71 ± 0.29
X313	0.132 ± 0.033	0.142 ± 0.041	0.011 ± 0.008	0.013 ± 0.013	0.078 ± 0.022	0.009 ± 0.012	0.75 ± 0.19
X314	0.181 ± 0.034	-0.006 ± 0.016	0.023 ± 0.009	0.148 ± 0.029	0.017 ± 0.013	0.156 ± 0.029	1.03 ± 0.19
X315	0.121 ± 0.030	0.039 ± 0.025	0.039 ± 0.011	0.027 ± 0.015	0.054 ± 0.018	0.051 ± 0.018	0.69 ± 0.17

Table 4—Continued

Object	F(0.35-8 keV)[a]	F(0.35-1.1 keV)[a]	F(1.1-2.6 keV)[a]	F(2.6-8 keV)[a]	F(0.5-2 keV)[a]	F(2-8 keV)[a]	L_X(0.35-8 keV)[b]
X316	1.280 ± 0.083	0.947 ± 0.087	0.256 ± 0.027	0.176 ± 0.033	0.809 ± 0.057	0.197 ± 0.034	7.27 ± 0.47
X317	0.455 ± 0.052	0.567 ± 0.068	0.035 ± 0.012	0.011 ± 0.014	0.323 ± 0.038	0.019 ± 0.016	2.58 ± 0.30
X318	0.172 ± 0.038	0.143 ± 0.040	0.037 ± 0.012	0.005 ± 0.015	0.117 ± 0.025	0.012 ± 0.016	0.98 ± 0.21
X319	0.139 ± 0.041	0.217 ± 0.052	-0.005 ± 0.007	0.006 ± 0.018	0.091 ± 0.026	-0.002 ± 0.017	0.79 ± 0.23
X320	0.145 ± 0.036	0.141 ± 0.038	0.022 ± 0.011	0.011 ± 0.015	0.101 ± 0.024	0.004 ± 0.015	0.82 ± 0.20
X321	47.500 ± 0.474	2.720 ± 0.140	15.100 ± 0.199	18.600 ± 0.301	16.400 ± 0.246	25.100 ± 0.338	268.55 ± 2.69
X322	0.694 ± 0.059	0.703 ± 0.071	0.107 ± 0.017	0.018 ± 0.014	0.477 ± 0.042	0.045 ± 0.018	3.93 ± 0.33
X323	0.102 ± 0.031	0.132 ± 0.038	0.010 ± 0.008	-0.002 ± 0.010	0.082 ± 0.022	-0.008 ± 0.010	0.58 ± 0.18
X324	2.300 ± 0.358	1.140 ± 0.362	0.622 ± 0.128	0.353 ± 0.127	1.300 ± 0.239	0.470 ± 0.144	13.05 ± 2.03
X325	1.100 ± 0.249	0.339 ± 0.200	0.338 ± 0.095	0.175 ± 0.091	0.568 ± 0.158	0.298 ± 0.116	6.21 ± 1.41
X326	0.381 ± 0.045	0.425 ± 0.057	0.047 ± 0.012	0.012 ± 0.013	0.282 ± 0.033	0.011 ± 0.013	2.16 ± 0.26
X327	0.920 ± 0.073	1.050 ± 0.092	0.117 ± 0.019	-0.001 ± 0.017	0.679 ± 0.053	0.008 ± 0.019	5.22 ± 0.41
X328	0.391 ± 0.051	0.202 ± 0.047	0.136 ± 0.020	-0.004 ± 0.014	0.289 ± 0.036	0.016 ± 0.017	2.22 ± 0.29
X329	0.135 ± 0.036	0.047 ± 0.035	0.022 ± 0.010	0.065 ± 0.022	0.031 ± 0.020	0.079 ± 0.023	0.77 ± 0.20
X330	0.174 ± 0.038	0.151 ± 0.042	0.034 ± 0.011	0.015 ± 0.016	0.121 ± 0.026	0.023 ± 0.017	0.99 ± 0.21
X331	0.091 ± 0.028	0.124 ± 0.035	0.007 ± 0.006	-0.004 ± 0.011	0.070 ± 0.020	-0.006 ± 0.010	0.52 ± 0.16
X332	0.586 ± 0.060	0.361 ± 0.059	0.155 ± 0.021	0.068 ± 0.024	0.346 ± 0.040	0.097 ± 0.026	3.32 ± 0.34
X333	0.119 ± 0.034	0.169 ± 0.044	-0.002 ± 0.006	0.011 ± 0.015	0.075 ± 0.023	0.013 ± 0.014	0.67 ± 0.19
X334	1.110 ± 0.216	1.920 ± 0.324	0.092 ± 0.046	0.054 ± 0.094	0.851 ± 0.132	0.023 ± 0.098	6.28 ± 1.22
X335	0.148 ± 0.036	0.130 ± 0.041	0.030 ± 0.011	0.003 ± 0.010	0.103 ± 0.025	0.001 ± 0.011	0.84 ± 0.20
X336	0.160 ± 0.037	0.200 ± 0.048	0.014 ± 0.008	-0.003 ± 0.010	0.108 ± 0.026	-0.002 ± 0.011	0.91 ± 0.21
X337	0.149 ± 0.035	0.153 ± 0.040	-0.002 ± 0.006	0.053 ± 0.021	0.076 ± 0.022	0.046 ± 0.019	0.84 ± 0.20
X338	0.281 ± 0.043	0.223 ± 0.048	0.054 ± 0.013	0.037 ± 0.018	0.166 ± 0.029	0.058 ± 0.020	1.60 ± 0.24
X339	0.372 ± 0.046	0.496 ± 0.062	0.023 ± 0.009	0.002 ± 0.010	0.288 ± 0.034	-0.004 ± 0.010	2.11 ± 0.26
X340	0.222 ± 0.057	-0.015 ± 0.037	0.040 ± 0.015	0.140 ± 0.039	0.042 ± 0.026	0.158 ± 0.039	1.26 ± 0.32
X341	0.105 ± 0.033	0.172 ± 0.044	-0.001 ± 0.006	-0.008 ± 0.010	0.086 ± 0.024	-0.015 ± 0.009	0.60 ± 0.19
X342	0.321 ± 0.043	0.302 ± 0.050	0.065 ± 0.014	-0.002 ± 0.009	0.246 ± 0.032	0.009 ± 0.012	1.82 ± 0.24
X343	0.083 ± 0.029	0.127 ± 0.038	0.012 ± 0.007	-0.024 ± 0.004	0.084 ± 0.022	-0.019 ± 0.006	0.47 ± 0.16
X344	0.305 ± 0.052	0.030 ± 0.035	0.073 ± 0.018	0.141 ± 0.031	0.102 ± 0.030	0.156 ± 0.033	1.73 ± 0.30
X345	1.060 ± 0.075	0.061 ± 0.034	0.297 ± 0.028	0.480 ± 0.051	0.323 ± 0.037	0.612 ± 0.055	6.03 ± 0.43
X346	0.129 ± 0.033	-0.021 ± 0.022	0.029 ± 0.010	0.094 ± 0.024	0.021 ± 0.017	0.104 ± 0.024	0.73 ± 0.19
X347	0.129 ± 0.040	0.126 ± 0.044	0.031 ± 0.012	-0.010 ± 0.016	0.102 ± 0.027	-0.013 ± 0.015	0.73 ± 0.22
X348	0.177 ± 0.037	0.124 ± 0.038	0.047 ± 0.013	0.012 ± 0.013	0.119 ± 0.025	0.019 ± 0.015	1.00 ± 0.21
X349	0.268 ± 0.042	0.048 ± 0.031	0.096 ± 0.017	0.064 ± 0.022	0.131 ± 0.026	0.091 ± 0.024	1.52 ± 0.24
X350	0.294 ± 0.047	0.335 ± 0.060	0.038 ± 0.012	-0.000 ± 0.011	0.204 ± 0.034	0.009 ± 0.013	1.67 ± 0.27

Table 4—Continued

Object	F(0.35-8 keV)[a]	F(0.35-1.1 keV)[a]	F(1.1-2.6 keV)[a]	F(2.6-8 keV)[a]	F(0.5-2 keV)[a]	F(2-8 keV)[a]	L_X(0.35-8 keV)[b]
X351	0.221 ± 0.044	0.053 ± 0.036	0.073 ± 0.016	0.055 ± 0.024	0.113 ± 0.026	0.072 ± 0.025	1.26 ± 0.25
X352	0.138 ± 0.035	0.187 ± 0.048	0.010 ± 0.007	-0.005 ± 0.008	0.098 ± 0.025	-0.002 ± 0.009	0.79 ± 0.20
X353	0.247 ± 0.042	0.233 ± 0.049	0.051 ± 0.013	0.001 ± 0.015	0.170 ± 0.029	0.012 ± 0.016	1.40 ± 0.24
X354	0.090 ± 0.034	0.144 ± 0.041	0.002 ± 0.007	-0.010 ± 0.016	0.062 ± 0.021	-0.012 ± 0.016	0.51 ± 0.19
X355	0.249 ± 0.041	0.268 ± 0.050	0.034 ± 0.011	0.009 ± 0.015	0.160 ± 0.027	0.028 ± 0.017	1.41 ± 0.23
X356	0.187 ± 0.037	0.204 ± 0.044	0.010 ± 0.008	0.032 ± 0.017	0.115 ± 0.024	0.028 ± 0.017	1.06 ± 0.21
X357	0.935 ± 0.102	0.346 ± 0.086	0.281 ± 0.038	0.159 ± 0.043	0.547 ± 0.067	0.209 ± 0.048	5.29 ± 0.58
X358	1.570 ± 0.089	2.070 ± 0.125	0.102 ± 0.017	0.002 ± 0.013	1.090 ± 0.065	0.023 ± 0.017	8.89 ± 0.51
X359	0.934 ± 0.099	0.398 ± 0.087	0.244 ± 0.035	0.205 ± 0.047	0.477 ± 0.062	0.250 ± 0.050	5.29 ± 0.56
X360	0.530 ± 0.055	0.639 ± 0.072	0.066 ± 0.014	-0.018 ± 0.011	0.409 ± 0.041	-0.007 ± 0.013	3.01 ± 0.31
X361	0.365 ± 0.049	0.032 ± 0.027	0.096 ± 0.017	0.173 ± 0.034	0.124 ± 0.025	0.204 ± 0.035	2.07 ± 0.28
X362	0.194 ± 0.044	0.138 ± 0.053	0.027 ± 0.011	0.055 ± 0.021	0.085 ± 0.025	0.059 ± 0.021	1.10 ± 0.25
X363	1.510 ± 0.087	1.180 ± 0.094	0.391 ± 0.032	0.003 ± 0.014	1.120 ± 0.065	0.069 ± 0.022	8.59 ± 0.49
X364	0.374 ± 0.049	0.407 ± 0.060	0.045 ± 0.012	0.015 ± 0.018	0.269 ± 0.034	0.025 ± 0.019	2.12 ± 0.28
X365	0.108 ± 0.032	0.166 ± 0.039	-0.001 ± 0.005	0.001 ± 0.016	0.070 ± 0.019	-0.006 ± 0.015	0.61 ± 0.18
X366	6.820 ± 0.180	0.232 ± 0.046	1.950 ± 0.071	3.070 ± 0.122	1.960 ± 0.086	4.040 ± 0.135	38.76 ± 1.02
X367	7.950 ± 0.450	4.390 ± 0.494	2.000 ± 0.145	1.230 ± 0.175	4.160 ± 0.277	1.850 ± 0.203	45.10 ± 2.56
X368	1.040 ± 0.074	1.350 ± 0.101	0.072 ± 0.015	0.017 ± 0.019	0.705 ± 0.052	0.020 ± 0.019	5.90 ± 0.42
X369	3.280 ± 0.197	1.510 ± 0.195	0.800 ± 0.064	0.650 ± 0.081	1.670 ± 0.120	0.869 ± 0.092	18.65 ± 1.11
X370	0.971 ± 0.073	0.028 ± 0.028	0.262 ± 0.027	0.469 ± 0.050	0.283 ± 0.035	0.565 ± 0.053	5.52 ± 0.41
X371	0.122 ± 0.033	0.021 ± 0.023	0.033 ± 0.010	0.049 ± 0.022	0.055 ± 0.018	0.047 ± 0.021	0.69 ± 0.18
X372	0.134 ± 0.035	-0.006 ± 0.020	0.028 ± 0.011	0.084 ± 0.026	0.025 ± 0.016	0.097 ± 0.027	0.76 ± 0.20
X373	0.828 ± 0.172	0.472 ± 0.162	0.183 ± 0.048	0.185 ± 0.097	0.381 ± 0.091	0.253 ± 0.101	4.71 ± 0.98
X374	0.223 ± 0.055	0.095 ± 0.043	0.077 ± 0.019	0.017 ± 0.028	0.115 ± 0.030	0.051 ± 0.032	1.26 ± 0.31
X375	0.128 ± 0.064	0.258 ± 0.085	0.027 ± 0.017	-0.045 ± 0.026	0.150 ± 0.042	-0.050 ± 0.027	0.73 ± 0.36
X376	1.150 ± 0.170	0.537 ± 0.174	0.299 ± 0.049	0.190 ± 0.077	0.682 ± 0.099	0.222 ± 0.082	6.51 ± 0.96
X377	0.193 ± 0.038	0.006 ± 0.022	0.069 ± 0.014	0.061 ± 0.023	0.091 ± 0.022	0.077 ± 0.024	1.10 ± 0.22
X378	4.690 ± 0.151	1.460 ± 0.105	1.470 ± 0.062	1.000 ± 0.070	2.360 ± 0.094	1.470 ± 0.082	26.60 ± 0.86
X379	1.750 ± 0.109	0.923 ± 0.096	0.454 ± 0.040	0.304 ± 0.049	0.961 ± 0.069	0.467 ± 0.057	9.96 ± 0.62
X380	5.310 ± 0.185	1.830 ± 0.155	1.520 ± 0.068	0.959 ± 0.073	2.830 ± 0.119	1.330 ± 0.083	30.15 ± 1.05
X381	0.235 ± 0.041	0.040 ± 0.028	0.067 ± 0.014	0.083 ± 0.025	0.068 ± 0.020	0.132 ± 0.029	1.34 ± 0.23
X382	0.204 ± 0.049	0.101 ± 0.051	0.067 ± 0.017	0.006 ± 0.017	0.153 ± 0.034	0.016 ± 0.019	1.16 ± 0.28
X383	3.500 ± 0.481	0.598 ± 0.297	1.140 ± 0.183	0.641 ± 0.219	1.690 ± 0.285	1.080 ± 0.260	19.86 ± 2.74
X384	1.250 ± 0.082	0.144 ± 0.040	0.359 ± 0.031	0.469 ± 0.050	0.450 ± 0.043	0.604 ± 0.055	7.09 ± 0.47
X385	4.680 ± 0.372	1.760 ± 0.342	1.180 ± 0.112	0.984 ± 0.176	2.110 ± 0.200	1.510 ± 0.200	26.60 ± 2.11

Table 4—Continued

Object	F(0.35-8 keV)[a]	F(0.35-1.1 keV)[a]	F(1.1-2.6 keV)[a]	F(2.6-8 keV)[a]	F(0.5-2 keV)[a]	F(2-8 keV)[a]	L_X(0.35-8 keV)[b]
X386	29.500 ± 0.426	10.200 ± 0.329	7.710 ± 0.157	7.440 ± 0.203	13.900 ± 0.260	9.830 ± 0.228	167.21 ± 2.42
X387	0.594 ± 0.085	0.025 ± 0.048	0.148 ± 0.026	0.182 ± 0.043	0.164 ± 0.038	0.273 ± 0.050	3.37 ± 0.48
X388	0.356 ± 0.060	0.582 ± 0.103	0.037 ± 0.013	-0.002 ± 0.017	0.270 ± 0.043	0.012 ± 0.020	2.02 ± 0.34
X389	4.140 ± 0.157	4.380 ± 0.201	0.683 ± 0.047	0.035 ± 0.021	3.040 ± 0.118	0.100 ± 0.029	23.46 ± 0.89
X390	0.254 ± 0.053	0.121 ± 0.049	0.050 ± 0.015	0.075 ± 0.029	0.110 ± 0.029	0.086 ± 0.030	1.44 ± 0.30
X391	1.130 ± 0.089	1.040 ± 0.106	0.216 ± 0.028	0.041 ± 0.021	0.831 ± 0.067	0.064 ± 0.024	6.43 ± 0.51
X392	0.924 ± 0.139	0.280 ± 0.121	0.246 ± 0.042	0.205 ± 0.067	0.457 ± 0.075	0.250 ± 0.073	5.24 ± 0.79
X393	0.185 ± 0.042	0.161 ± 0.046	0.027 ± 0.011	0.034 ± 0.021	0.094 ± 0.024	0.037 ± 0.022	1.05 ± 0.24
X394	2.140 ± 0.234	0.315 ± 0.189	0.510 ± 0.068	0.617 ± 0.116	0.769 ± 0.115	0.842 ± 0.130	12.14 ± 1.33
X395	0.236 ± 0.045	-0.010 ± 0.020	0.058 ± 0.015	0.129 ± 0.032	0.060 ± 0.020	0.140 ± 0.032	1.34 ± 0.26
X396	0.140 ± 0.041	0.226 ± 0.052	-0.007 ± 0.007	0.018 ± 0.020	0.064 ± 0.022	0.004 ± 0.020	0.80 ± 0.23
X397	0.688 ± 0.074	0.231 ± 0.059	0.208 ± 0.027	0.118 ± 0.033	0.374 ± 0.046	0.160 ± 0.036	3.90 ± 0.42
X398	0.325 ± 0.064	0.195 ± 0.067	0.057 ± 0.018	0.079 ± 0.030	0.161 ± 0.037	0.082 ± 0.031	1.84 ± 0.36
X399	3.920 ± 0.606	1.720 ± 0.507	0.980 ± 0.222	0.865 ± 0.274	2.050 ± 0.387	1.090 ± 0.304	22.24 ± 3.45
X400	0.553 ± 0.074	0.002 ± 0.034	0.050 ± 0.015	0.320 ± 0.048	0.048 ± 0.022	0.360 ± 0.050	3.14 ± 0.42
X401	0.171 ± 0.054	0.028 ± 0.043	0.061 ± 0.017	0.023 ± 0.025	0.100 ± 0.030	0.040 ± 0.028	0.97 ± 0.31
X402	1.500 ± 0.098	0.138 ± 0.044	0.252 ± 0.029	0.883 ± 0.072	0.304 ± 0.040	0.975 ± 0.074	8.54 ± 0.56
X403	180.000 ± 1.650	114.000 ± 1.870	46.300 ± 0.576	20.100 ± 0.496	109.000 ± 1.150	31.500 ± 0.605	1023.52 ± 9.35
X404	2.150 ± 0.148	1.200 ± 0.153	0.549 ± 0.051	0.317 ± 0.055	1.210 ± 0.097	0.459 ± 0.064	12.21 ± 0.84
X405	0.132 ± 0.038	0.009 ± 0.024	0.009 ± 0.009	0.104 ± 0.030	0.003 ± 0.013	0.117 ± 0.031	0.75 ± 0.22
X406	0.581 ± 0.106	0.234 ± 0.099	0.098 ± 0.027	0.176 ± 0.055	0.184 ± 0.050	0.231 ± 0.060	3.29 ± 0.60
X407	0.798 ± 0.093	0.038 ± 0.050	0.086 ± 0.021	0.432 ± 0.057	0.117 ± 0.035	0.451 ± 0.058	4.53 ± 0.53
X408	0.258 ± 0.062	0.092 ± 0.050	0.067 ± 0.020	0.058 ± 0.034	0.120 ± 0.034	0.075 ± 0.036	1.46 ± 0.35
X409	0.474 ± 0.079	0.332 ± 0.081	0.087 ± 0.023	0.101 ± 0.040	0.296 ± 0.050	0.089 ± 0.040	2.69 ± 0.45
X410	3.890 ± 0.595	3.410 ± 0.695	0.734 ± 0.189	0.293 ± 0.176	2.210 ± 0.392	0.504 ± 0.218	22.07 ± 3.37
X411	6.480 ± 0.579	3.310 ± 0.571	1.560 ± 0.178	1.090 ± 0.261	3.670 ± 0.347	1.450 ± 0.287	36.74 ± 3.29
X412	1.140 ± 0.109	0.575 ± 0.100	0.268 ± 0.037	0.263 ± 0.054	0.602 ± 0.068	0.311 ± 0.057	6.49 ± 0.62
X413	0.302 ± 0.071	0.338 ± 0.085	0.043 ± 0.019	0.033 ± 0.033	0.166 ± 0.041	0.045 ± 0.035	1.71 ± 0.40
X414	11.800 ± 1.050	6.030 ± 0.950	3.110 ± 0.393	2.100 ± 0.435	6.230 ± 0.671	2.830 ± 0.496	66.88 ± 5.95
X415	1.210 ± 0.132	0.571 ± 0.130	0.283 ± 0.042	0.236 ± 0.055	0.584 ± 0.078	0.350 ± 0.065	6.89 ± 0.75
X416	0.371 ± 0.078	0.093 ± 0.060	0.090 ± 0.025	0.102 ± 0.037	0.140 ± 0.042	0.136 ± 0.042	2.11 ± 0.44
X417	3.310 ± 0.534	2.100 ± 0.533	0.689 ± 0.180	0.588 ± 0.216	1.770 ± 0.345	0.731 ± 0.240	18.80 ± 3.04
X418	0.299 ± 0.085	-0.034 ± 0.048	0.008 ± 0.016	0.216 ± 0.054	-0.026 ± 0.018	0.231 ± 0.058	1.70 ± 0.48
X419	8.000 ± 0.927	3.930 ± 0.814	2.430 ± 0.358	0.874 ± 0.357	5.070 ± 0.630	1.310 ± 0.403	45.35 ± 5.27
X420	6.790 ± 0.285	2.730 ± 0.267	1.710 ± 0.097	1.400 ± 0.114	3.340 ± 0.177	1.880 ± 0.131	38.51 ± 1.62

Table 4—Continued

Object	F(0.35-8 keV)[a]	F(0.35-1.1 keV)[a]	F(1.1-2.6 keV)[a]	F(2.6-8 keV)[a]	F(0.5-2 keV)[a]	F(2-8 keV)[a]	L_X(0.35-8 keV)[b]
X421	5.700 ± 0.892	2.370 ± 0.748	1.600 ± 0.316	0.909 ± 0.409	3.090 ± 0.543	1.370 ± 0.468	32.43 ± 5.07
X422	0.835 ± 0.133	0.545 ± 0.148	0.186 ± 0.036	0.145 ± 0.062	0.462 ± 0.073	0.185 ± 0.067	4.74 ± 0.75
X423	4.310 ± 0.646	5.620 ± 0.921	0.449 ± 0.155	-0.051 ± 0.007	3.080 ± 0.480	0.021 ± 0.085	24.42 ± 3.67
X424	10.200 ± 2.870	4.800 ± 2.550	1.970 ± 0.884	2.620 ± 1.440	5.360 ± 1.770	2.930 ± 1.510	58.02 ± 16.26
X425	2.130 ± 0.228	0.465 ± 0.199	0.511 ± 0.063	0.550 ± 0.113	0.951 ± 0.118	0.692 ± 0.122	12.11 ± 1.29
X426	2.280 ± 0.475	0.831 ± 0.362	0.847 ± 0.211	0.193 ± 0.147	1.210 ± 0.302	0.591 ± 0.237	12.92 ± 2.69
X427	1.780 ± 0.416	0.514 ± 0.288	0.783 ± 0.199	0.031 ± 0.082	1.170 ± 0.295	0.268 ± 0.163	10.11 ± 2.36
X428	3.800 ± 0.220	0.409 ± 0.116	0.968 ± 0.074	1.090 ± 0.101	1.390 ± 0.119	1.470 ± 0.116	21.53 ± 1.25
X429	0.760 ± 0.171	0.109 ± 0.146	0.163 ± 0.044	0.269 ± 0.093	0.209 ± 0.075	0.331 ± 0.100	4.31 ± 0.97
X430	0.666 ± 0.164	0.033 ± 0.074	0.195 ± 0.059	0.180 ± 0.076	0.246 ± 0.088	0.268 ± 0.090	3.77 ± 0.93
X431	1.710 ± 0.168	0.988 ± 0.189	0.474 ± 0.058	0.171 ± 0.052	1.100 ± 0.117	0.259 ± 0.061	9.70 ± 0.95
X432	6.860 ± 0.303	3.330 ± 0.323	1.680 ± 0.101	1.240 ± 0.111	3.430 ± 0.193	1.790 ± 0.131	39.02 ± 1.72
X433	2.150 ± 0.281	0.399 ± 0.186	0.113 ± 0.047	1.260 ± 0.181	0.190 ± 0.081	1.360 ± 0.188	12.21 ± 1.60
X434	1.720 ± 0.253	1.730 ± 0.312	0.342 ± 0.065	0.174 ± 0.116	1.090 ± 0.140	0.281 ± 0.127	9.78 ± 1.44
X435	0.552 ± 0.112	0.206 ± 0.100	0.188 ± 0.036	0.037 ± 0.049	0.356 ± 0.066	0.089 ± 0.055	3.14 ± 0.64
X436	1.740 ± 0.230	0.163 ± 0.159	0.451 ± 0.067	0.509 ± 0.122	0.548 ± 0.104	0.779 ± 0.138	9.86 ± 1.31
X437	22.600 ± 1.470	13.100 ± 1.420	5.790 ± 0.540	3.000 ± 0.540	12.700 ± 0.967	5.170 ± 0.684	128.45 ± 8.36
X438	29.200 ± 0.703	10.100 ± 0.620	7.440 ± 0.234	6.250 ± 0.296	14.000 ± 0.425	8.570 ± 0.337	165.69 ± 3.98
X439	1.950 ± 0.222	0.684 ± 0.193	0.469 ± 0.064	0.443 ± 0.111	0.943 ± 0.118	0.545 ± 0.120	11.10 ± 1.26
X440	7.160 ± 0.626	2.630 ± 0.598	1.600 ± 0.199	1.740 ± 0.259	3.270 ± 0.383	2.110 ± 0.282	40.54 ± 3.55
X441	1.730 ± 0.266	1.280 ± 0.339	0.329 ± 0.078	0.331 ± 0.103	0.849 ± 0.165	0.472 ± 0.121	9.80 ± 1.51
X442	2.980 ± 0.240	1.930 ± 0.315	0.446 ± 0.061	0.802 ± 0.102	1.320 ± 0.144	0.905 ± 0.108	16.92 ± 1.36
X443	4.590 ± 0.799	3.240 ± 0.833	0.968 ± 0.269	0.710 ± 0.315	2.620 ± 0.527	0.679 ± 0.312	26.09 ± 4.53
X444	9.330 ± 1.070	4.630 ± 0.949	2.180 ± 0.378	2.220 ± 0.514	4.660 ± 0.663	2.670 ± 0.558	52.95 ± 6.08
X445	2.630 ± 0.604	0.581 ± 0.406	0.434 ± 0.179	1.350 ± 0.404	0.821 ± 0.300	1.390 ± 0.414	14.92 ± 3.42
X446	2.030 ± 0.464	1.300 ± 0.455	0.509 ± 0.165	0.261 ± 0.187	1.190 ± 0.303	0.315 ± 0.202	11.55 ± 2.63
X447	0.535 ± 0.122	0.098 ± 0.107	0.094 ± 0.031	0.195 ± 0.062	0.186 ± 0.061	0.216 ± 0.065	3.04 ± 0.69
X448	3.910 ± 0.482	0.861 ± 0.368	1.180 ± 0.174	0.624 ± 0.168	1.920 ± 0.303	1.000 ± 0.206	22.19 ± 2.74
X449	17.400 ± 0.503	9.180 ± 0.549	4.180 ± 0.166	3.020 ± 0.184	9.290 ± 0.328	4.060 ± 0.210	98.55 ± 2.86
X450	18.800 ± 0.567	9.990 ± 0.591	4.770 ± 0.185	2.910 ± 0.225	10.300 ± 0.356	4.200 ± 0.257	106.66 ± 3.22
X451	1.480 ± 0.444	-0.139 ± 0.167	0.599 ± 0.185	0.377 ± 0.223	0.350 ± 0.203	0.841 ± 0.301	8.39 ± 2.52
X452	0.929 ± 0.185	0.210 ± 0.159	0.211 ± 0.052	0.260 ± 0.088	0.289 ± 0.088	0.395 ± 0.100	5.27 ± 1.05
X453	22.100 ± 2.450	12.500 ± 3.350	5.250 ± 0.771	3.520 ± 0.787	12.300 ± 1.690	4.650 ± 0.891	125.41 ± 13.93
X454	2.480 ± 0.633	0.982 ± 0.493	0.652 ± 0.206	0.629 ± 0.373	1.100 ± 0.334	1.040 ± 0.426	14.06 ± 3.60
X455	1.470 ± 0.497	1.680 ± 0.557	0.105 ± 0.109	0.198 ± 0.267	0.548 ± 0.230	0.199 ± 0.278	8.34 ± 2.81

Table 4—Continued

Object	F(0.35-8 keV)[a]	F(0.35-1.1 keV)[a]	F(1.1-2.6 keV)[a]	F(2.6-8 keV)[a]	F(0.5-2 keV)[a]	F(2-8 keV)[a]	L_X(0.35-8 keV)[b]
X456	2.730 ± 0.649	1.170 ± 0.528	0.684 ± 0.216	0.686 ± 0.362	1.270 ± 0.366	0.933 ± 0.399	15.50 ± 3.67
X457	7.490 ± 0.950	2.270 ± 0.710	2.290 ± 0.364	1.450 ± 0.421	3.840 ± 0.583	2.050 ± 0.484	42.56 ± 5.40
X458	16.200 ± 1.340	7.430 ± 1.150	3.730 ± 0.459	4.070 ± 0.665	7.630 ± 0.795	4.950 ± 0.725	91.96 ± 7.58

[a]Fluxes are in units of 10^{-6} photons cm^{-2}s^{-1}.

[b]0.35-8 keV X-ray luminosities are in units of 10^{36} ergs s^{-1} and are calculated from the energy flux in the 0.35-8.0 kev band. The errors are purely statistical.

Table 5.   M83 X-ray Point Source IDs and Comments[a]

Object	Other X-ray[b]	Radio ID[c]	SNR/SNe[d]	P/T[e]	Var.[f]	Type[g]	Notes[h]
X001						AGN	
X002				P		AGN	Bright power law source outside D25 contour
X003	D13-030:					AGN?	
X005	D13-033			P		AGN	Bright power law source outside D25 countour; blueish optical point source
X006	D13-040:					AGN?	
X007	D13-041:						
X009	D13-046:				AN		
X010	D13-048				V	AGN?	
X011						AGN?	
X012					V		
X014	D13-049:						
X017	D13-053:			P		AGN	Bright power law source outside D25 contour
X019	S03-001	A002	B12-003			SNR	
X020		A003:					
X021	S03-002			P	V		
X022	S03-003			P	A		
X027					V		
X029	S03-005; D13-060			P	V	XRB	Bright XRB
X031	D13-061				C		
X035						Star	Foreground star (2MASS)
X036	D13-064:					AGN?	
X038	D13-065			P		AGN	AGN (z=0.078), bright 2MASS galaxy
X039					N		
X040	D13-066:					AGN?	
X044	S03-006		D10-307:	P		AGN	AGN based on GMOS optical spectrum
X046	S03-007		B12-023			SNR	
X048					V		
X049	S03-008; D13-069			P/T	N		
X051	S03-009						
X053	S03-010		B12-036			SNR	
X054			D10-309		B		
X055					V		
X056					V*		
X057			B12-037			SNR	

Table 5—Continued

Object	Other X-ray[b]	Radio ID[c]	SNR/SNe[d]	P/T[e]	Var.[f]	Type[g]	Notes[h]
X060						AGN?	
X061			B12-041			SNR	
X063	S03-011	A012; M06-03:	B12-045			SNR	
X064			B12-047		V*	SNR?	Soft source coincident with SNR, but may be variable
X065	S03-012	A013	B12-048			SNR	
X067	S03-013:	A015; M06-04				SNR	
X070						AGN/GAL	Near galaxy
X072					B		
X073	S03-014; D13-073			P	V		
X075					V		
X078		A018				SNR	
X081						AGN/GAL	
X085				P	A		
X087					V		
X088	D13-074:						
X093			B12-060			SNR	
X095		A021; M06-08				SNR	
X097	S03-015	A020; M06-07				SNR	
X098		A022; M06-09					
X099				D	B		
X100			B12-063:			SNR	
X103	S03-016						
X104		A026; M06-12				SNR	
X105	S03-017		B12-065			SNR	
X106			B12-067			SNR	
X107	S03-018		B12-066			SNR	
X110	S03-019; D13-076:		D10-312		V*	SNR	
X111				D	C		
X116	S03-020; D13-077:	A031:; A032	B12-073			SNR	
X117	S03-021			P	V		
X118	S03-023				V*		
X119	S03-022		B12-074			SNR	
X121			B12-075			SNR	
X124			B12-079				
X127			B12-082			SNR	

Table 5—Continued

Object	Other X-ray[b]	Radio ID[c]	SNR/SNe[d]	P/T[e]	Var.[f]	Type[g]	Notes[h]
X128			B12-084			SNR	
X129	S03-025	A037; M06-20	B12-087			SNR	
X131	S03-024		B12-089			SNR	
X133		A036:; A038:; M06-19:					
X134			B12-090			SNR	
X135	S03-026		D10-314:		AN		
X136			B12-093			SNR	
X137			B12-095:				
X138	S03-027; D13-079			P	V	XRB	Bright source with featureless spectrum
X139	S03-028	A039:; M06-22	B12-096:; B12-098		V		Coincident with SNR, but hard X-ray spectrum and variability make SNR ID unlikely
X141	S03-029	A043; M06-24	B12-106			SNR	
X143	S03-030:	A044					
X145	S03-031; D13-080			P/D	V	XRB	Bright XRB in spiral arm
X147	S03-032						
X148					V*		
X149			B12-109			SNR	
X152	S03-033; D13-081			P/D	V	XRB	
X155	S03-034; D13-082:			P	V	AGN/XRB?	Bright power law source outside galaxy disk; faint I-band source
X159	S03-035		B12-115	T		SNR	
X160	S03-036				V*		
X161	S03-037						
X162	S03-038				A	SS	Very soft variable X-ray source, likely SS source
X163	S03-040:; D13-084			P			
X165	S03-039; D13-083:	A050; M06-28		P		AGN/GAL	
X166			B12-117			SNR	
X167					V		
X168				D	B	XRB	Bright source, not detected in archival data
X169		A051				SNR	
X171	D13-085			P		AGN/XRB?	Bright power law source outsde main galaxy disk but no optical counterpart
X172	S03-041		B12-118; D10-01			SNR	
X178	S03-042						
X179		A055					
X181			D10-03			SNR	

Table 5—Continued

Object	Other X-ray[b]	Radio ID[c]	SNR/SNe[d]	P/T[e]	Var.[f]	Type[g]	Notes[h]
X182					V		
X183	S03-043		B12-122			SNR	
X184		A056	B12-123			SNR	
X185	S03-044; D13-087			P+D	V	XRB	Bright source in spiral arm
X186	S03-045	A057	B12-124; D10-04			SNR	
X187	S03-046; D13-088			P	V		
X193	S03-047			D	V	XRB	Bright source with complex spectrum in nucleus
X195	S03-048		B12-127			SNR	
X197					V*		
X198	S03-049			P		XRB	
X199	S03-051		B12-129			SNR	
X201	S03-050						
X202			D10-N01			SNR	
X203	S03-052			P			
X204				T			Bright thermal source in nucleus
X205			B12-131			SNR	
X206				P	N		Bright power law source in nucleus
X207	S03-053		D10-N03	T	V*	SNR	Bright thermal source in nucleus
X212	S03-054		D10-N04	T		SNR	Bright thermal source in nucleus
X213				T	V		
X215			B12-133			SNR	
X216	S03-056; D13-090:		SN1968L	T	V		Thermal source which aligns with SN1968L but association unlikely
X217	S03-055; D13-091:				V		
X219		A060					
X220	S03-057			T	V		Thermal X-ray spectrum in nuclues, but probably not SNR
X223	S03-059:		D10-N08; D10-N10	T	V*		Thermal X-ray spectrum in nuclues, but probably not SNR
X224				T	V		
X225	S03-058			P			Bright power law source in nucleus
X227	S03-060; D13-092:			P/D	V	XRB	Bright source in spiral arm
X228	S03-062			P	V	XRB	Bright hard source in nucleus
X229			D10-N12	T	V		
X230	S03-061			T			Bright thermal source in nucleus
X231			D10-N11	T			Soft source with thermal spectrum in nucleus
X232	D13-093:			T	V		
X233	S03-063		D10-N15	P	V	NUC	Bright powerlaw source; Optical/IR nucleus

Table 5—Continued

Object	Other X-ray[b]	Radio ID[c]	SNR/SNe[d]	P/T[e]	Var.[f]	Type[g]	Notes[h]
X234	S03-064			P	V	XRB	Bright powerlaw south of Optical/IR nucleus
X235	S03-066		B12-137; D10-09			SNR	
X236	S03-065; D13-095:			P/D	V	XRB	Bright source in star forming region
X237	S03-067	A062	D10-N16	D	V		Bright diskBB source near nucleus; new microquasar
X239				T	V		
X240	S03-068				AN	SS	Supersoft source idenfified by Soria & Wu (2003)
X241			D10-N17	T	V	SNR?	Bright thermal source in nucleus
X242	S03-069			P	V		
X243	S03-070		D10-321	T		SNR	Bright thermal source in nucleus
X244	S03-071			P			
X245		A063:					
X248	S03-072; D13-097:			D	V	XRB	Bright source in interarm region
X249			B12-141			SNR	
X250	S03-074		D10-N19			SNR	
X251	S03-073; D13-099:			D	V	XRB	Highly variable, bright XRB
X252	S03-075; D13-098:			P	V	XRB/AGN?	Bright source at outer edge of stellar disk; no optical source
X253	S03-076		B12-142			SNR	
X255			B12-144			SNR	
X256	S03-077		B12-143; D10-12			SNR	
X258	S03-078; D13-100			D	V	XRB	Bright source
X259	S03-079						
X261	S03-080	A066	B12-147			SNR	
X262			B12-148			SNR	
X263	D13-102:					AGN?	
X265	S03-081	A067; M06-35	B12-150; D10-15	T		SNR	
X267	S03-082			P	V		
X268						AGN/GAL	Galaxy/AGN
X269					V		
X271	D13-104:						
X272	S03-083	A070	B12-151			SNR	
X273					A		
X274	S03-084	A071; M06-36		P	V		
X275		A072; M06-38				SNR	
X279		A073; M06-39	D10-324; SN1957D			SNR	
X280					V*		

Table 5—Continued

Object	Other X-ray[b]	Radio ID[c]	SNR/SNe[d]	P/T[e]	Var.[f]	Type[g]	Notes[h]
X281	S03-085; D13-106			P/D	V	XRB	Persistent, bright source
X284	S03-086; D13-107			D	BN	XRB	Bright source, with relatively soft spectrum
X285	S03-087			P	V*		
X286	S03-088; D13-108			D	V	XRB	
X287	S03-089	A075	B12-156			SNR	
X288			B12-159			SNR	
X289	S03-090				V*		
X290	S03-091				AN		
X292			B12-160:			SNR	
X294		A077; M06-40:					
X295	S03-092			P			
X299				P+D	A	XRB	ULX, see Soria & Wu (2003)
X301					V		
X303	S03-093			P/T	V		
X304					V*		
X305	D13-110						
X309	S03-094						
X310	S03-095		B12-169		V	SNR	
X311	S03-097		B12-170			SNR	
X312	S03-096				A	SS	Supersoft source idenfified by Soria & Wu (2003)
X313			B12-171; D10-19			SNR	
X314					V		
X315	S03-099				V		
X316	S03-100	A080; M06-41	B12-174			SNR	
X317	S03-101						
X318		A082:; M06-42:					
X319			B12-177			SNR	
X320	S03-102		B12-178			SNR	
X321	S03-104; D13-114:		B12-179	D	V	XRB	Likely BH XRB, despite positional coincidence with B112-179
X322	S03-103						
X324	D13-115:						
X326	S03-105; D13-116:	A084	B12-180; D10-22			SNR	
X327	S03-106						
X330		A089	B12-186			SNR	
X332	S03-107						

Table 5—Continued

Object	Other X-ray[b]	Radio ID[c]	SNR/SNe[d]	P/T[e]	Var.[f]	Type[g]	Notes[h]
X333		A090:; M06-49:					
X334						Star	Foreground star (2MASS 13370837-2943235)
X335	S03-108:						
X336			D10-26			SNR	
X338			B12-190; D10-27			SNR	
X339	S03-109		B12-191; D10-28			SNR	
X341			D10-333; D10-29			SNR	
X342		A094	B12-193; D10-32			SNR	
X348		A095; M06-52	B12-195; D10-34			SNR	
X350		A098:; M06-54	B12-197; D10-36			SNR	
X352			B12-199; D10-37			SNR	
X353			B12-203			SNR	
X354		A100; M06-55:					
X355			B12-207			SNR	
X356			B12-206			SNR	
X357						Star	Foreground star (2MASS 13371181-2948335)
X358	S03-110		B12-209			SNR	
X360	S03-111		D10-336			SNR	
X363	S03-112						
X364			B12-210			SNR	
X365					C		
X366	S03-113; D13-120:			P	V		
X367	D13-122:					AGN?	
X368	S03-115		B12-211			SNR	
X369	D13-124					AGN?	
X370	S03-116						
X373					V		
X376						AGN?	
X377					V		
X378	S03-117			P	V		
X379	S03-118				V		
X380	S03-119; D13-125:			P	V		
X383	D13-127:						
X384	S03-120						
X386	S03-121; D13-129:			P+D	V	XRB?	Possible Bright XRB outside main disk, based on spectrum; no

Table 5—Continued

Object	Other X-ray[b]	Radio ID[c]	SNR/SNe[d]	P/T[e]	Var.[f]	Type[g]	Notes[h]
							optical source
X388						Star	Foreground star (2MASS 13371700-2948153)
X389	S03-122; D13-130	A103	B12-221	T		SNR	
X391	S03-123	A104	B12-223			SNR	
X393	S03-124				A	SS	Variable source with very soft spectrum, most likely a SS source
X394						AGN?	
X397	S03-125						
X399	D13-131					AGN?	
X400						AGN/GAL	
X402	S03-126				V	AGN/GAL	Galaxy/AGN
X403	D13-133			P+D	V	XRB?	Bright source that is most likely XRB (See appendix); adjacent to background galaxy
X404						AGN?	
X405						AGN/GAL	Galaxy/AGN
X412	S03-127					AGN/GAL	Galaxy/AGN
X414	D13-137					AGN?	
X416						AGN/GAL	
X417	D13-139:						
X419	D13-140:					AGN?	
X420	D13-141			P/D		AGN?	Bright power law/diskBB source outside D25 countours of galaxy
X421	D13-142:					AGN?	
X422						AGN?	
X423	D13-143					Star	Foreground star (2MASS 13372725-2955475)
X424	D13-144:					AGN/GAL	Galaxy; 2MASS source
X425						AGN?	
X427	D13-146:						
X428	D13-147:						
X430						AGN?	
X431	D13-148:	A108:				AGN/GAL	Galaxy visible in Magellan optical images
X432	D13-149:			P		AGN	Bright power law source outside D25 countours of the galaxy
X433						AGN?	
X434						Star	Foreground star (2MASS 13373013-2941568)
X435	D13-152:						
X436						AGN?	
X437	D13-153					AGN?	

Table 5—Continued

Object	Other X-ray[b]	Radio ID[c]	SNR/SNe[d]	P/T[e]	Var.[f]	Type[g]	Notes[h]
X438	D13-154:			P		AGN	Bright power law source outside bright disk of the galaxy
X440	D13-155					AGN?	
X441		A109:				AGN?	Galaxy visible in Magellan images
X442	D13-158:					AGN/GAL	
X443	D13-160:					AGN?	
X444	D13-161					AGN?	
X445	D13-162:					AGN/GAL	
X446						AGN?	
X448						AGN?	
X449	D13-164			P		AGN	Bright power law source outside D25 contours with bluish stellar counterpart
X450	D13-166:			P		AGN/XRB?	Bright power law source outside bright disk
X451						AGN?	
X453	D13-170:						
X456						AGN/GAL	
X457						AGN?	
X458	D13-177:					Star	Foreground star; 2MASS

[a]A source in a pre-existing catalog is assumed to be coincident if it is within 2 arcsec of an X-ray source. If the difference in position of the X-ray source and the catalogued source is between 1 and 2 arcsec, this is indicated with a ":"

[b]Coincidences with the earlier X-ray survey of Soria & Wu (2003) and Ducci et al. (2013).

[c]Coincidences with the radio survey of Maddox et al. (2006) and our new radio survey conducted with ATCA.

[d]Coincidencs with optical SNRs identified by Blair et al. (2012) and Dopita et al. (2010). Only nebulae with high [S II]:Hα ratios are included.

[e]For sources brighter than 500 counts, the source spectra are characterized as having non-thermal (P) or thermal (T). See text. There are a few sources, labelled P/T for which no clear distinction could be made.

[f]Variability flags: C implies "Clasical X-ray trasient, B implies source with large variations from observation to observation. A source with 'N' in the classification implies that the sources is seen above the background all of the time. 'A' is the designation for sources that were either "on" in the archival observations and "off" in the new data, or vice versa. 'V' refers to sources that are simply variable, while 'V*' indicates the object was variable, but the variability was not detected in the T band. See text.

[g]Our attempt to classify X-ray sources in M83. Sources classifications we regard as more tentative are followed by a '?'.

[h]Brief comments on the sources. More extensive commentary on a number of the sources can be found in the text and for the X-ray bright sources in the Appendix.

Table 6.   Census of Identifications[a]

Object List	Comparison List	Number in Comparison List	Number IDs	Notes
ATCA	VLA[b]	55	47	
ATCA	X-ray	458	46	
ATCA	[SII]-SNRs[c]	225	21	
X-ray	Soria & Wu (2003)	127	124	
X-ray	XMM[d]	46	40	Within D25
X-ray	[SII]-SNRs[c]	225	73	
SNE	ATCA	5	3	
SNRs	ATCA	109	28	
SNe	X-ray	5	1	
SNRs	X-ray	458	87	
Stars	X-ray	458	6	
AGN/Background	X-ray	458	56	

[a]See text for details, as some sources are chance coincidences

[b]Maddox et al. (2006)

[c]Blair et al. (2012)

[d]Ducci et al. (2013)

Table 7. Source Counts in the Various Regions

Region	Definition	Limit[a]	Sources[b]	AGN	SNR	Star	XRB
		0.35-8.0 keV					
Bulge	$r < 0\rlap{.}'6$	6.4	53	0.8	7	0	45.2
Nuclear Region[c]	$r < 0\rlap{.}'3$	6.4	38	0.2	6	0	31.8
Outer Bulge	$0\rlap{.}'3 < r < 0\rlap{.}'6$	6.4	15	0.7	1	0	13.3
All Disk	$r > 0\rlap{.}'6 \text{ and } R_{proj} < 6\rlap{.}'5$	8.0	265	96.3	69	1	98.7
Inner Disk	$r > 0\rlap{.}'6 \text{ and } R_{proj} < 3\rlap{.}'5$	6.4	185	34.0	60	0	91.0
Arm		6.4	84	9.8	37	0	37.2
Inter-Arm		6.4	101	24.3	23	0	53.7
Outer Disk	$3\rlap{.}'5 < R_{proj} < 6\rlap{.}'5$	10.0	89	63.0	11	1	14.0
		0.5-2.0 keV					
Bulge	$r < 0\rlap{.}'6$	2.5	52	0.6	7	0	44.4
Nuclear Region[c]	$r < 0\rlap{.}'3$	2.5	37	0.1	6	0	30.9
Outer Bulge	$0\rlap{.}'3 < r < 0\rlap{.}'6$	2.5	15	0.4	1	0	13.6
All Disk	$r > 0\rlap{.}'6 \text{ and } R_{proj} < 6\rlap{.}'5$	2.5	262	70.6	75	1	115.4
Inner Disk	$r > 0\rlap{.}'6 \text{ and } R_{proj} < 3\rlap{.}'5$	2.5	187	22.4	64	0	100.6
Arm		2.5	95	6.5	41	0	47.6
Inter-Arm		2.5	92	15.9	23	0	53.1
Outer Disk	$3\rlap{.}'5 < R_{proj} < 6\rlap{.}'5$	3.2	75	47.8	11	1	15.2
		2.0-8.0 keV					
Bulge	$r < 0\rlap{.}'6$	12.7	26	0.7	2	0	23.3
Nuclear Region[c]	$r < 0\rlap{.}'3$	10.1	22	0.2	2	0	19.8
Outer Bulge	$0\rlap{.}'3 < r < 0\rlap{.}'6$	12.7	4	0.6	0	0	3.4
All Disk	$r > 0\rlap{.}'6 \text{ and } R_{proj} < 6\rlap{.}'5$	16.0	115	52.2	3	0	59.8
Inner Disk	$r > 0\rlap{.}'6 \text{ and } R_{proj} < 3\rlap{.}'5$	12.7	71	20.9	3	0	47.1
Arm		12.7	21	6.4	3	0	11.6
Inter-Arm		16.0	46	14.2	0	0	31.8
Outer Disk	$3\rlap{.}'5 < R_{proj} < 6\rlap{.}'5$	25.4	45	30.9	0	1	14.0

[a] Limiting sensitivity in units of 10^{35} ergs s^{-1} for each region. The sensitivity of our observations vary from position to position in M83, and from region to region. The sensitivity limit for a region is the limit at which the completeness correction from observed source counts to actual source counts

is 10%, that is the luminosity where 90% of the area of a region has that sensitivity or better.

[b] Source counts here are for sources which were detected in a particular band above the sensitivity limit for that band. Since the limiting sensitivity varies from region to region, the number of sources do not always sum up. The clearest case of this is in the 0.2-8 keV band where there are 67 sources in the sum of the inter-arm and arm regions, but 71 in the inner disk.

[c] The nuclear region described in Section 7 includes both the nuclear starburst and a population of older stars.
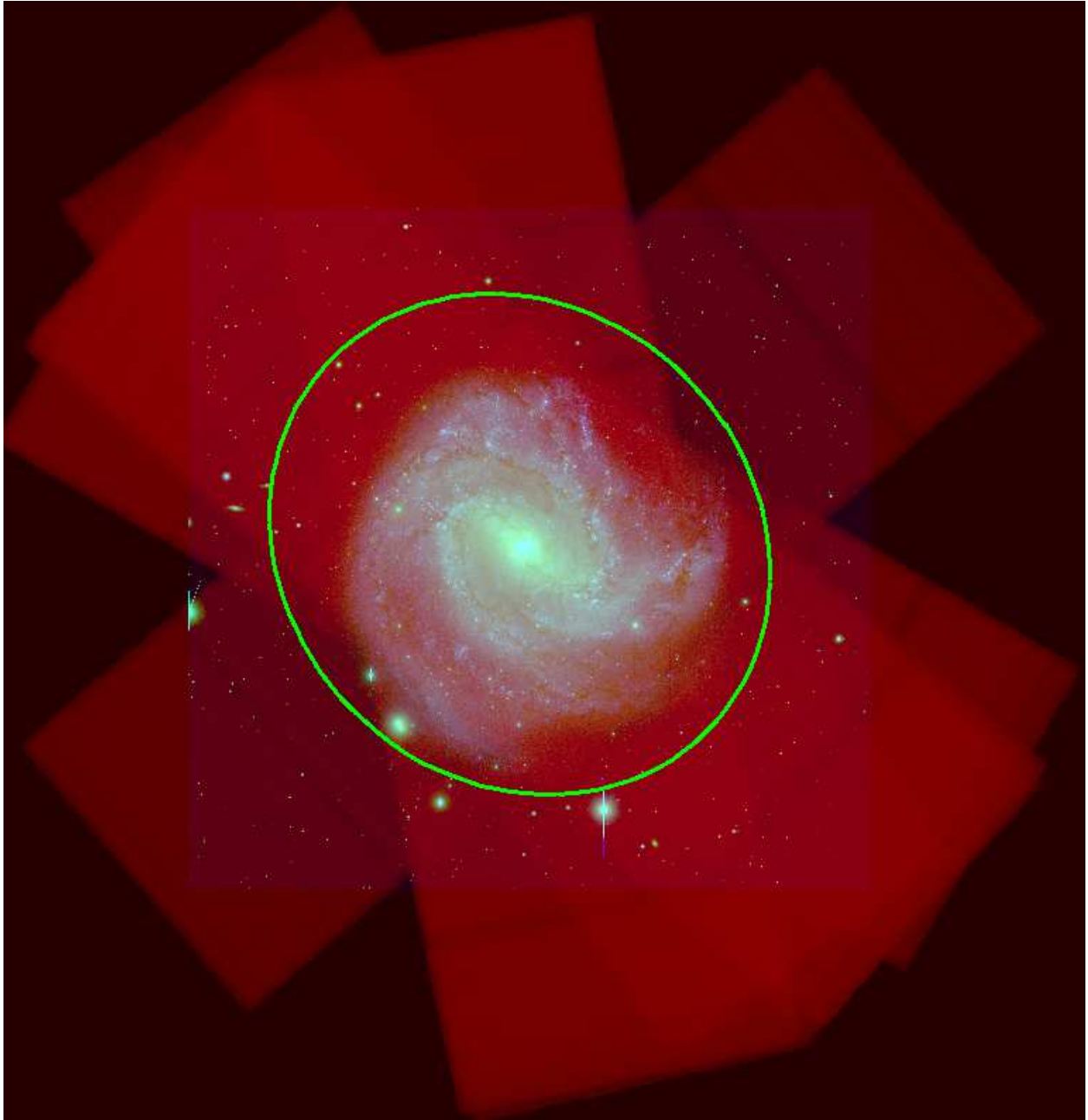
Fig. 1.— An exposure map created for the S2, S3, and S4 chips for all of the *Chandra* observations of M83, superposed on an optical image of M83. The D$_{25}$ size of M83 is shown in green. Though most of the inner portions of M83 are well covered by our observations, regions to the NW and SE have somewhat lower coverage than elsewhere.
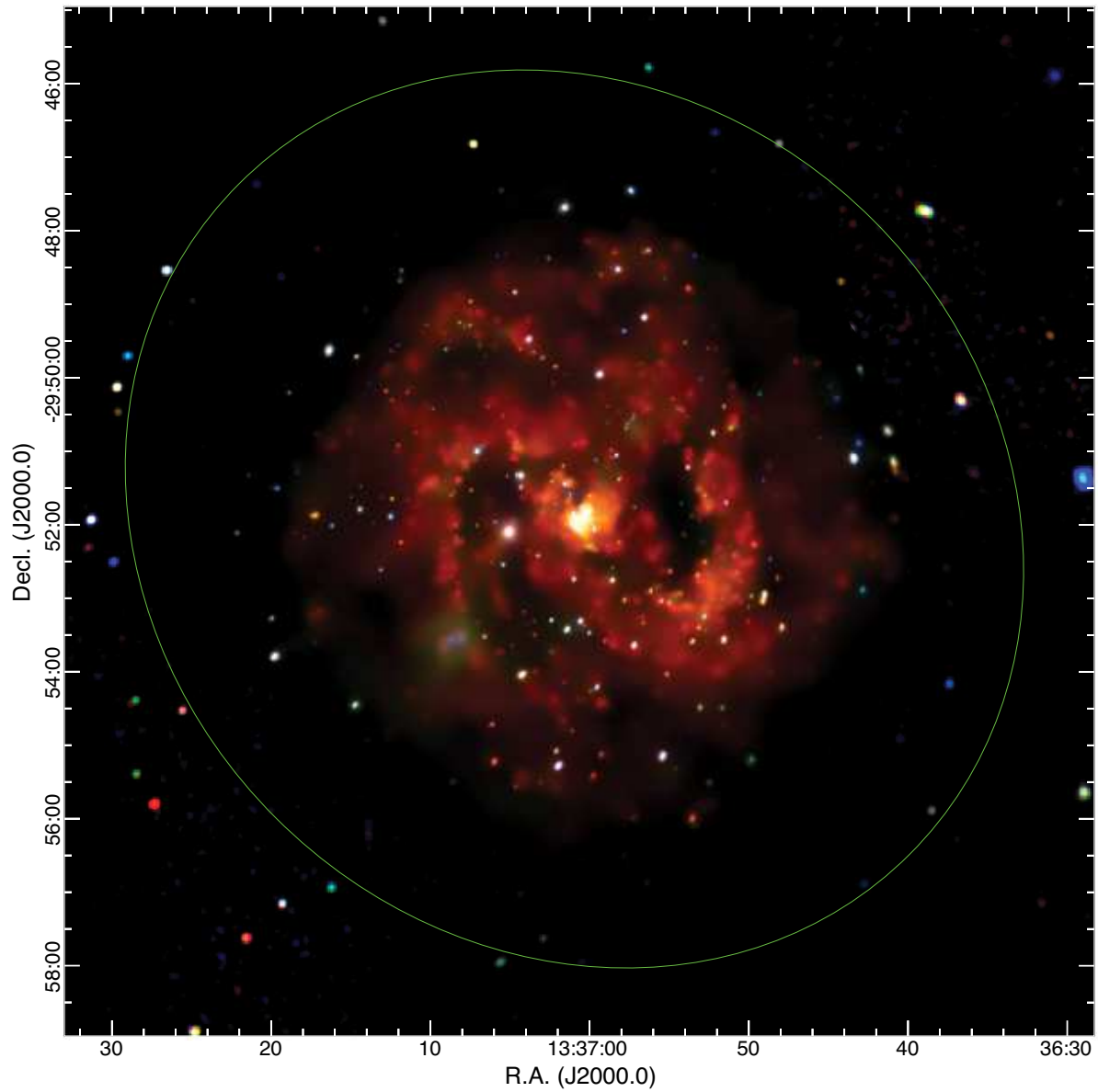
Fig. 2.— The inner portion of combined X-ray image obtained from the 2010-2011 *Chandra* observations of M83. Photons from 0.35-1.1 keV, 1.1-2.6 keV, and 2.6-8 keV are shown in red, green, and blue, respectively. The D$_{25}$ ellipse of M83 is shown in green. Soft diffuse X-ray emission traces the spiral arms of the galaxy. The new ultraluminous X-ray source described by Soria et al. (2012) is in the inter-arm region about 1′ east of the nucleus.
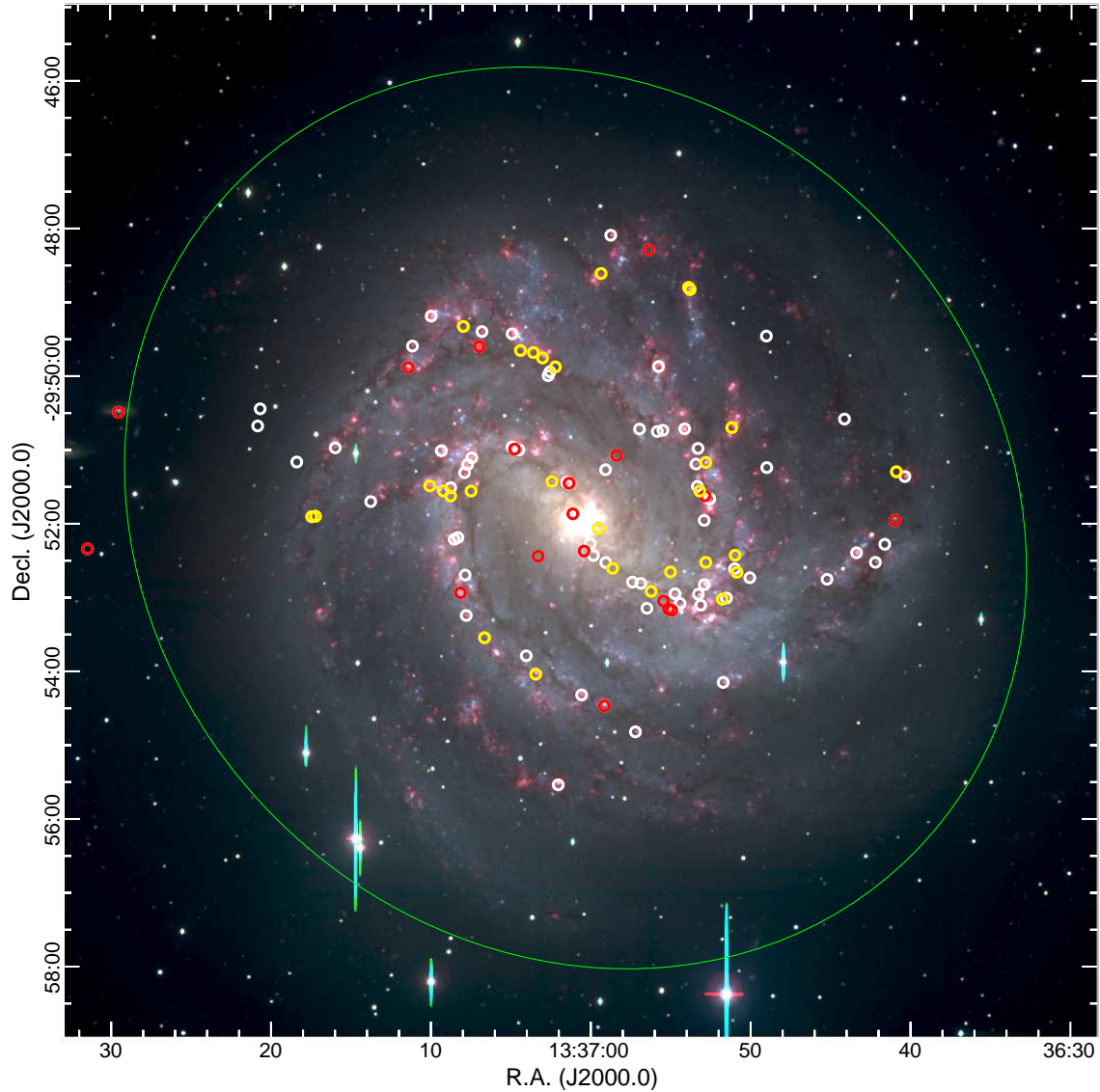
Fig. 3.— Radio sources detected in our ATCA survey of M83 are plotted on a 3 color image of M83. Here Hα emission is shown in red, V band in green, and the B band in blue, all from our Magellan survey (Blair et al. 2012). The field is identical with that shown in Figures 2 and 4, and the D$_{25}$ ellipse is again shown in green. Radio sources coincident with *Chandra* X-ray sources are shown in red, ones coincident with SNRs from Blair et al. (2012) are shown in yellow, and the remaining sources in white. Most of the sources of all types lie along the spiral arms of the galaxy. The two radio sources outside the D$_{25}$ contour of the galaxy are AGN.
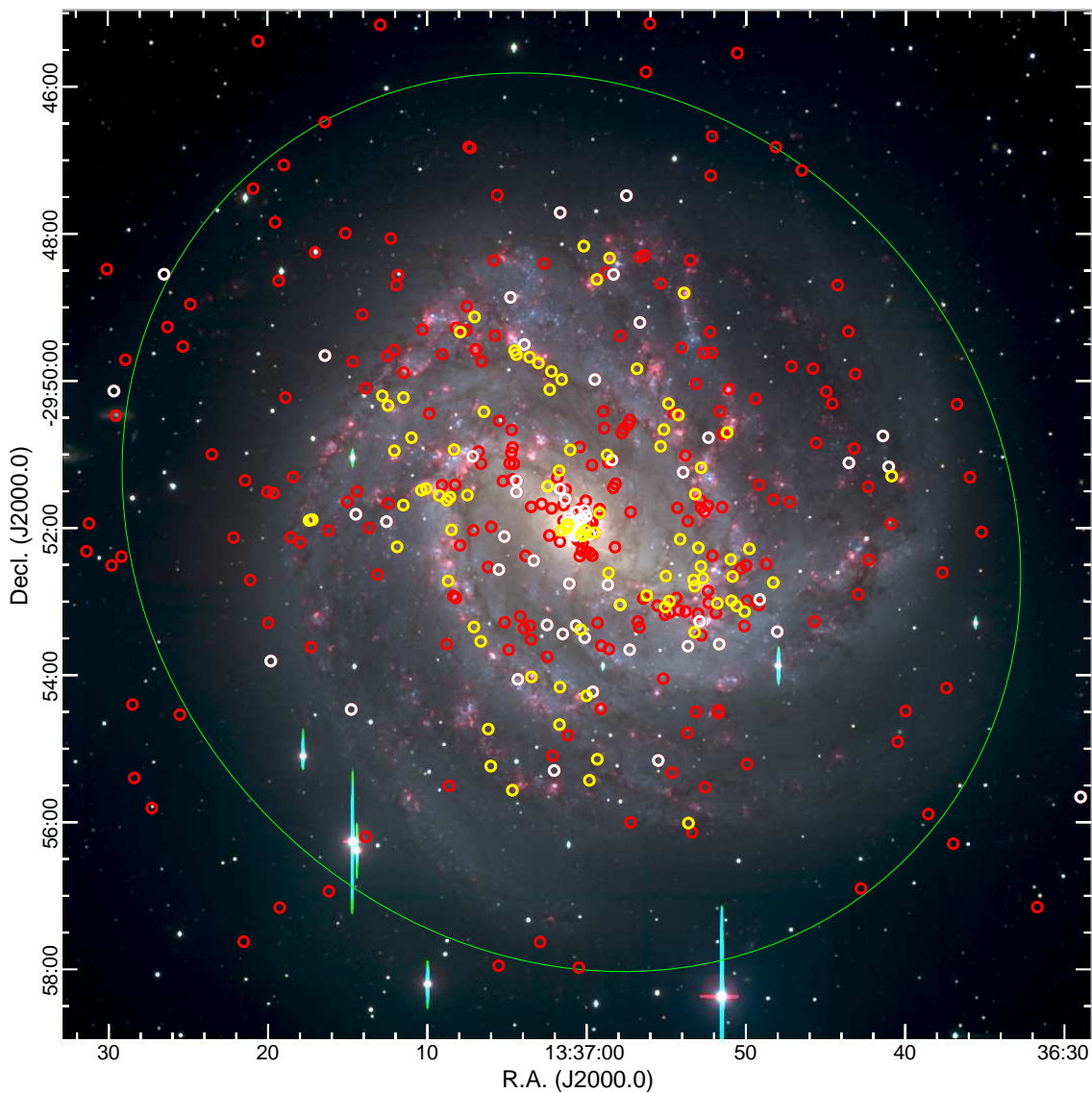
Fig. 4.— X-ray sources detected in our *Chandra* survey of M83 are plotted on the same 3-color optical image as shown in Figure 3. The field is identical for Figures 2, 3 and 4. The D_{25} ellipse is again shown in green. Sources identified as SNRs are identified in yellow, the brighter sources (those with > 500 counts in our survey) are in white, and fainter sources in red. Most of the sources outside of this boundary are foreground or background objects, mainly AGN.
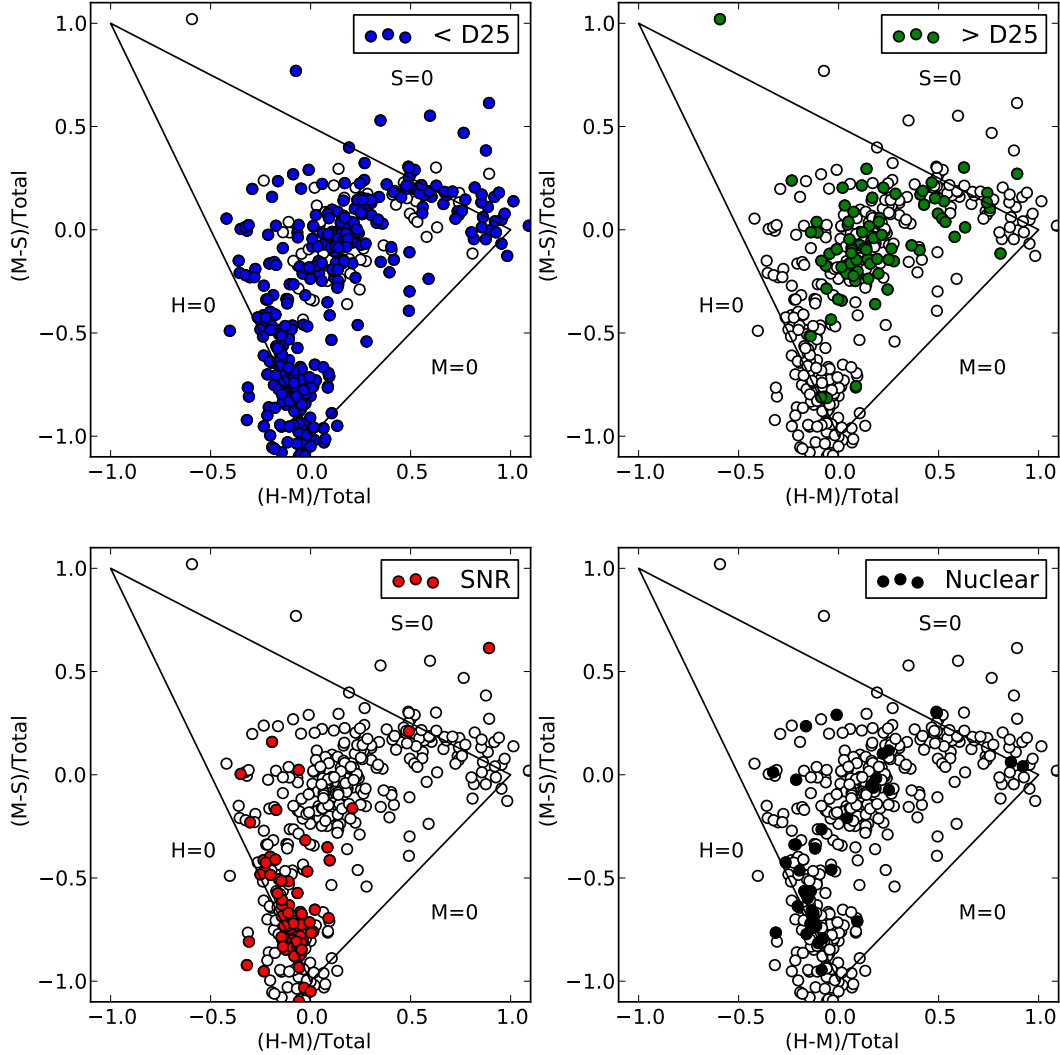
Fig. 5.— A hardness-ratio plot of the sources detected in M83, with different subsets high-lighted in the different panels. Hardness ratios of individual sources are listed in Table 3. The soft (S), medium (M) and hard (H) bands correspond to energies of 0.35-1.1 keV, 1.1-2.6 keV and 2.6-8 keV, respectively. As a result of counting statistics, some sources have ratios that fall outside of the triangular region where all sources should lie. Sources shown in blue (upper left panel) denote ones within the D_{25} ellipse, while those in green (upper right) de-note ones outside D_{25}. Sources shown in red (lower left) coincide in position with SNRs and SNR candidates reported by Blair et al. (2012). The black filled circles (lower right) denote sources in the nuclear region, within 0.5 kpc of M83's center. Some of these nuclear-region sources are relatively hard, typical of X-ray binaries, while others are quite soft, consistent with what one might expect from SNRs.
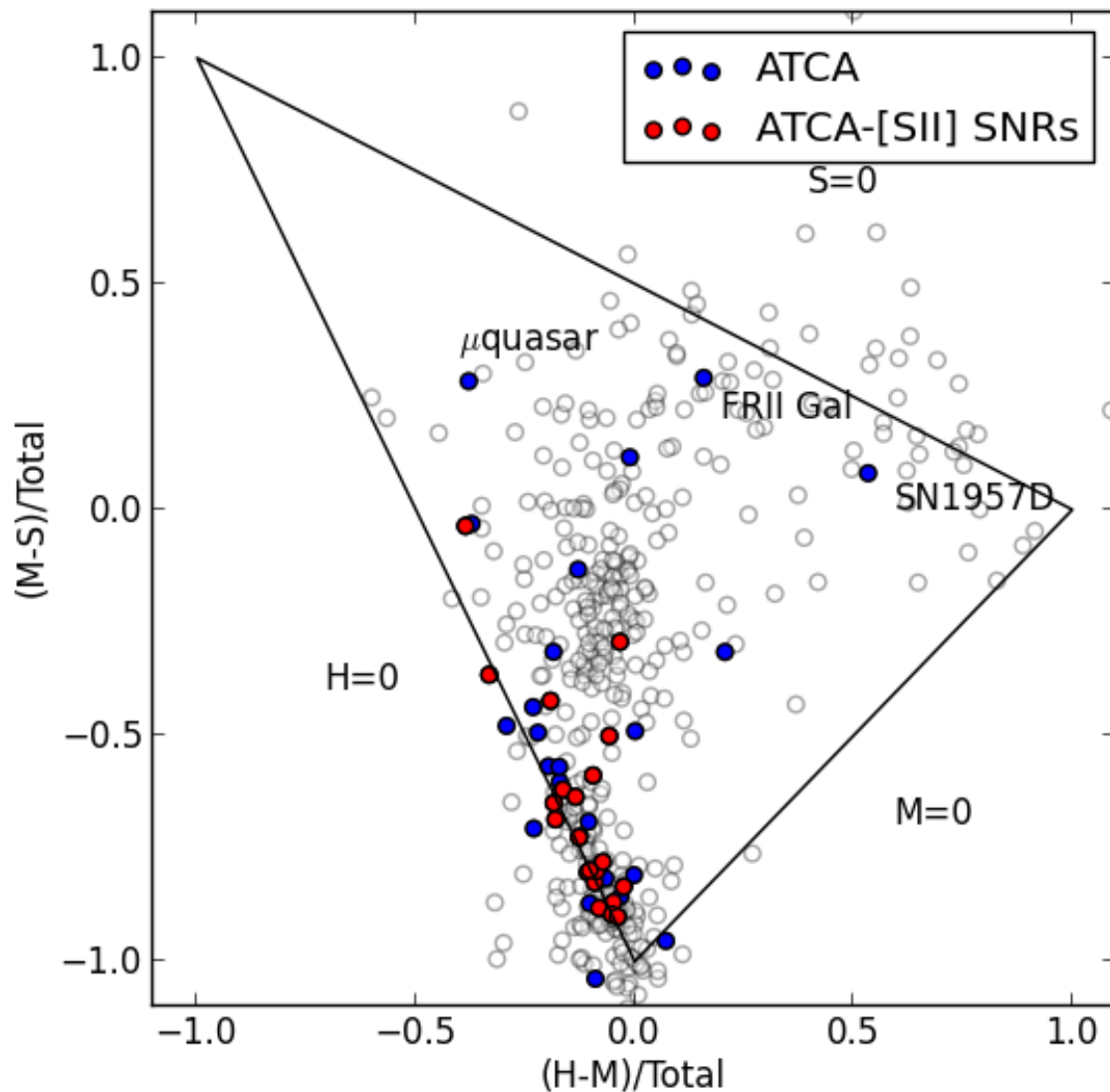
Fig. 6.— A hardness ratio plot of X-ray sources identified with ATCA sources. Sources which are identified with optically identified SNRs are shown in red, and the remainder of the sources are plotted in blue. The entire sample is also shown for context. The hardness ratios of several specific sources are labeled.
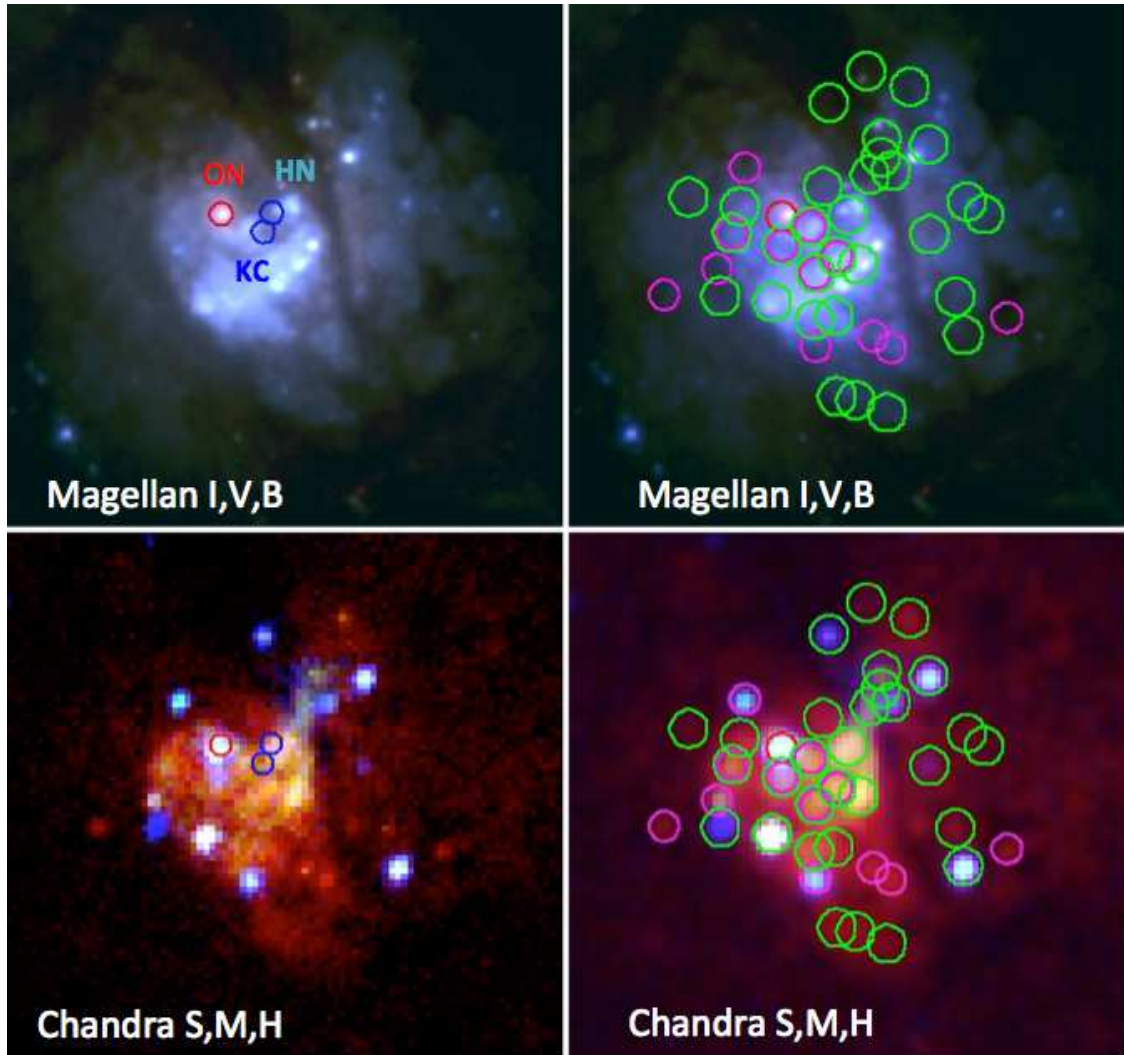
Fig. 7.— A 35″ region near the nucleus of M83 in optical and X-ray. Top two panels show the Magellan broadband data, where red = I band, green = V band, and blue = B band. The bottom two panels show the *Chandra* data in three-color format, with red = 0.35-1.2 keV (soft), green = 1.2-2.6 keV (medium), and blue = 2.6-8.0 keV (hard). The left panel is at the full *Chandra* resolution, while the right panel has had a small amount of smoothing applied. The three small regions shown in the left two panels represent the positions of the optical nucleus (red), the kinematic center determined by (Thatte et al. 2000, lower blue circle), and the so-called "hidden nucleus" inferred by Mast et al. (2006). The two right panels show source positions as found by *AE*. Green circles typically have no specific optical source but rather correspond to high star formation regions, or in a few cases actual young clusters. Magenta circles align closely with SNRs identified by Dopita et al. (2010) in *HST*/WFC3 data, although in some cases the alignment may be fortuitous. A red circle in the right two panels indicates source X233, which corresponds to the optical nucleus. Some of the harder (blue and white) sources in both green and magenta circles may actually be X-ray binaries, but no optical identifications with point sources have been made.
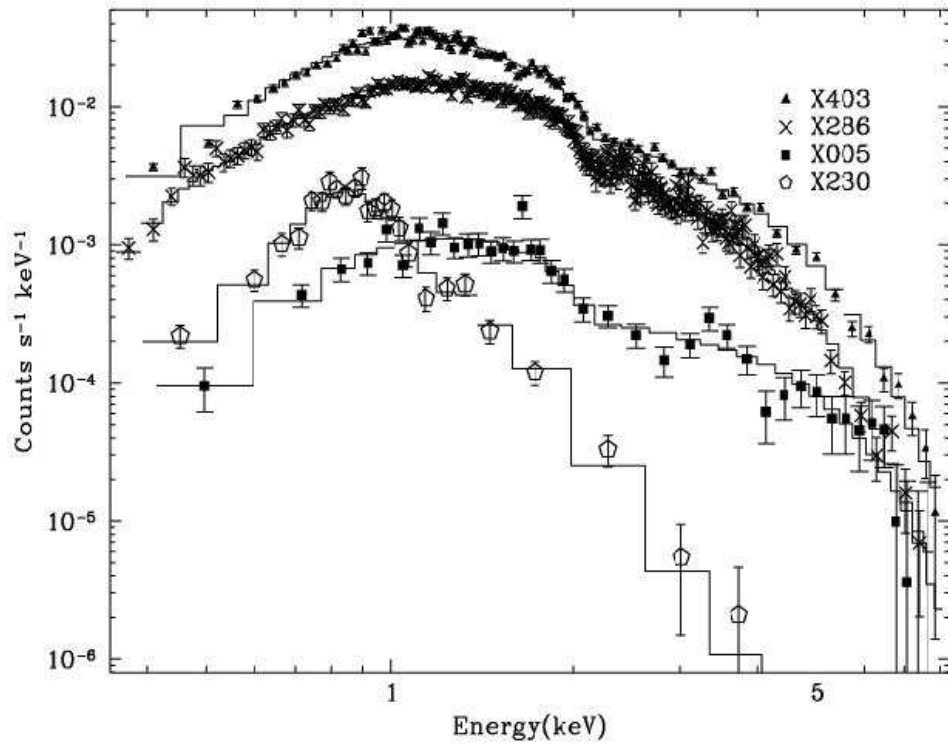
Fig. 8.— Examples of the different types of spectra observed in the bright and moderately bright sources. X403 and X286 are examples of bright sources. X403 had more than 12,000 counts and is modeled in terms of a disk-blackbody + power law spectrum, while X286 is just a disk-blackbody. X005 and X230 are examples of moderately bright sources, both having of order 1000 counts total. These two were selected to show the difference between a thermal and non-thermal spectrum with this number of source counts.
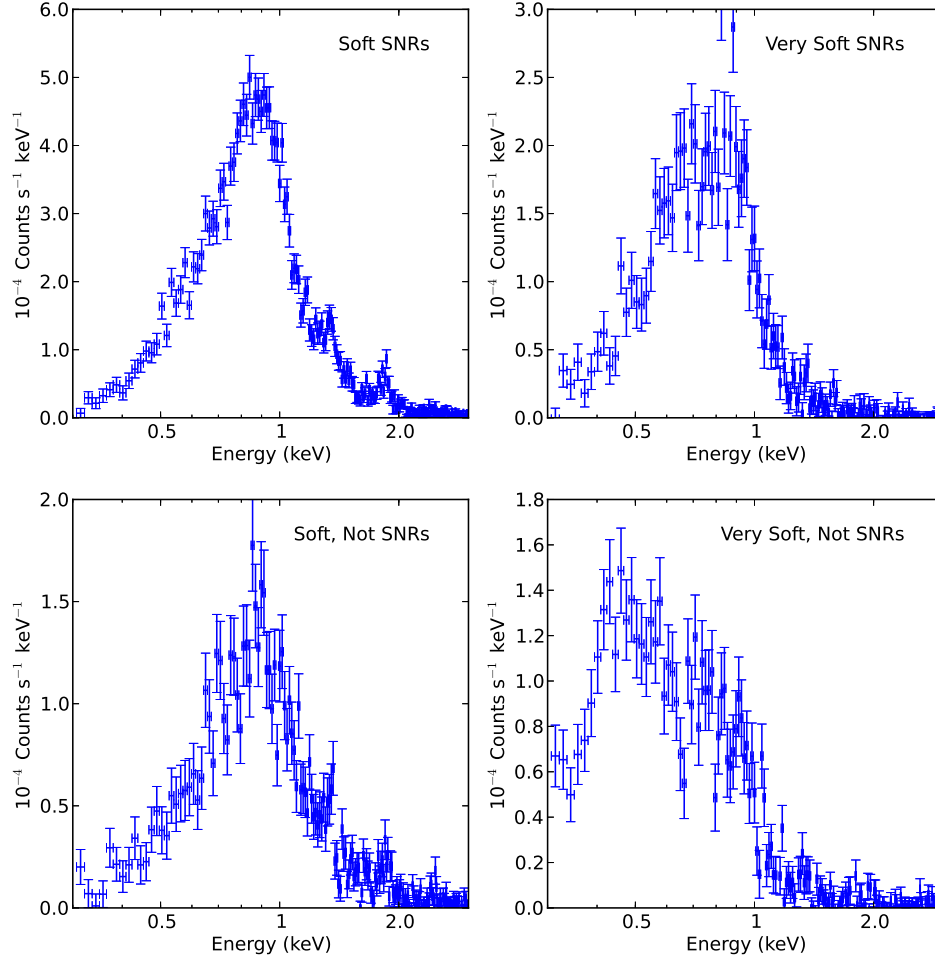
Fig. 9.— A comparison of the summed spectra of various groups of soft sources. The sources have been divided into four groups. The upper left panel shows the summed spectra for objects identified as SNRs which have hardness ratios (M–S/T) between -0.88 and -0.5. The lower left panels shows summed spectra for objects which are not identified as SNRs but have hardness ratios between -0.88 and -0.5. The upper right and lower right panels show objects which have hardness ratios less than -0.88, split into objects that are identified as SNRs and objects that are not identified as SNRs. The composite spectra of the "Soft, Not SNRs" objects and the "Soft SNRs" objects are very similar, showing the same spectral features, suggesting that some of the 'Soft, Not SNRs" objects are actually SNRs as well. The composite spectrum of "Very Soft, Not SNRs" objects shows and an excess at 0.5 keV, not seen in the "Very Soft SNRs" group, which may indicate the some of these objects are true supersoft sources.
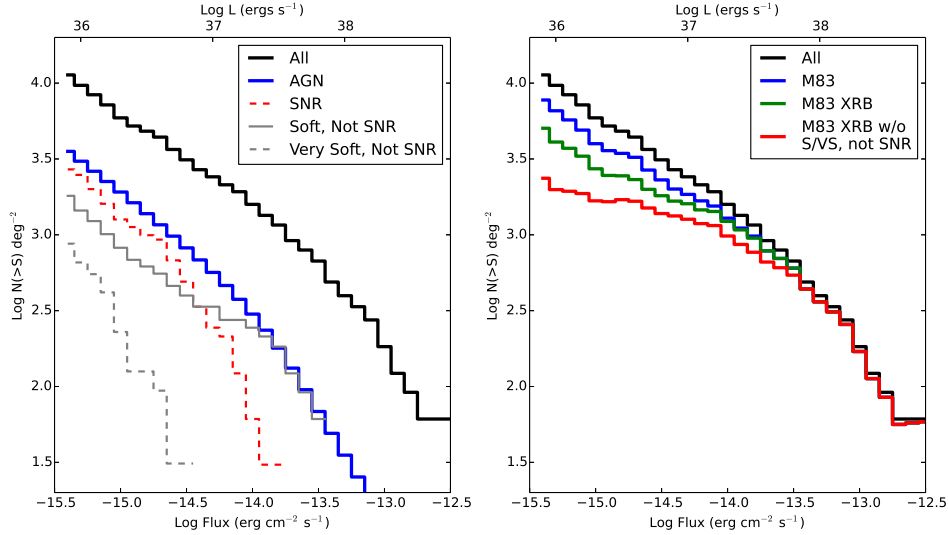
Fig. 10.— *Left:* The broad-band (0.35 - 8 keV) CLF of sources within the D_{25} region of M83 before subtraction of foreground and background sources, and various subpopulations of the CLF, namely AGN, X-ray sources identified as SNRs, other soft sources ("Soft, not SNRs"), and other very soft sources ("Very Soft, Not SNRs"). The contribution of AGN to the CLF was estimated statistically, as discussed in Section 9.1. Foreground stars are not an important contributor to the CLF. The nature of the "Soft, not SNRs" and "Very Soft, Not SNRs" sources is discussed in Section 8. *Right:* The broad-band CLF before subtraction, the M83 CLF obtained by removing AGN and foreground stars, and the XRB CLF obtained by also removing SNRs from the sample, and finally the CLF, with background and foreground sources, SNRs, and other soft and very soft sources subtracted. We suspect that some, perhaps the majority, of the "Soft, not SNRs" and "Very Soft, Not SNRs" sources are SNRs. If so, this has a significant affect on the CLF for XRBs in M83.
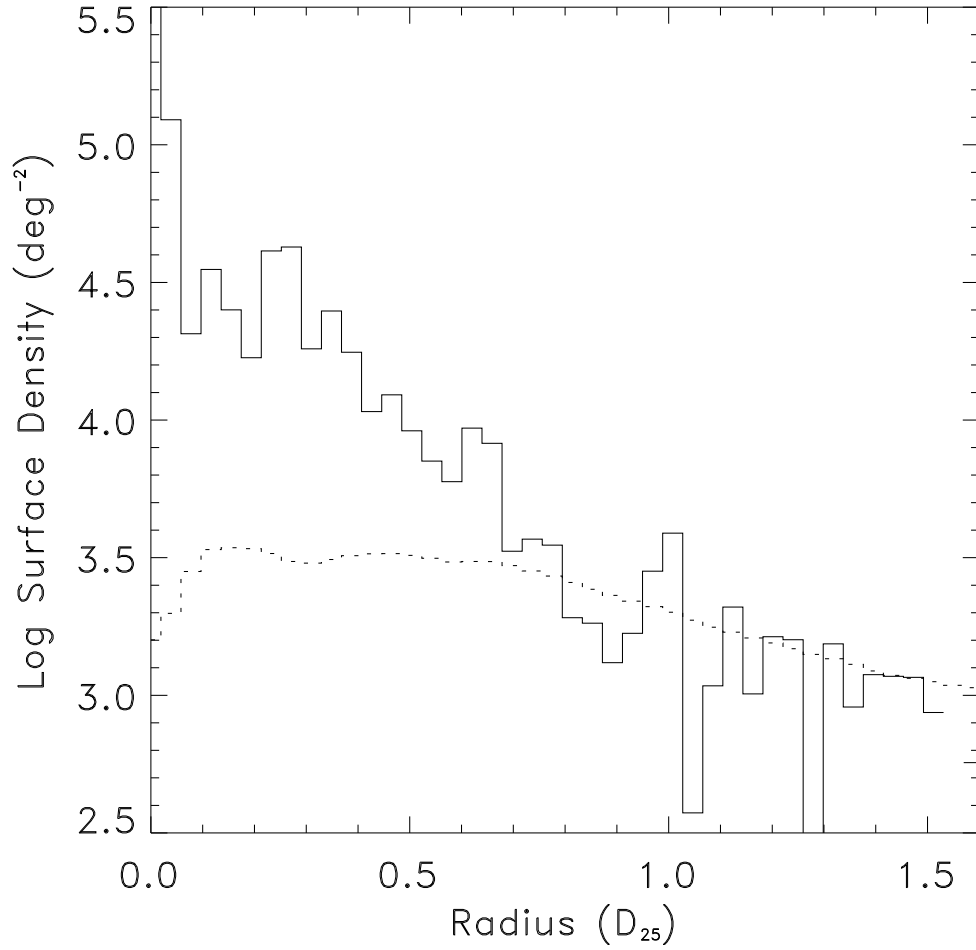
Fig. 11.— The surface density of all point sources with $\log F \geq -6.5$ phot cm^{-2} s^{-1} in the 0.35-8 keV band. The dotted line is the radial profile of the AGN calculated as described in the Section 9.1. The decline in the predicted density of AGN towards the center of the galaxy is due to the absorption by M83, while the decline towards the outer parts of the galaxy is due to the decrease in sensitivity of the observations.
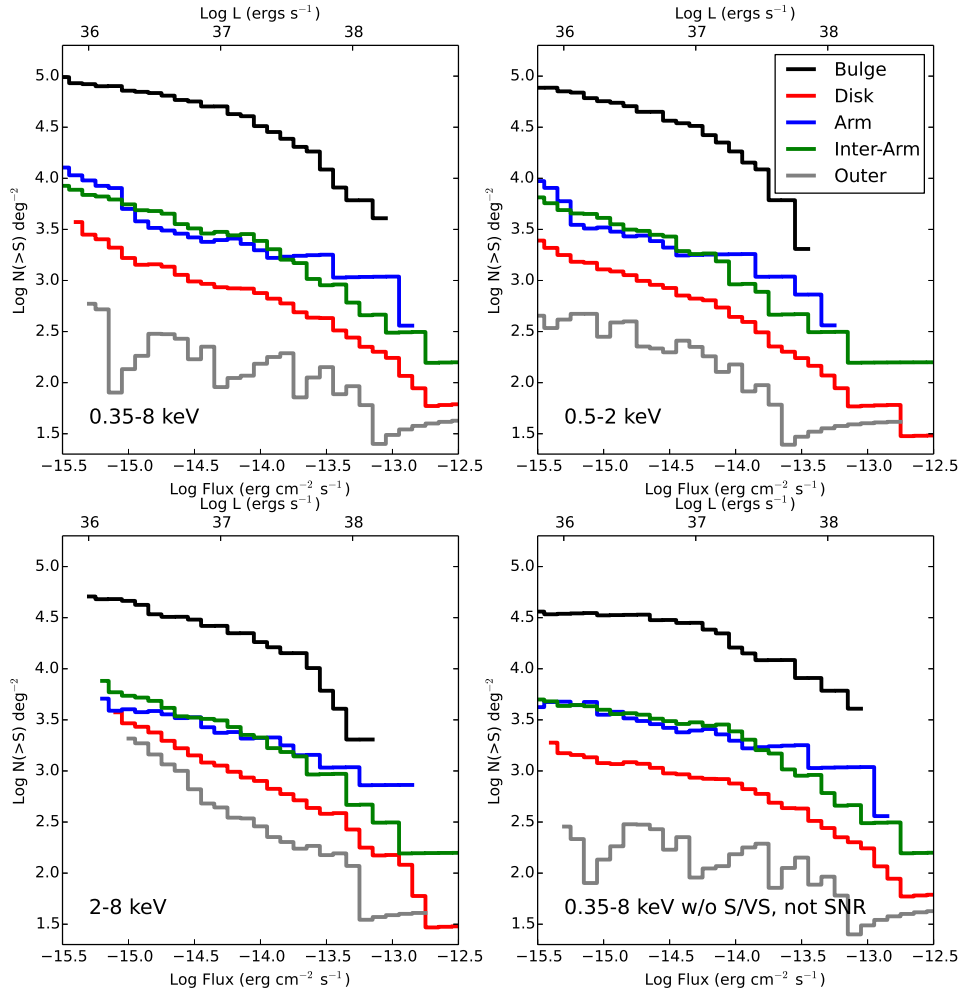
Fig. 12.— XRB CLFs in the 0.35-8 keV (upper left), 0.5-2.0 keV (upper right) and 2.0-8 keV (lower left) bands for a variety of different regions in M83. The number of sources differ in the various bands because only sources with probability-of-no-source $< 5 \times 10^{-6}$ in that band are included in the CLF for that band. In all panels, the black lines shows the CLF for the bulge/nuclear region of the galaxy, while the red line shows the CLF of the disk. The CLF for the arm and inter-arm regions and outer disk are shown separately. Source density decreases with radius, which explains why the CLF for arm and inter-arm regions inner disk disk are always greater than that for the outer disk. The various regions are shown graphically in Figure 13. The lower right hand panel shows the 0.35-8 keV CLF with all soft sources removed, not just SNRs. Removing the soft sources ("Soft, not SNRs" and "Very Soft, not SNRs") flattens the CLF at lower luminosities, and makes all of the CLFs look more similar aside from an overall normalization. The densities of sources in the arm and inter-arm regions are very similar, indicating that there is not a large concentration of XRBs in the spiral arms.
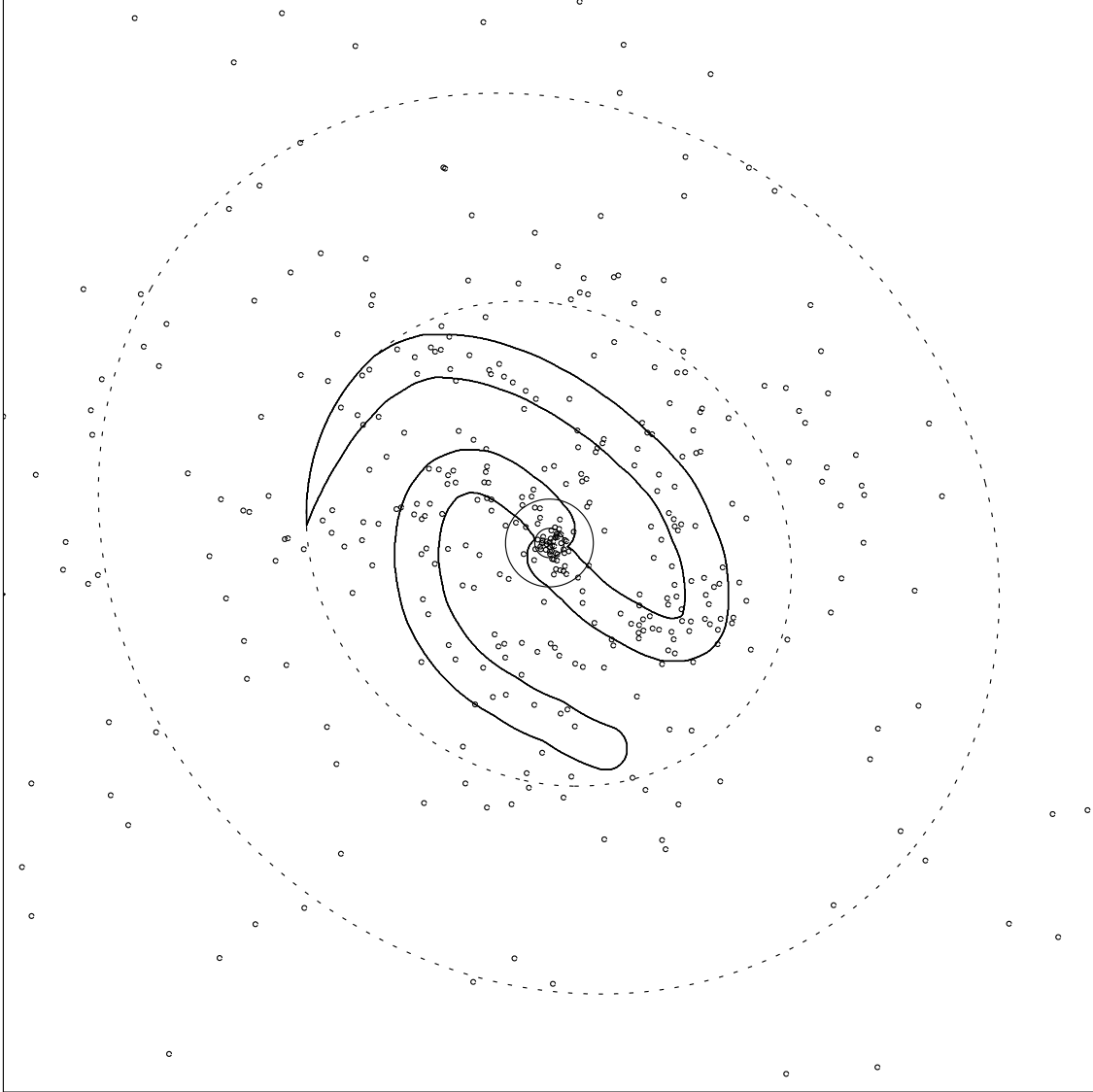
Fig. 13.— The regions over which CLFs were extracted. The positions of the sources detected in the 0.35-8 keV band are also shown. The inner ellipse at $R_{proj} = 3\rlap{.}'5$ is the boundary between the inner and outer disk; the outer ellipse at $R_{proj} = 6\rlap{.}'5$ corresponds to the D_{25} contour. The inner circles have radii of $0\rlap{.}'3$ and $0\rlap{.}'6$ and define the nucleus and outer bulge regions. Although the arms extend beyond $R_{proj} = 3\rlap{.}'5$, we have only used the region between $0\rlap{.}'6$ and $R_{proj} = 3\rlap{.}'5$ for the purpose of extracting the arm and inter-arm CLFs.
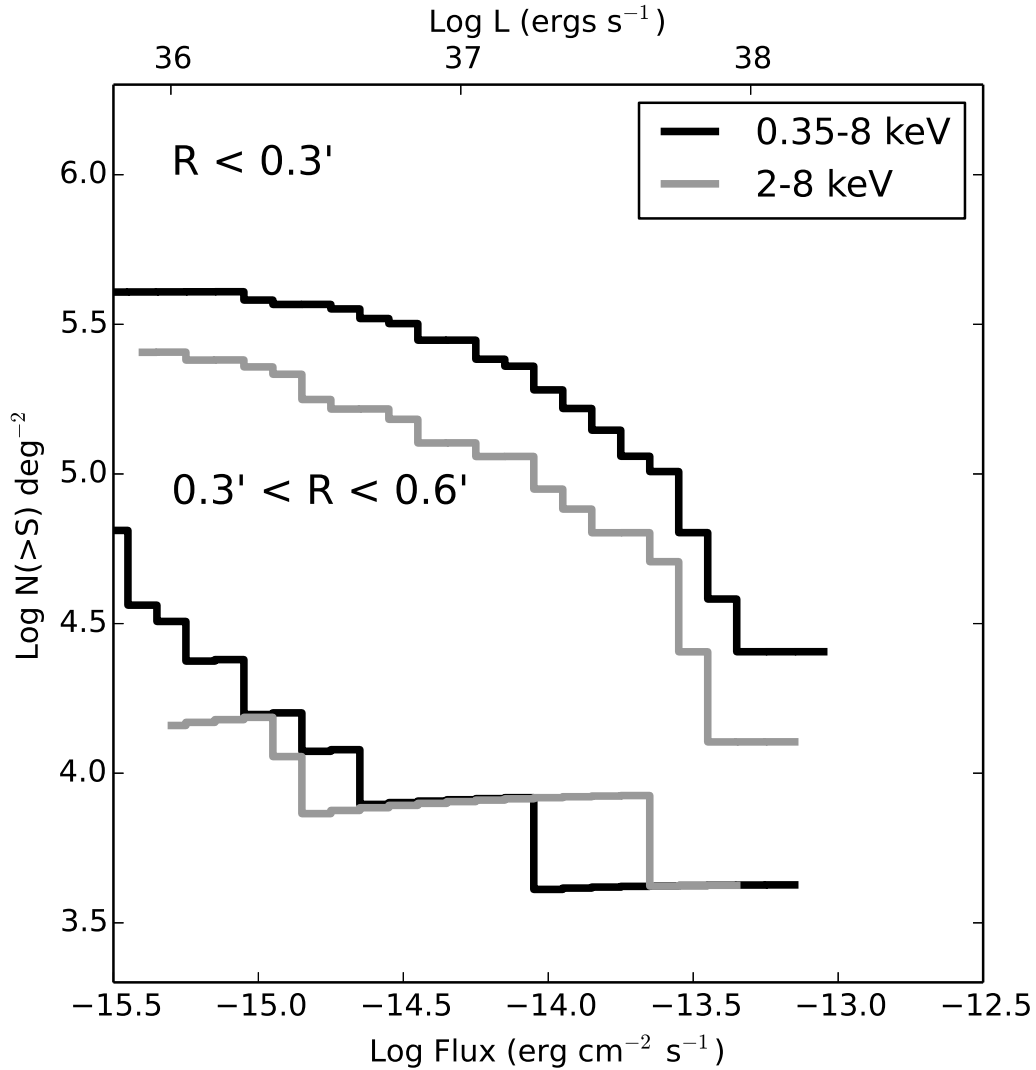
Fig. 14.— The CLFs for the inner bulge or nuclear region ($R < 0\rlap{.}'3$) and the outer bulge region ($0\rlap{.}'3 < R < 0\rlap{.}'6$). The heavier lines indicate the 0.35-8.0 keV band; lighter lines, the 2.0-8.0 keV band. The 2.0-8.0 keV band CLFs have been adjusted to the 0.35-8.0 keV band luminosities. At 0.35-8 keV, the CLF for the outer bulge extends to lower luminosities than that for the inner nucleus, due to the strong diffuse emission in the nucleus and to source crowding.
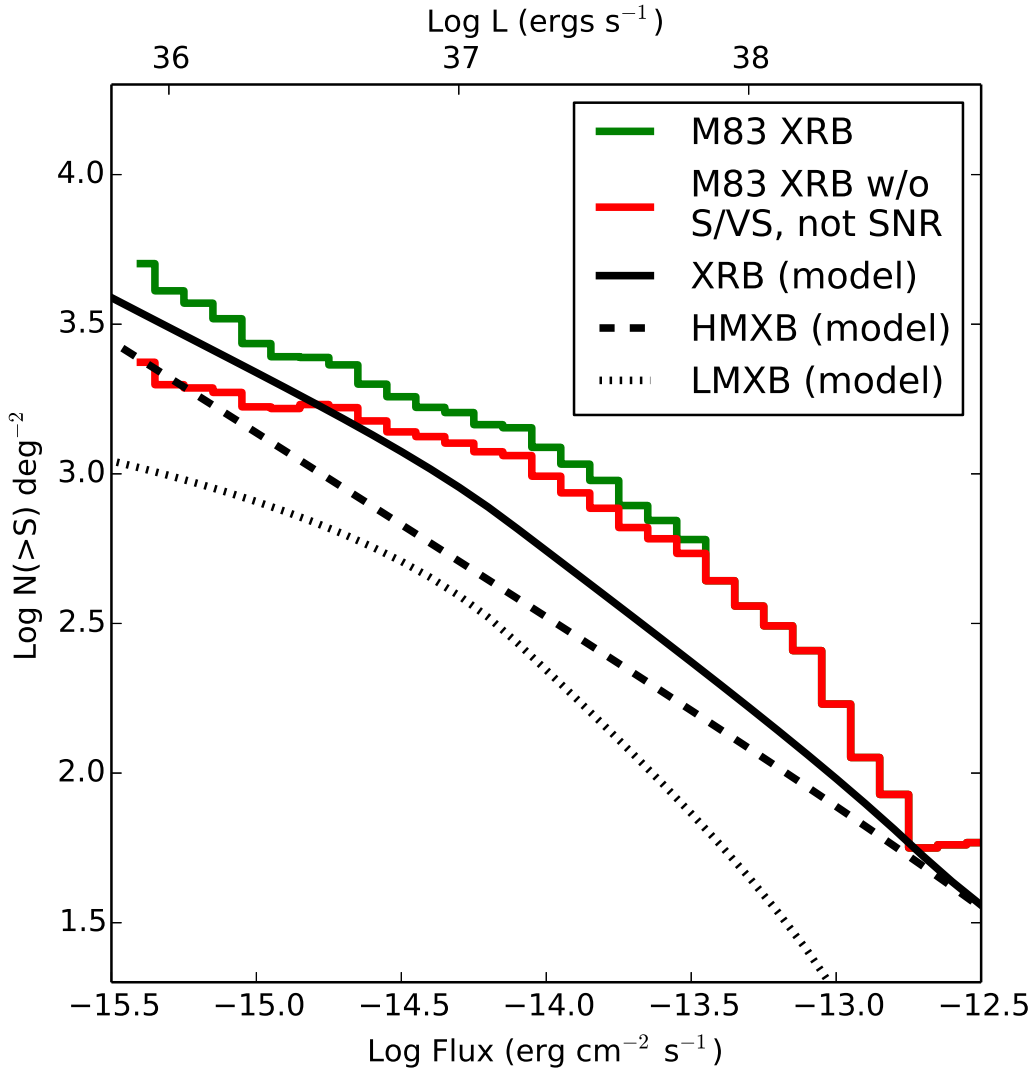
Fig. 15.— The 0.35-8.0 keV band CLF of the galaxy within the D_{25} contour after the removal of the AGN, foreground stars and SNRs (in green), and, in addition, the "Soft, Not SNR" and "Very Soft, Not SNR" sources (in red). The remaining lines are the predicted CLF based on the model of Gilfanov (2004) for XRBs (the solid black line) and the contributions from HMXBs (the dashed black line) and LMXBs (the dotted black line). The predicted CLF has been scaled from the star-formation rate and stellar mass of M83. The predictions are not a very good match to the CLF observed in M83.